

Copyright

by

Ryan Thomas Woodall

2020

The Dissertation Committee for Ryan Thomas Woodall Certifies that this is the approved version of the following Dissertation:

Models of Fluid Dynamics in Biological Tissues for Medical Imaging and Drug Delivery

Committee:

Thomas E. Yankeelov, Supervisor

Jeanne C. Stachowiak

Christopher G. Rylander

George Biros

Andrew J. Brenner

**Models of Fluid Dynamics in Biological Tissues for Medical Imaging
and Drug Delivery**

by

Ryan Thomas Woodall

Dissertation

Presented to the Faculty of the Graduate School of

The University of Texas at Austin

in Partial Fulfillment

of the Requirements

for the Degree of

Doctor of Philosophy

The University of Texas at Austin

August 2020

Dedication

To my brother, Tyler Woodall, my foundation and inspiration, who knows my flaws yet trusted me to overcome them.

To my mother, Michelle Bohannon, my refuge and comforter, who allowed me to doubt myself so that I could ultimately believe in myself.

Acknowledgements

I would like to acknowledge my advisor and mentor Dr. Thomas E. Yankeelov, without whom I could not have achieved this. I am indebted to him for the patient, sensitive, and optimistic mentorship he provided, despite my own doubts about myself. Thank you for trusting me and being patient, all with a smile and good sense of humor. In that vein, I would also like to acknowledge Dr. David A. Hormuth, II, for treating me like an equal, for providing an extra set of hands when I was down one, and for his unparalleled taste in podcasts and restaurants. I would like to acknowledge Dr. Michael Abdelmalik for his help in stabilized fluid dynamics, and his lively dinner and drink discussions. I could not have made it through this process without the entirety of the Oncology Modeling Group, especially my fellow graduate students. Thank you for being supportive teammates, great listeners, and exceptional friends.

I would like to acknowledge my mother, my brother, Max Flagge, and Nond Hasbamrer for their untiring support and availability for phone calls and last-minute escapes from town. I also acknowledge Kevin, Donna, & Morgan Arnett, and Doug, Lou Ann, & Abigail Woodall, for providing me shelter and a sense of familial closeness when I had no place of my own. I want to acknowledge the friends I've made in Austin, who have provided me with a sense of belonging, and the space to grow and change. You are as much my family as my blood relatives.

Finally, I want to acknowledge the University of Texas and the Department of Biomedical Engineering for providing me the opportunity to pursue this degree.

Abstract

Models of Fluid Dynamics in Biological Tissues for Medical Imaging and Drug Delivery

Ryan Thomas Woodall, Ph.D.

The University of Texas at Austin, 2020

Supervisor: Thomas E. Yankeelov

Fluid dynamics are essential to accurately describe the transport of any solute or particle delivered to a tumor, whether it is blood, nutrients, oxygen, systemic therapies, or a contrast agent. The purpose of this dissertation is to utilize quantitative medical imaging to inform computational fluid dynamics models of transport in biological tissues for applications in medical imaging and drug delivery, thereby improving our understanding of the imaging modalities, and providing accurate models of contrast agent and drug delivery for clinical use to maximize benefit to the individual patient. This objective is addressed in two distinct parts. First, we develop a high resolution, tissue-based model of contrast agent delivery in the mouse BT474 xenograft model of breast cancer, and simulate the acquisition of dynamic contrast enhanced magnetic resonance imaging data in this domain to test the accuracy of the standard methodology typically used to analyze such data. The results indicate that this widely used methodology for analyzing DCE-MRI data has inherent inaccuracies, as it does not account for passive delivery and distribution of the contrast agent due to diffusion within each voxel. Second, we develop, calibrate, and validate a mathematical model of convection-enhanced delivery of Rhenium-186

nanoliposomes to glioblastoma multiforme. The model is used to identify the optimal placement of the catheter within the tumor, so as to simultaneously minimize radiation exposure to healthy tissue and maximize tumor coverage. While models of convection enhanced delivery of molecular agents are currently on the market, no such models exist which are designed specifically for nanoparticle delivery, and which are calibrated and validated using clinical medical image data. Our results offer a useful model which accurately recapitulates the distribution of these liposomes, and is capable of identifying an optimal catheter placement for the delivery of these nanoparticles which avoids leakage into non-tumor regions.

Table of Contents

List of Tables	xii
List of Figures	xiii
Chapter 1: Introduction	1
1.1 Motivation.....	1
1.2 Clinical imaging for breast cancer	2
1.2.1 Dynamic contrast-enhanced MRI	2
1.2.2 DCE-MRI limitations	4
1.3 Glioblastoma Multiforme (GBM).....	5
1.3.1 Standard of care for GBM	6
1.3.2 Clinical imaging of GBM	6
1.3.3 Diffusion-weighted MRI.....	7
1.3.4 Single photon emission and X-ray computed tomography.....	9
1.5 Convection-enhanced Delivery.....	10
1.4.1 Rhenium-186 Nanoliposomes.....	11
1.5 Models of fluid transport in biological tissues.....	12
1.5.1 Darcy's Law	12
1.5.2 Starling's Law	13
1.5.3 Advection diffusion	13
1.6 Dissertation overview	14
1.6.1 Specific Aims.....	15
1.6.2 Significance	16
1.6.3 Innovation	17

1.7 Dissertation outline	18
Chapter 2: the effects of intra-voxel contrast agent diffusion on the analysis of DCE-MRI data in realistic tissue domains	22
2.1 Introduction.....	22
2.2 Methods	24
Sub-Sub-Heading (Heading 4).....	24
2.2.1 Histological analysis.....	24
2.2.2 Finite element methods: Forward Model.....	26
2.2.3 FEM Mesh	28
2.2.4 Simulations	29
2.2.5 Statistical analysis.....	31
2.2.6 Domain size analysis	32
2.3 Results.....	33
2.4 Discussion.....	35
2.5 Conclusion	38
2.6 Acknowledgements.....	39
Chapter 3: Patient specific, imaging-informed modeling of Rhenium-186 nanoliposome delivery via convection enhanced delivery in glioblastoma multiforme.....	47
3.1 Background and introduction.....	47
3.2 Methods	49
3.2.1 Clinical protocol	49
3.2.2 Imaging details.....	50
3.2.3 Image processing	51
3.2.4 Fluid dynamics model.....	52

3.2.5 Numerical implementation and analysis.....	54
3.2.6 In silico assessment of model fidelity.....	56
3.2.7 Model family.....	57
3.2.8 Statistical analysis and model selection.....	57
3.2.9 Validation.....	59
3.3 Results.....	60
3.3.1 Convergence analysis	60
3.3.2 Calibration and model selection	60
3.3.3 Model prediction.....	61
3.4 Discussion	61
3.5 Conclusion	63
3.6 Acknowledgements.....	64
3.7 Ethical Statement	64
Chapter 4: A framework for optimal catheter placement for RNL delivery.....	76
4.1 Introduction.....	76
4.2 Methods	77
4.2.1 Prediction of RNL distribution	77
4.2.2 Objective function and analysis.....	78
4.3 Results.....	79
4.3.1 Objective function maps	79
4.3.2 Optimization comparison.....	80
4.4 Discussion.....	80
4.5 Conclusion	82

4.6 Acknowledgements.....	83
4.7 Ethical Statement	83
Chapter 5: Conclusion.....	92
5.1 Summary	92
5.2 Future directions	92
5.2.1 Models of DCE-MRI data.....	92
5.2.2 Modeling RNL-186 for CED	93
5.2.3 Optimizing catheter placement	94
References.....	95
Vita.....	110

List of Tables

Table 2.1:	Summary of parameterization errors over all four tumors.....	46
Table 3.1:	Clinical patient details.....	65
Table 3.2:	Clinical imaging details	66
Table 3.3:	Clinical MR image acquisition parameters.....	67
Table 3.4:	List of each member of the model family and their associated and unknown parameters θ_n	68
Table 3.5:	AIC, CCC, and Dice for model calibrations for each patient and model combination.....	69
Table 3.6:	Prediction results.....	70
Table 4.1:	Comparison of the objective function components and objective function.	91

List of Figures

Figure 1.1:	Compartment diagram of the extended Kety-Tofts model. Contrast agent may transfer between the plasma compartment to the extra-vascular extra-cellular compartment with a volumetric rate of K^{trans} . Contrast agent.....	19
Figure 1.2:	Depictions of DCE data. Figure 1.2a depicts a population AIF, which acts as known source term for the Kety-Tofts model.	20
Figure 1.3:	Depiction of apparent diffusion coefficient of water with decreasing freedom of diffusive mobility.	21
Figure 2.1:	Depiction of workflow for developing the simulation domain.....	40
Figure 2.2:	Model results from simulations performed on a representative necrotic tissue domain.	41
Figure 2.3:	Model results from simulation performed on a representative well-perfused tissue domain.....	42
Figure 2.4:	Mean and 95% confidence intervals of the parameterization error in a single mouse specimen (see Figure 2.5) for a range of diffusivities.	43
Figure 2.5:	Depiction of parameterization error for a single tumor specimen	44
Figure 2.6:	Comparison of model accuracy as a function of distance from blood vessel.....	45
Figure 3.1:	Schematic for modeling process. The SPECT/CT and MRI data are first co-registered and used to create the FEM mesh.	71
Figure 3.2:	Demonstrative T1+contrast image, and its corresponding FEM mesh.....	72
Figure 3.3:	Model Convergence with mesh refinement. Depicted are the total residuals (defined as the L-2 norm) of the steady-state pressure field.	73
Figure 3.4:	Visualization of the Model 1 prediction for (representative) Patient 5.	74

Figure 3.5: Visualization of the Model 12 prediction for representative Patient 5.	75
Figure 4.1: Objective function overlain on T_1 + contrast image for Patient 1 on central tumor slice.....	84
Figure 4.2: Objective function overlain on T_1 + contrast image for Patient 2 on central tumor slice.....	85
Figure 4.3: Objective function overlain on T_1 + contrast image for Patient 3 on the central tumor slice.....	86
Figure 4.4: Objective function overlain on T_1 + contrast image for Patient 4 on the central tumor slice.....	87
Figure 4.5: Objective function overlain on T_1 + contrast image for Patient 5 on the central tumor slice.....	88
Figure 4.6: Maps of individual components of objective function J	89
Figure 4.7: Distributions of RNL in Patient 3, resulting from the mean distribution of 100 Monte Carlo predictions	90

Chapter 1: Introduction

1.1 Motivation

The overarching goal of this dissertation is to develop fluid dynamical models for the delivery of metabolites to cancer, informed by medical imaging. In the case of breast cancer, dynamic contrast enhanced MRI is a tool utilized to parameterize and classify tumors. The most widely used models of contrast agent delivery to tumors assume that the spatial dependence of contrast agent is negligible, but as our understanding of cancer biology grows, we are beginning to understand that cancer is highly dependent upon shape and geometry, as well as the spatial heterogeneity of cancer cells within a tumor. As such, this dissertation challenges the assumption that spatial contributions to contrast agent arrival within a tumor, for dynamic contrast enhanced imaging, is unimportant, as is a source of significant error in the standard method of dynamic contrast enhanced MRI quantification and data processing. In the case of glioblastoma multiforme, a highly aggressive and lethal form of primary brain cancer, aggressive and risky treatments must be used to extend the patient's life. Convection enhanced delivery of radioactive liposomes *via* catheter directly to the tumor location is one such treatment for this type of cancer. Due to the extreme risks involved in perfusing brain tissue with a highly radioactive therapeutic, it is imperative to use all the information available to be able to accurately predict and optimize the treatment for individual patients receiving this radical life-extending treatment.

The following introduction serves to introduce and motivate the studies performed in this dissertation. First, we introduce breast cancer imaging modalities, their uses and limitations, in order to motivate the research implemented in Chapter 2. Second, we introduce glioblastoma, its relevant imaging modalities, and discuss radio liposome treatment to motivate a model of convection enhanced delivery of said liposomes, discussed in Chapters 3 and 4. Each of these projects utilize models of fluid dynamics, informed by medical imaging, to further inform the field of biomedical engineering using the plethora of medical imaging information available to us in our modern age.

1.2 Clinical imaging for breast cancer

Breast cancer is most common type of cancer in women, accounting for over a quarter of all cancer diagnoses in woman across the world. Woman have a 13% lifetime risk factor of developing breast cancer [1]. Because breast cancer is so common, woman are advised to undergo breast cancer screenings to detect abnormalities beginning at age 40 [2]. Early detection of breast tumors is associated with higher treatment efficacy and survival [3]. Screening for breast cancer is typically done with X-ray mammography, where breast tissue is flattened between two plates (to increase image contrast), and an image of tissue density is acquired. If an abnormality is identified by a radiologist, further imaging and biopsies are performed to establish a definitive diagnosis.

Upon detection of a suspicious lesion, the focus of imaging shifts to diagnosis. Multi-parametric magnetic resonance imaging (MRI) is often performed at this stage to identify various properties of the tumor, including its shape, density, and perfusion characteristics. In particular, diffusion-weighted (DW) MRI is performed to assess tumor cell density, as breast tumors frequently present with increased cellularity compared to the surrounding tissue. Contrast-enhanced (CE) and dynamic contrast-enhanced (DCE) MRI are often performed to visualize characteristics related to blood flow and the highly permeable vasculature commonly associated with many types of cancer. These MRI modalities assist physicians in making the decision to proceed to obtaining a biopsy or active surveillance. As contrast enhanced MRI is central to all three aims of this Dissertation, we detail the technique in the next section.

1.2.1 Dynamic contrast-enhanced MRI

Dynamic contrast-enhanced MRI (DCE-MRI) is a noninvasive method to estimate pharmacokinetic properties of a tumor [4], [5]. Quantitative DCE-MRI requires the following measurements: a pre-contrast T_1 map, dynamic T_1 -weighted data acquired before/after the administration of a contrast agent (described in the previous section), the concentration of the contrast agent in the blood plasma over time, and a pharmacokinetic model to analyze the resulting data. By fitting the signal intensity time courses to a

compartment model, estimates of quantities related to vascular, cellular, and extravascular extracellular volume fractions can be quantified. Additionally, the volumetric fluid flux between vascular and extravascular extracellular compartments can be quantified. The transfer of contrast agent between tissue compartments is modeled using a two-compartment model, similar to first-order models of chemical reactions. A visualization of this two-compartment model is shown in **Figure 1.1**, and the corresponding ordinary differential equation (ODE) is given by:

$$\frac{\partial C_t(t)}{\partial t} = C_p(t)K^{trans} - C_t(t)K^{ep}, \quad 1.1$$

$$K^{ep} = K^{trans} / v_e, \quad 1.2$$

where C_t is the concentration of contrast agent within the tissue interstitium, C_p is the concentration of contrast agent within the vasculature (i.e., the arterial input function), K^{trans} is the volumetric transfer coefficient from the vascular compartment to the tissue compartment (in units of inverse time), K^{ep} is the volumetric transfer coefficient from the tissue compartment to the vascular compartment (in units of inverse time), and v_e is the extravascular extracellular volume fraction. In addition to the measured signal intensity time course of the tissue of interest, the time course of concentration of contrast agent in the blood is also needed (i.e., C_p). This measurement is particularly difficult and many methods for obtaining it from individuals [4] or populations [6] have been established for both pre-clinical and clinical studies. The solution to Eq. [1.1] is given by:

$$C_t(t) = K^{trans} \int_0^t C_p(u) \cdot \exp(-K^{trans} / v_e (t-u)) du \quad 1.3$$

where u is a dummy variable of integration. This formulation is known as the standard Kety-Tofts model [7]. In cases of tumors with significant blood plasma contributions to signal intensity (i.e., plasma volume fraction > 0.05 [8]), an extended Kety-Tofts model is used to incorporate the addition of the plasma compartment:

$$C_t(t) = K^{trans} \int_0^t C_p(u) \exp(-K^{trans} / v_e (t-u)) du + v_p C_p(t), \quad 1.4$$

where v_p is the vascular volume fraction.

Importantly, the concentration of contrast agent in the various tissue spaces is not measured directly in an MRI experiment. Thus, the measured signal intensity has to be converted to an estimate of the concentration of contrast agent so that Eq. 1.4 can be applied to estimate pharmacokinetic parameters. For the particular type of image acquisition employed in our studies (i.e., the spoiled gradient recalled echo), the MR signal intensity is given by:

$$SI = S_0 \frac{\sin \alpha \cdot (1 - \exp(-TR \cdot R_1))}{1 - \cos \alpha \cdot \exp(-TR \cdot R_1)}, \quad 1.5$$

where S_0 is the baseline signal intensity, α is the flip angle, TR is the repetition time for the scan, $R_1(t)$ is the longitudinal relaxation rate constant, and we have assumed that the echo time is much less than the tissues T_2^* . R_1 is converted to the concentration of contrast agent *via*:

$$R_1 = r_1 C_t(t) + R_{1,0}, \quad 1.6$$

where r_1 is the relaxivity of the contrast agent (in units of $\text{mM}^{-1}\text{s}^{-1}$), C_t is the concentration of the contrast agent, and $R_{1,0}$ is the pre-contrast R_1 value of the voxel which is obtained from a T_1 -mapping acquisition [4]. Eq. [1.5] coupled to Eq. [1.6] is then fit either on a voxel-by-voxel basis or for an entire region of interest (ROI). If fit for individual voxels, each voxel will yield its own pharmacokinetic parameters (e.g., K^{trans} or K_{ep}) which can then yield maps that can be overlain on anatomical images to visualize the spatial distribution of each parameter. A sample DCE-MRI enhancement curve, model fit, and AIF are demonstrated in **Figure 1.2**.

1.2.2 DCE-MRI limitations

DCE-MRI is widely considered to be an effective method of measuring the transport dynamics of contrast agent within tumor tissue [4], [9]. While the information it provides is relevant to transport and has shown to be useful in the diagnostic and prognostic settings, the pharmacokinetic models used to analyze the DCE-MRI data do not necessarily properly characterize the relevant physiology, and as such its usage has numerous limitations [8], [10].

A primary limitation of the Kety-Tofts model is that it does not consider fluid transport between voxels [10]. All contrast agent which enters a voxel is assumed to both arrive and leave from vasculature within the voxel. This requires the assumption that interstitial fluid flow between voxels is negligible [10]. Another fundamental assumption of DCE-MRI is that the contrast agent within the extravascular extracellular space in each voxel instantaneously equilibrates. However, the known diffusion coefficient of the common FDA-approved contrast agents (2.6 mm²/s, Gadovist, Bayer, Whippany, NJ) (mm²/s), is significantly smaller than what would enable instantaneous filling of the interstitial space on the time scale of typical DCE-MRI image acquisitions (1.6 seconds) [8].

As the Kety-Tofts model is widely used, yet has potentially conflicting assumptions built into its methodology, it is important to understand the validity of this model. To estimate the validity of this model in a pre-clinical mouse xenograft model of breast cancer, in Chapter 2, we simulate contrast agent delivery to a histologically-derived tumor domain with known perfusion parameters and volume fractions, and compare those known quantities to those obtained from a simulated DCE-MRI acquisition and the standard extended Kety-Tofts model.

1.3 Glioblastoma Multiforme (GBM)

The following sections are intended to introduce the necessary information to motivate an imaging informed model of convection enhanced delivery for the treatment of recurrent GBM. GBM is the most common of the primary brain cancers, and is the most deadly. GBM has an incidence of 3.2 in 100,000 person-years, and accounts for the majority of all primary central nervous system tumors [11]. The disease grows rapidly, and is often undetected until acute neurological symptoms necessitate hospitalization [12]. Once diagnosed with GBM, median survival time is only 14 months, and the disease is almost guaranteed to recur, with a five year survival under 5% [13]. As GBM is so deadly, there are a number of trials ongoing, attempting to increase both median and five-year survival.

1.3.1 Standard of care for GBM

Typical treatment for GBM consists of an initial tumor resection (to relieve interstitial pressure and mass effect), external beam radiation therapy, and concurrent chemotherapy [14]. In most clinical presentations of GBM, primary tumor resection is necessary for the immediate survival of the patient and reduction of the rapid onset of acute symptoms including nausea, headache, lack of motor control, and seizure, stemming from the increased cranial pressure introduced by the tumor [12]. External beam radiation serves to provide a locally elevated dose of ionizing radiation to kill tumor cells within the region of exposure. Concurrent chemotherapy is typically delivered as temozolomide, a DNA alkylating agent. While effective when in combination with external beam radiation [14], temozolomide is a nonspecific cancer treatment, and causes off-target effects including nausea, fatigue, alopecia, and severe myelosuppression [15]. Temozolomide relies on the disruption of the BBB to successfully enter the tumor region, and as such requires a high dose to provide a therapeutic effect, resulting in increased morbidity from off-target effects [14]. Temozolomide is not known to be effective at extending post-resection survival alone, but has been shown to extend survival from 12.1 to 14.6 months when given concurrently with radiation therapy [14]. More generally, systemically delivered chemotherapies have difficulty reaching regions of brain tumors that possess an intact blood-brain barrier, meaning, thereby reducing the effectiveness of the intervention [16]. Despite this aggressive post-surgical treatment, GBM is all but guaranteed to recur, with a 5 year survival of less than 5% [12].

1.3.2 Clinical imaging of GBM

As the incidence of GBM is quite low (a total lifetime risk of between 4 and 5/1000), regular surveillance screening for this disease is not performed. Instead, screening for GBM typically occurs after a patient complains of symptoms associated with GBM, such as headache, changes in personality, vomiting, or difficulty speaking [12]. Initial screening is performed *via* magnetic resonance imaging.

At initial presentation, a multimodal suite of MRI scans is performed to locate the tumor and identify the extent of disease. CE-MRI and DCE-MRI are utilized to visualize the tumor blood supply, as GBM is known to degrade the BBB and allow blood flow (and therefore contrast agent) into the tumor region. CE-MRI is the gold-standard for non-invasively identifying GBM, as the disease typically presents with a ring of contrast agent enhancement around a dark necrotic tumor core. T_2 -weighted and fluid attenuation inverse recovery (FLAIR) MRI are acquired to differentiate between tumor, edema, healthy tissue, and cerebro-spinal fluid (CSF). Diffusion MRI is also performed in GBM patients as the tumor burden changes the tissue density within and around the tumor, altering the apparent diffusion coefficient (ADC) of water in the brain at the tumor location. Additionally, diffusion tensor imaging (DTI) is a central tool for planning a surgical intervention. Water preferentially diffuses along white matter tracts in the brain which connect different functional regions of the brain. DTI allows for the measurement of the preferred diffusion direction and fractional anisotropy of the diffusion tensor, providing clear maps of white matter tracts, helping to plan for a tumor resection. As with DCE-MRI, diffusion MRI provides data that is central to each Aim of this Dissertation; thus, we detail the technique in the next section.

1.3.3 Diffusion-weighted MRI

Diffusion-weighted MRI is capable of measuring the diffusion of water molecules within biological tissue [17]. Diffusion of water occurs is described by Brownian motion and, as such, the standard diffusion coefficient of water is temperature dependent, higher with increasing temperature (or thermal energy). The diffusion of a molecule is also affected by its surroundings; water molecules in free solution diffuse without restriction, while molecules within more complicated geometries can have more collisions with boundaries, effectively decreasing the apparent diffusion coefficient (ADC) of water. Further details are shown in **Figure 1.3**. To measure diffusion within biological tissue, a strong magnetic gradient is applied in a single direction, spatially encoding a phase difference in the direction of the gradient. Diffusion along the gradient direction will cause

a decoherence in bulk Larmor frequency, and a subsequent loss in signal intensity. The signal intensity for a diffusion-weighted image at a given position, may be determined by the following equation:

$$S = S_0 \exp(-\gamma^2 G_x^2 \delta^2 \Delta ADC_x), \quad 1.7$$

where S_0 is the baseline signal intensity, γ is the gyromagnetic ratio of water, G_x is the magnetic field gradient strength applied in direction x , δ is time the diffusion gradient field is on, Δ is the time between the gradient radio-frequency pulses, and ADC_x is the apparent diffusion coefficient of water in the x direction. This equation is often simplified by collecting all of the acquisition parameters into a single value, b :

$$S = S_0 \exp(-bADC_x), \quad 1.8$$

where

$$b = \gamma^2 G_x^2 \delta^2 \Delta. \quad 1.9$$

To determine the ADC in a single direction, the signal intensity is recorded at multiple b -values, and linear regression is performed on the natural log of the measured signal intensities. To obtain the average ADC irrespective of direction, the diffusion-weighted scan is repeated in all three orthogonal spatial directions x , y , and z , and its mean is taken:

$$ADC = (ADC_x + ADC_y + ADC_z) / 3 \quad 1.10$$

As the ADC of water is high (approximately 2.7×10^{-3} mm²/s at 37°C [17]) in unrestricted regions, and decreases in the presence of many physical barriers, the ADC is often used as a proxy measurement for cellularity or cell density. In cancer, the ADC is useful in identifying regions of abnormally high cellular density (often a sign of rapidly proliferating tumor cells), as well as regions of abnormally low cellular density (often a sign of necrosis) [18], [19]. The ADC is also useful in predicting resistance to flow, as fluid under a pressure gradient will preferentially flow along the direction of least resistance, and is used as a proxy for hydraulic conductivity in modeling interstitial fluid flow [20].

If the ADC is measured in six or more directions, a complete diffusion tensor image (DTI) may be constructed [17]. In tissues where neighboring cells are highly organized and structured, the DTI data can provide information on the orientation and arrangement of

cells. For example, DTI is widely used to identify the directions of white matter tracts within the brain, as water preferentially diffuses along the direction of the tract due to the increased presence of diffusion barriers in all perpendicular directions [17]. As such, DTI is an important tool for neurosurgical planning, by allowing physicians to visualize the physical connections between differing function regions in the brain. As advection is a directional process, hydraulic conductivity may also be considered as a tensor, with decreased resistance in directions of the least resistance [21].

1.3.4 Single photon emission and X-ray computed tomography

Many therapeutic agents are designed to preferentially deliver a payload containing a radioactive element to a particular area of interest—usually a diseased tissue. Once arriving at its destination, the agent can irradiate into the targeted tissue [22]. There are some agents which are designed to emit to forms of radiation—one to deliver a therapeutic effect, and another designed to be captured outside the body to form an image and determine the internal distribution of the drug. The radiation which escapes the body may be observed (depending on the tracer) by the common nuclear imaging techniques of positron emission tomography (PET) and or single photon emission computed tomography (SPECT). In this dissertation, Aim 3 makes extensive use of SPECT data and we now focus on this technique.

SPECT imaging is utilized to visualize a spatial map of the location of where radioactive decay events are occurring within the body. To acquire a SPECT image, a patient is first placed into a SPECT scanner, consisting of a rotating 2D camera array. Individual gamma particles escape the body and are detected on a 2D camera array. This camera array rotates around the body part to be imaged, collecting a 2D image from many angles around the body. Each 2D image at each rotational position around the body is reconstructed into a 3D volumetric image using one of two methods. The simplest method of 3D reconstruction is filtered back-projection, where each 2D image is first projected in 3D along the direction it was acquired along, and each resulting projection is summed together and filtered to increase resolution. More advanced iterative reconstruction

algorithms now exist, which minimize imaging artifacts and take into account the attenuation of gamma particles by tissue [23], [24].

While SPECT images provide useful spatially resolved functional information, such as the location of radioactive decay events or high metabolic activity, images from the modality do not offer any anatomical context by themselves. As such, SPECT is often co-acquired with X-ray computed tomography. In X-ray CT, external gamma particles are emitted from a source outside the body and emitted through the body onto a detector on the opposite side. This source/detector pair also rotates around the body, and the resulting data is acquired and reconstructed in a similar fashion as the SPECT data. By co-acquiring SPECT with X-ray CT, the functional SPECT data may be registered and overlain on an anatomical map from co-acquired X-ray CT data [25].

1.5 Convection-Enhanced Delivery

Convection enhanced delivery (CED) is an experimental method for the delivery of therapeutic agents directly to cancers within the brain *via* a surgically inserted catheter. Agents delivered to the brain can either be chemotherapies or radiotherapies. After initial imaging and approval for entry into the study, a catheter is surgically inserted into the brain, directly into the tumor. The therapeutic agent is then delivered through the catheter, into the brain interstitium, using a syringe pump to supply pressure. The obvious advantage of this method is the direct delivery of therapeutic agents to the tumor without reliance on the breakdown of the BBB. This benefit is twofold: first, more active agent is delivered to the region of interest, increasing the dose delivered to the tumor. Second, the total amount of therapeutic delivered is substantially less than that which is systemically delivered, reducing overall systemic toxicity and off-target effects. In spite of these potential advantages, there is currently no CED protocol FDA-approved for clinical use. This is because CED carries with it numerous risks and tradeoffs. The first of which is the infusion rate. Higher infusion rates are known to correspond to larger coverage volumes, but also carry with them risks of backflow along the catheter [26], cavitation at the site of the tumor [27], and leakage into the CSF [28] and along white-matter tracts [29]. It is also theorized

that GBM grows in the direction of interstitial fluid velocity streamlines, meaning that there is therefore an increased risk of tumor invasion, especially in the case of prolonged CED at low flow rates, over the course of multiple days [30].

1.4.1 Rhenium-186 Nanoliposomes

Rhenium-186 nanoliposomes (RNL) are a radiotherapeutic agent, delivered *via* CED, under clinical investigation at The University of Texas at Health Science Center San Antonio. Rhenium-186, a beta- and gamma-emitting radioactive element, is encapsulated within liposomes composed of distearoylphosphatidylcholine (DSPC) and cholesterol in a molecular ratio of 55:45 [22]. Encapsulation into liposomes prevents leakage of the radiotherapeutic agent into the CSF, and increases the duration of tumor retention [31], [32]. This ensures that the radiation is primarily delivered to the tumor before it is cleared (by relying on the enhanced permeability and retention effect [33]), thereby limiting the exposure of healthy tissue (e.g. liver, kidney, healthy brain) to high doses of beta-radiation.

Rhenium-186 has two primary decay mechanisms: the first of which, accounting for approximately 93% of the energy emitted during decay, is decay to Osmium-186, with a neutron decaying into proton, emitting an electron and an electron antineutrino (1.07 MeV) [34]. The pathlength of this beta particle is approximately 2 mm before absorption into tissue. Beta decay accounts for the majority of energy deposition for this therapeutic method, and is the primary therapeutic effect of RNL. The second decay mechanism is to Tungsten-186, releasing a gamma particle at (137 keV) [35]. This gamma decay event can be imaged using SPECT imaging, as the energy of this decay event is within the imaging window for imaging Technetium-99 decay. The radioactive half-life of Rhenium-186 is 3.72 days, allowing the deposition of energy to take place over the course of multiple days [22].

In preclinical trials, RNL was demonstrated to have high retention at the delivery site in rats. After 20 hours, greater than 50% of the RNL was still present within the rat brains. In rat U87 xenograft models of GBM, it was demonstrated that RNL extended survival from 46 (control) to 126 days (treatment) [22]. Further, the survival of rats was

highly dependent upon dose, with rats receiving greater than 100 Gy surviving significantly longer than rats receiving less than 100 Gy to the local of the tumor. The standard clinical dose to the entire brain for external beam radiation therapy is roughly 40 Gy [36]. RNL is currently in Phase I/II dose escalation trials, under the supervision and direction of Dr. Andrew Brenner M.D Ph.D., at The University of Texas at Health Science Center San Antonio for treatment of recurrent GBM after initial tumor resection [37].

1.5 Models of fluid transport in biological tissues

Medical images are highly useful in conjunction with models of fluid dynamics. In this section, we describe the relevant models used in the development of a model for convection enhanced delivery. The models in this section are informed by medical imaging, such that each model may be run given a patient's specific geometry and using material properties measured directly from patient imaging such as MRI and SPECT/CT.

1.5.1 Darcy's Law

Fluid flow through porous media is a common occurrence in biological tissues. The interstitial fluid which bathes cells is constantly flowing between the pores of tightly packed cells and extracellular structures [38]. The geometry of the extracellular matrix is highly heterogenous, which makes exact models of fluid flow difficult to implement. However, bulk fluid flow through porous media is well-described by Darcy's Law, which states that fluid will flow with a velocity in the direction of decreasing pressure gradient, with a magnitude proportional to the hydraulic conductivity of the medium:

$$\vec{v} = -K\nabla p \tag{1.11}$$

where \vec{v} is the interstitial fluid velocity, K is the hydraulic conductivity of the medium, and p is the continuous pressure field within the medium [38]. Darcy's Law is derived as a simplification of Stokes' Law [39]. In the present work, we utilize Darcy's Law to calculate the steady-state interstitial fluid velocity and pressure in our model of convection enhanced delivery.

1.5.2 Starling's Law

Starling's Law describes the rate of fluid filtration through tissue permeated by capillary structures, and is often used to model the transfer of fluid from capillary space to tissue space. Starling's Law states that the fluid flux entering the tissue intersitium is proportional to relative pressure between the interstitial compartment and vascular compartment, scaled by the total surface area interface between the two compartments:

$$\nabla \cdot \vec{v} = L_p \frac{S}{V} ((p_c - p_i) - \sigma(\pi_c - \pi_i)), \quad 1.12$$

where L_p is the hydraulic conductivity of the capillary wall, S/V is the ration of capillary surface area to volume, p_c and p_i are the capillary and interstitial hydrostatic pressures, π_c and π_i are the capillary and interstitial osmotic pressures, and σ is the capillary wall reflection coefficient [38]. In the present work, we utilize Starlings's Law to incorporate the leaky BBB allowing fluid to leave the brain into the blood stream.

1.5.3 Advection diffusion

The advection diffusion equation describes the time-dependent transport of a solute or particles carried by a bulk fluid phase under the effects of random thermal motion (diffusion) and a bulk fluid flow. The standard partial differential equation form of the advection diffusion equation reads as a time-dependent flux into a differential element composed of the flux due to diffusion, advection, and a local source term. The standard advection diffusion equations reads as,

$$\frac{\partial c}{\partial t} = \nabla \cdot (D \nabla c) - \nabla \cdot (\vec{v} c) + f, \quad 1.13$$

where c is the metabolite concentration, D is the coefficient of diffusion, \vec{v} is the bulk fluid velocity field, and f is a source term [40]. This equation directly models the transport of a well-mixed metabolite, assumed to be dissolved within the bulk fluid [41]. In the case of modeling nanoparticle transport, the nanoparticles are orders of magnitude larger than a metabolite which might be dissolved, and thus will experience a significant restriction in motion, whether due to drag forces or collisions between nanoparticles and cellular

boundaries within the medium [41]. As such, a restriction term, R , may be introduced to reduce the nanoparticle velocity [41]:

$$\frac{\partial c}{\partial t} = \nabla \cdot (D\nabla c) - \nabla \cdot (r\vec{v}c) + f. \quad 1.14$$

We utilize the advection-diffusion equation, coupled with Darcy’s and Starling’s laws to calculate the spatiotemporal distribution of liposomes in a model of convection enhanced delivery.

1.6 Dissertation overview

The overall goals of this dissertation are divided into two largely separate projects, united under the umbrellas of quantitative medical imaging and fluid dynamics: first, *we investigate the accuracy of the Kety-Tofts model of DCE-MRI in the diffusion-limited regime*. The Kety-Tofts model is widely used to parameterize DCE-MRI models, and the resulting parametric maps are widely used to predict response to chemo- and radiation therapy [42]–[44], as well as to parameterize models of tumor growth [45]. However, validation of the measured parameters is difficult to achieve, requiring prior knowledge of the parameters before evaluating a DCE-MRI acquisition. As such, we attempt to investigate the accuracy of this model by comparing a Kety-Tofts parameterization of a simulated DCE-MRI acquisition of a mouse xenograft tumor, to known tissue volume fractions and assigned flow parameters in a digital phantom derived from high resolution histological images.

Second, *we develop a functional framework to model and optimize the delivery of Rhenium-186 liposomes via convection-enhanced delivery to glioblastoma multiforme, calibrated and validated using clinical patient data from an ongoing Rhenium-186 clinical trial*. While models of CED exist for molecular agents, no such models exist for nanoparticles. As nanoparticles are several orders of magnitude larger than molecular agents, they experience a greater restriction of motion, and therefore distribute among a smaller volume than is predicted by models designed to simulate molecular agents. By accurately modeling the delivery of RNL, we seek to maximize the benefit to each

individual patient in the clinical trial by predicting the optimal catheter placement and the resulting distribution of RNL.

1.6.1 Specific Aims

Aim 1: Investigate the effects of slow contrast agent diffusion on the accuracy of the Kety-Tofts model of DCE-MRI analysis

1a. Use histological tumor data (BT474 mouse-xenograft) and the finite element method to build a cell-resolution DCE-MRI model, simulating the transport of contrast agent within a realistic tumor domain.

1b. Compare the known tissue volume fractions and delivery parameters to those obtained by fitting the Kety-Tofts model to simulated DCE-MRI data.

Hypothesis: Slow diffusion of contrast agent within and across voxels decreases the accuracy of the Kety-Tofts parameterization of DCE-MRI data.

Aim 2: In vivo modeling of ^{186}Re -liposome distribution using MRI and SPECT data in GBM patients

2a. Develop a spatiotemporal model of ^{186}Re -liposome distribution, informed with patient-specific DCE-MRI, DW-MRI, anatomical MR, and the location of the ^{186}Re -liposome injection. Longitudinal SPECT data will be used as the gold standard for calibration and assessment of error in model predictions.

2b. Validate the calibrated model of RNL delivery using leave-one-out and Monte Carlo methods to compare predicted RNL distributions to those measured by the gold standard.

Goal: Develop, calibrate, and validate a model which predicts the spatio-temporal distribution of RNL within an individual patient's brain.

Aim 3: Utilize a model of Rhenium-186 liposome delivery to predict optimal catheter placement for individual patients

3a. Develop a flexible framework and objective function that minimizes leakage of injected RNL, while simultaneously maximizing the tumor coverage of the agent.

3b. Identify the optimal delivery location for individual patients using calibrated parameters determined in Aim 2.

Goal: Develop and demonstrate a framework which will predict the optimal delivery location of RNL, which minimizes leakage into healthy tissue, while maximizing tumor coverage.

1.6.2 Significance

In Aim 1, we model an idealized case of DCE-MRI, which assumes minimal flow from vasculature and between voxels, and relies purely on diffusion of contrast agent from blood vessels to perfuse the surrounding tissue. Under these idealized assumptions, we demonstrate that DCE-MRI is incapable of fully describing the transport of contrast agent within tumor tissue, and that the quantities measured by DCE-MRI, even in this idealized scenario. While extended Kety-Tofts parameters are useful as biomarkers and predictors of tumor aggression and treatment response, if the parameters do not accurately measure the quantities it claims to measure, then the model is not an accurate descriptor of the underlying physical phenomena. If the Kety-Tofts model of DCE-MRI is incapable of accurately parameterizing contrast agent dynamics within a tumor, then more advanced models which consider both flow and diffusion, both between and within voxels, are required to accurately represent the physical fluid transport phenomena occurring during a DCE-MRI acquisition.

In Aims 2 and 3, we develop and utilize a model of the delivery of Rhenium-186 liposomes to GBM. A validated model and optimization methodology, as proposed in Aims II and III, would maximize the life-extending benefit of this experimental procedure while simultaneously minimizing the posed risks. Rhenium-186 nanoliposomes are an extremely promising therapeutic for treating GBM. In preclinical studies, RNL was shown to extend the survival of a rat U87 brain xenograft model from 49 days (control) to 125 days (treatment) ($p = 0.0013$) [22]. Animals receiving less than 100 Gy had a median survival time of 48 days, and animals receiving a dose greater than 100 Gy had a median survival greater than 125 days ($p < 0.0001$) [22]. While this treatment is promising, CED has had a

challenging time in the clinic, often hypothesized to be due to poor catheter placement [27], [28], [30]. As the radioactive doses for this therapy are so high, it is imperative to be able to accurately predict the outcome of an RNL infusion to limit leakage into surrounding healthy tissue and maximize tumor coverage.

1.6.3 Innovation

The extended Kety-Tofts model is currently used to provide spatial information on blood flow (and therefore nutrient, oxygen, contrast agent, and drug delivery profiles) in models of tumor growth [44], [46]–[48]. These tumor growth models are built upon the assumption that the parameters derived from this model are accurate. It is clear that the accuracy of this model needs to be rigorously validated, but to do that experimentally would require expensive experiments and microfluidic devices, in order to have prior knowledge of all volume fractions and K^{trans} . A simulated system, derived from histological imaging, circumvents this limitation by allowing for the assignment of known delivery parameters, such as K^{trans} , while also allowing for the volume fractions to be calculated by image-processing techniques. Simulated contrast agent delivery and MRI acquisitions will never replace a physical validation experiment of the Kety-Tofts model, but may guide researchers in designing such experiments by helping researchers select optimal imaging parameters and choose an optimal phantom design.

While mathematical models of convection-enhanced delivery exist, none to our knowledge are designed to model the delivery of nanoparticles [20], [27], [49], [50], which are orders of magnitude larger than molecular agents. Additionally, the current industry standard, iPlan Flow (BrainLab, Munich, Germany), utilizes a particle-based Monte Carlo method for the discretization of the partial differential equations for fluid transport. Monte Carlo methods are slow to numerically converge to the true solution, and prior to convergence may be inaccurate. In the fields of petroleum, aerospace, and biomedical engineering, the standard for accurate modeling of fluid flow is by Finite Element analysis. Finite elements are known to be more accurate and faster to converge than Monte Carlo methods, and have well-studied stabilization methods [40]. The method proposed in the

present work will bring the modeling methods of CED into the modern era of stabilized finite elements for fluid dynamics, which are well-suited to error analysis [51], and calibration to patient data. Further, finite elements are well suited to optimal control and adjoint-based methods of optimization, allowing for procedures to eventually be optimized and controlled in real time, given sufficient computational power [52].

1.7 Dissertation outline

The current chapter provides the necessary background information and motivation for the studies described in the ensuing chapters. Chapter 2 presents Specific Aim I in which the accuracy and validity of the Kety-Tofts is rigorously investigated *via* simulations over a gold-standard domain established from high-resolution histology images of mouse xenograft tumors. Specific Aim 2 is presented in Chapter 3, where a coupled Darcy-Advection-Diffusion model of CED is developed, calibrated, and validated on clinical SPECT/CT data in five patients from an ongoing clinical trial investigating the effect of RNL on extending survival in patients with recurrent GBM. In Chapter 4, Aim 3 is investigated by applying the model developed in Chapter 3 to systematically locate an optimal RNL catheter placement (in the same five patients) that maximizes delivery to the tumor while simultaneously minimizing RNL leakage into healthy brain tissue. Finally, in Chapter 5, we summarize the key results of the Dissertation, their implications, and future directions for each individual Aim.

Extended Tofts-Kety Model

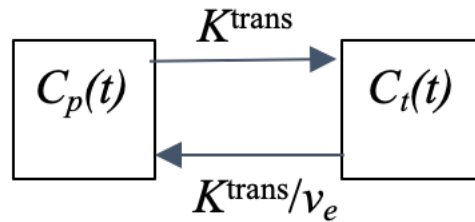


Figure 1.1 Compartment diagram of the extended Kety-Tofts model. Contrast agent may transfer between the plasma compartment to the extra-vascular extra-cellular compartment with a volumetric rate of K^{trans} . Contrast agent may transfer back into the vascular compartment from the extra-vascular extra-cellular compartment by K^{ep} , which is identically K^{trans}/v_e . It is assumed that the AIF is known, so that the only unknown variables in the ordinary differential equation are the volume fractions and transfer coefficients. The resulting ordinary differential equation for $C_i(t)$ is then solved and inverted for these parameters [7].

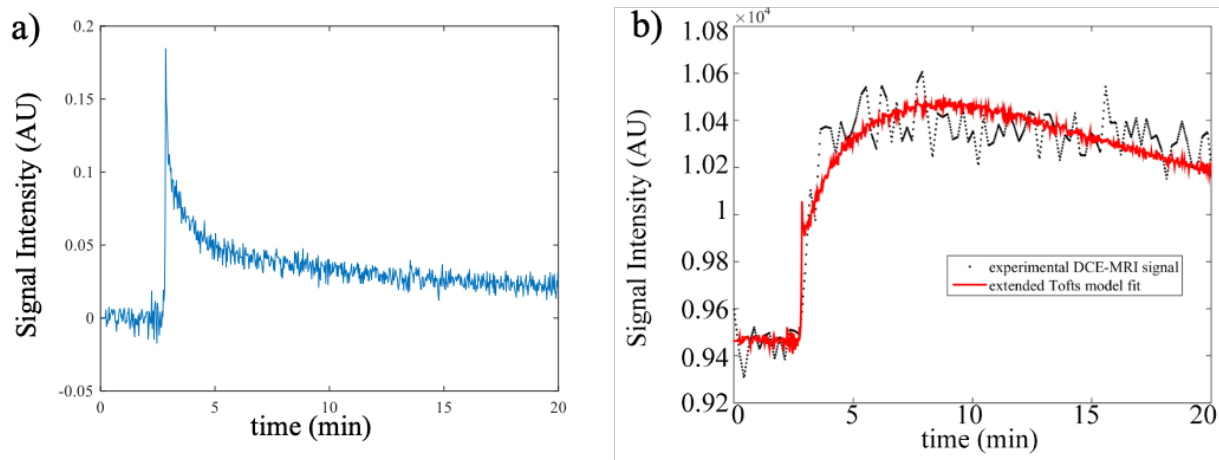


Figure 1.2 Depictions of DCE data. Figure 1.2a depicts a population AIF, which acts as known source term for the Kety-Tofts model. The AIF serves as the known value of $C_p(t)$ in the differential equation. Figure 1.2b depicts a standard DCE- acquisition profile for a single voxel (black lines) and temporal model fit for said voxel (red lines).

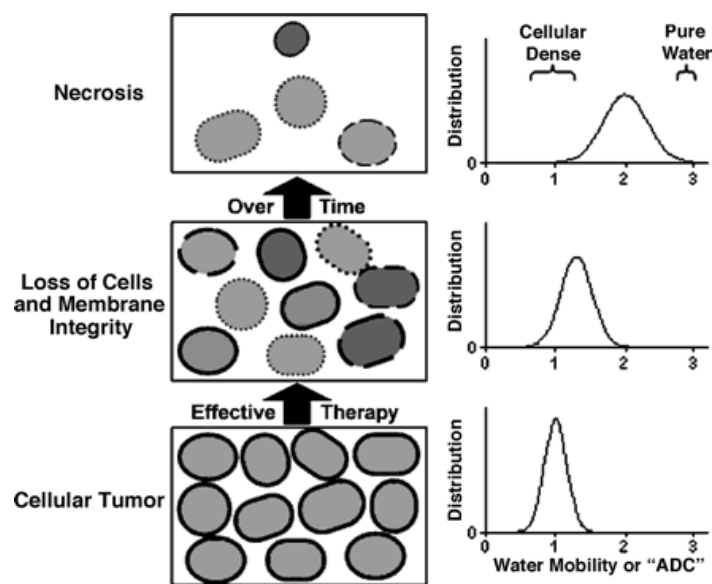


Figure 1.3 Depiction of apparent diffusion coefficient of water with decreasing freedom of diffusive mobility. In the bottom panel, tumor cells and cell walls block the free diffusion of water, restricting its motion, and decreasing the apparent diffusion coefficient of water. As cells die, the membranes which restrict the free diffusion of water break down, allowing water to more freely move, allowing the ADC of the water within the voxel to increase towards the free diffusion coefficient of water. Figure adapted from *Hall et al. Clin Canc Res 2004* [53].

Chapter 2:

The effects of *intra*-voxel contrast agent diffusion on the analysis of DCE-MRI data in realistic tissue domains

2.1 Introduction

Dynamic contrast-enhanced magnetic resonance imaging (DCE-MRI) is performed by acquiring sequential T_1 -weighted images before, during, and after the intravenous injection of a Gadolinium-based contrast agent. As the contrast agent is delivered into a tissue of interest, it decreases the native T_1 relaxation time, thereby increasing the measured signal intensity. As the contrast agent leaves the tissue, the relaxation time returns to the baseline value, as does the measured signal intensity. Thus, each voxel within the image series yields a signal intensity time course that can then be analyzed with a pharmacokinetic model to return estimates of parameters of physiological interest related to (for example) vessel perfusion and permeability and tissue volume fractions [54]. These parameters, which can be obtained on a region-of-interest or individual voxel scale, find application in both diagnostic [55-58] and prognostic [59-62] settings in various cancers. Due to leaky and fragile tumor-associated vasculature, DCE-MRI has a well-established presence in the quantitative imaging of cancer [63-66].

The standard approach to analyzing DCE-MRI data is the two-compartment Tofts-Kety model, which describes the exchange of contrast agent between the vascular and extravascular-extracellular spaces [67]. The utility of the parameters returned from a model is fundamentally limited by the ability of the model to sufficiently and realistically capture the *in vivo* behavior. A fundamental assumption of most DCE-MRI models is that contrast agent is actively delivered throughout each voxel *via* blood vessels, and not through passive *inter*-voxel diffusion. There is an increasing body of evidence indicating that this assumption can lead to significant estimation errors of the desired pharmacokinetic parameters, and extended models accounting for both active delivery and *inter*-voxel diffusion have been proposed [56],[68-71]. These methods show promise in improving the

accuracy of many dynamic contrast-enhanced imaging modalities, particularly those using fast-diffusing contrast agents.

A second limitation of the standard model is the assumption of instantaneous and uniform filling of the extravascular extracellular space (EES). In its original implementation, the Kety model was used to measure the concentration of solvated gasses in the two compartments of interest, and as such, assumes a high molecular diffusivity of the solvate [72]. However, in DCE-MRI, the contrast agent is many times larger than a gaseous molecule and therefore has a lower characteristic diffusivity, D . In fact, the range of D for gadolinium chelates has been measured to be $1-4 \times 10^{-4} \text{ mm}^2 \text{ s}^{-1}$ [73-74], which is multiple orders of magnitude less than that of the typical gases dissolved in tissue ($17-1,010 \text{ mm}^2 \text{ s}^{-1}$) [75-76]. For comparison, the ADC of water in cancerous tissue is typically $0.01-3 \times 10^{-3} \text{ mm}^2 \text{ s}^{-1}$ [59]. This invalidates the assumption that the domain is uniformly filled, and introduces a parameterization error into the model. Barnes *et al.* investigated the effect of *intra-voxel* diffusion on the accuracy of the standard model *in silico*, using simulated domains generated by means of a pseudo-random algorithm for the placement of cells and vessels [77]. It was determined that *intra-voxel* diffusion, within the range of standard gadolinium chelates, introduces significant parameterization error into the analysis of typical DCE-MRI data. They also demonstrated that this parameterization error was eliminated as the contrast agent diffusivity was increased into the gaseous range [77].

The present study aims to rigorously investigate the effects of *intra-voxel* diffusion of contrast agent, within realistic tissue domains derived from *in vivo* tumors, on the accuracy of the pharmacokinetic parameters derived from the extended Tofts-Kety model. We hypothesize that parameterization error due to diffusivity will increase as the coefficient of diffusion of the contrast agent decreases. We predict that this occurs due to slow diffusion away from vasculature, resulting in non-uniform filling of the domain. This is in contrast to the assumption of uniform filling of the extra-cellular compartment. In particular, we predict that there will be significant parameterization errors seen in DCE-MRI analysis when using common gadolinium-based contrast agents. These hypotheses

will be tested by developing a finite element method (FEM) model of segmented histological slices, obtained from BT474 tumors grown in mice.

2.2 Methods

Figure 2.1 provides a visual guide through each component of the experiments and data analysis.

2.2.1 Histological analysis

While details are presented in Sorace *et al.* 2016, the salient features are as presented here [79]. Representative histologically-stained images are demonstrated by Figure 2.1a, and the resulting segmentation shown in Figure 2.1b. All procedures were approved by the Institutional Animal Care and Use Committee. BT474 cells (10^7) were grafted into the hind-flank of adult female *fox nu/nu* mice (Charles River Laboratories, Wilmington, MA), and tumors were allowed to grow for 4-6 weeks, until the size of the tumor exceeded 200 mm^3 . Animals were humanely sacrificed and tumors were immediately excised and fixed in 10% formalin. Tumors were then stored in 70% ethanol for further processing. Serial slices of the tumor ($5 \text{ }\mu\text{m}$ thickness) were taken at the center cross-section of the tumor. Hematoxylin and eosin (H&E, for cell identification) and anti-CD31 (ab28364, Abcam Cambridge, MA, for endothelial cell and vascularity identification) stains were performed on consecutive histological slices. Slides were digitally scanned at $20\times$ resolution ($0.5 \text{ }\mu\text{m}$ lateral resolution) with bright-field microscopy using a Leica SCN400 Slide Scanner (Leica Microsystems Inc, Ariol, Buffalo Grove, IL) [78]. Digitized CD31 and H&E stains from corresponding mice were then registered by intensity-based rigid transformation (MATLAB Image Processing Toolbox, Natick, MA). H&E images were then segmented into cellular and extra-cellular regions using color thresholding in Hue-Saturation-Value (*HSV*) space. Nuclei were first segmented by thresholding the dark blue stain in H&E, while the cytoplasm was segmented from the background by thresholding purple stained H&E regions. To create an initial mask of cellular space, which was later refined, the masks for nuclei and cytoplasm were combined.

The distance transform was performed on the inverse of the cellularity mask (equivalent to a mask of extracellular space), and the resulting image was watershed-transformed to obtain the edges between cytoplasm and extra-cellular space. Likewise, the distance transform was performed on the mask of nuclei, and watershed-transformed to identify the boundary between nuclei and cytoplasm. Finally, each segmented nuclei was morphologically dilated until reaching the boundary between cytoplasm and extra-cellular space, filling in any small holes in the initial mask of cellularity.

CD31 stains were segmented into vascular and non-vascular space using color thresholding to identify epithelial tissue, and a closing operation (dilation followed by erosion) to fill in open space within blood vessels. Red-colored regions were selected using the *HSV* color space, and then converted into a rough mask of vascularity. This rough mask was then refined by morphological closing, closing the lumen of the blood vessels in the vascular mask and removing small holes within vascular regions. Objects smaller than 2 μm in diameter were excluded from the vascular mask to accurately represent the segmentation at the lower finite element resolution.

Registered masks of cellularity and vascularity were then down-sampled from 0.5 μm to 2 μm lateral resolution to achieve a reasonable solve time for the finite element model (FEM; see below). Finally, the mask of extracellular space was modified such each blood vessel has a region of extracellular space 2 μm thick surrounding it. This was done to ensure each vessel could distribute contrast agent to the extravascular extracellular space in all directions, and was not hindered by cellularity directly adjacent to the vasculature. All morphological operations were performed on histological images using a 3 x 3 pixel sliding window. An example of the resulting segmentation is presented in Figure 2.1b. All image processing was performed using the MATLAB Image Processing Toolbox (2016a, Natick, MA).

2.2.2 Finite Element Methods: Forward Model

The following constitutes the forward model, depicted visually in Figure 2.1c. The extended Tofts-Kety model of DCE-MRI is described by the following ordinary, linear, differential equation with constant coefficients:

$$\frac{dC_t(t)}{dt} = K^{trans} C_p(t) - \frac{K^{trans}}{v_e} C_t(t), \quad 2.1$$

where $C_t(t)$ and $C_p(t)$ are the concentration of contrast agent within the tissue and blood plasma compartments at time t , respectively. K^{trans} is the volume transfer rate of the contrast agent from the plasma to the extravascular compartment, and v_e is the extravascular extracellular volume fraction [79-80]. Solving Eq. [2.1] and including a correction factor for a non-negligible plasma volume fraction, v_p [57,80], yields the extended, two-compartment Tofts-Kety model:

$$C_t(t) = K^{trans} \int_0^t C_p(u) \exp\left(\frac{K^{trans}}{v_e}(t-u)\right) du + v_p C_p(t). \quad 2.2$$

If $C_p(t)$ can be measured (or estimated), Eq. [2.2] can be fit to measured DCE-MRI data, using standard, least-squares error minimization, to return estimates for the parameters K^{trans} , v_e , and v_p on a voxel-wise basis.

In order to determine the accuracy of Eq. [2.2] in tissue, we extend the FEM methodology developed in Barnes *et al.* [78]. The diffusion equation in two dimensions,

$$\frac{dC(x, y, t)}{dt} = \nabla \cdot D \nabla C(x, y, t), \quad 2.3$$

is used to disperse contrast agent throughout the extravascular extracellular space, where $C(x, y, t)$ is the 2D spatial and temporal distribution of contrast agent within the domain. The vessel boundary conditions are set such that the flux of contrast agent is determined by an assigned K^{trans} . D is the coefficient of diffusion, or diffusivity (in units of mm^2s^{-1}) of the contrast agent, and is assigned values within the experimentally measured range ($1 \times 10^{-4} < D < 4 \times 10^{-4} \text{ mm}^2 \text{ s}^{-1}$) [73-74]. We approximate the solution to Eq. [2.3] at each

time step through FEM [81-82] using a set of linear, local basis functions $\phi_j(x, y)$, and locally approximated concentration functions C_j :

$$C(x, y) \approx \hat{C}(x, y) = \sum_{j=1}^n C_j \phi_j(x, y), \quad 2.4$$

where n is the total number of elements, $C(x, y)$ is the exact spatial distribution of contrast agent within the tumor domain, and $\hat{C}(x, y)$ is the approximated solution at a single time step within the domain. Time stepping is performed using Crank-Nicholson methodology [83]. This methodology guarantees an exact solution at element vertices (to machine accuracy), and continuous linear interpolation between all vertices within the problem domain.

To implement domain boundary conditions between plasma and extravascular extracellular space, the Tofts-Kety model is implemented:

$$\nabla C \cdot \hat{n} = P(C_p(t) - C(t)), \quad 2.5$$

where P is the permeability, defined as $(K^{trans} V)/S$, with S as the total surface area of the vasculature within the voxel, \hat{n} is the unit normal vector to the boundary, and V as the volume of tissue within the voxel. The concentration within the plasma, $C_p(t)$, is assigned as a constant at each time step, according to a population AIF. Because our simulation is in 2D, S is measured as vessel perimeter (mm), and V is measured in units of area (mm²). For simplicity, P (mm•min⁻¹) is assigned as a constant value for all vessel boundaries within one entire tumor domain, such that the voxel containing the maximum S will have a K^{trans} value of 0.5 min⁻¹, and voxels with no vasculature (i.e., $S = 0$) have a K^{trans} of 0 min⁻¹. This is equivalent to scaling K^{trans} from 0 to 0.5 min⁻¹ as S scales from 0 to S_{max} .

These methods constitute a forward model which is used to simulate the spatio-temporal evolution of contrast agent within the histological FEM domain. By changing the model parameters (K^{trans} , v_e , v_p , D , tissue geometry), the model output (i.e., $C(x, y, t)$) is determined. The forward model output is then analyzed using the methodology outlined below in the *Simulations* section to systematically and quantitatively assess the error in the extended Tofts-Kety model on a voxel-wise basis, when the assumption of instantaneous

and uniform filling of the contrast agent in the extravascular extracellular space is not satisfied. This model was designed such that all the extended Tofts-Kety parameters could be directly measured or assigned. It is not intended to be an exact representation of tumor biology and contrast agent delivery, but an investigational tool which allows fine parametric control in a large variety of biologically relevant geometries under best-case imaging conditions.

2.2.3 FEM Mesh

The mesh developed in this section is used to evaluate the FEM model discussed above (Figure 2.1c). To calculate tissue volume fractions within the segmented histology image that correspond to a typical imaging voxel, down-sampled histological masks were binned into $438 \mu\text{m} \times 438 \mu\text{m}$ pixels to match the in-plane spatial resolution of a typical preclinical DCE-MRI study. The extravascular extracellular volume fraction (v_e) and plasma volume fraction (v_p) were then calculated for each simulated voxel. Vessel surface area (S), (in this case a 1D vessel perimeter) was calculated in each simulated voxel as well. Tissue volume V was measured as the total area of histological pixels in the mask within the voxel. These measured parameters are presented in Figure 2.1d. In all presentation of results, except in Table 2.1 where it is explicitly stated otherwise, truth for v_e is considered to be the fraction of EES accessible to contrast agent, through connectivity to vasculature. Determining connectivity to vasculature was done by first partitioning the mask of extravascular extracellular space into connected regions, and then determining whether each region was connected to vasculature. Regions of extracellular extravascular space not connected to vasculature were counted in the cellular space volume fraction. This was done to ensure the results only reflect error introduced from slow contrast agent diffusion, and not tissue geometry.

To generate a 2D mesh, each pixel in the extravascular extracellular space was divided into two triangular elements in a cross-hatched manner, placing the location of the nodes at the corners of each pixel in the histology segmentation. Boundary elements directly adjacent to vasculature were denoted as “vascular boundaries”, while boundary

elements adjacent to cells and the tumor periphery were denoted as “cellular boundaries”. Contrast agent is permitted to enter and leave the extravascular extracellular space through vascular boundaries (see Eq. [2.5]), while no contrast agent flux is permitted at cellular boundaries. Each element within a simulated imaging voxel is used to then calculate a modeled signal intensity for that region. It should be noted that there are no boundaries between simulated voxels so that contrast agent may flow freely between voxels, representative of in vivo delivery. Elements without a connection (i.e., a physical path) to a contrast agent source were not included in the meshed area for the sake of memory reduction, as the concentration of contrast agent within these isolated pockets of the extravascular extracellular space can never increase beyond zero.

2.2.4 Simulations

The FEM model and compartment model developed above, and their implementation here is represented in Figure 1c. For implementing the forward model, a range of diffusivities, D , for the common, clinically-approved Gadolinium-based contrast agents were chosen as 1.0, 2.0, 2.6 and $4.0 \times 10^{-4} \text{ mm}^2\text{s}^{-1}$ [73]; in particular, $2.6 \times 10^{-4} \text{ mm}^2\text{s}^{-1}$ was chosen to directly simulate a DCE-MRI scan using Gd-DTPA (Magnevist, Bayer, Berlin, Germany) [74]. Each tumor ($n = 4$) was excised, stained, digitized, segmented, meshed, and run through the forward model for with the prescribed values of D . Each time-step was solved using the preconditioned conjugate gradients method on the sparse array of nodal indices. The maximum bound for Δt was selected according to Eq. [2.6], ensuring that it is small enough to capture the dynamic behavior with the given minimum element area, $A_{elm,min}$, and assigned D for the simulation:

$$\Delta t = \frac{4A_{elm,min}}{8D} . \quad 2.6$$

An appropriate values, less than that calculated from Eq. [2.6] was selected for Δt such that the time course utilized in the simulation captured the peak value of the AIF curve.

To calculate signal enhancement for each voxel, at each time point k in the simulation, the total relaxivity of each compartment is calculated and weighted according to its corresponding volume fraction:

$$R_{1,voxel}^k = v_e R_{1,e}^k + v_{eis} R_{1,eis}^k + v_p R_{1,blood}^k \quad 2.7$$

with k corresponding to a measured time point in the population AIF. The longitudinal relaxation rate constant for each element within the extravascular extracellular space, $R_{1,elm}^k$, is calculated as:

$$R_{1,elm}^k = (A_{elm} / area)(r_1 \cdot [CA]_{elm}^k + R_{10,elm}) , \quad 2.8$$

where A_{elm} is the area of the element, $area$ is the area of tissue within the simulated voxel, r_1 is the relaxivity of the contrast agent, ($4.7 \text{ mM}^{-1}\text{s}^{-1}$ appropriate for Gd-DTPA at 7T, [30]), $[CA]_{elm}^k$ is the average concentration of contrast agent within the element, and $R_{10,elm}$ (set to 0.5 s^{-1}) [77] is the pre-contrast relaxation rate constant of tissue. Summing over all elements yields $v_e R_{1,e}^k$ [Eq. 2.7]. We also include the vascular contribution to the signal intensity as:

$$R_{1,blood}^k = r_1 \cdot [C_p]^k + R_{10,blood} , \quad 2.9$$

where $R_{1,blood}^k$ is the longitudinal relaxation rate constant for each element with a blood vessel, C_p is the population AIF [83], and $R_{10,blood}$ (set to 0.5 s^{-1}) [77] is the pre-contrast longitudinal relaxation rate constant of the blood. Contrast agent is assumed to be uniformly distributed within the blood plasma, and is therefore not weighted by element, but rather multiplied by v_p . Finally, the longitudinal relaxation rate constant, $R_{1,voxel}^k$, of the k^{th} time step is calculated by summing up each of the contributions described by Eq. [2.8] and Eq. [2.9] and accounting for the static contribution of the intracellular space (to which CA does not have access) to the R_I :

$$R_{1,voxel}^k = \sum R_{1,elm}^k + (1 - v_e - v_p) \cdot R_{10,elm} + v_p \cdot R_{1,blood}^k . \quad 2.10$$

The expression in Eq. [2.9] is then used with Eq. [2.11] to calculate a simulated signal intensity for each voxel at each time point k (in which we have assumed the echo time, $TE \ll T_2^*$):

$$SI_{\text{voxel}}^k = S_0 \cdot \frac{\sin\alpha(1 - \exp(-TR \cdot R_{1,\text{voxel}}^k))}{1 - \cos\alpha \cdot \exp(-TR \cdot R_{1,\text{voxel}}^k)}, \quad 2.11$$

where α is the flip angle of the DCE-MRI acquisition (25°), TR is the repetition time between scans (5 ms), and, for $S_0 = 1$ for simplicity.

The FEM and DCE-MRI simulations were performed at the Texas Advanced Computing Center (TACC), using the Lonestar 5 system. Each simulation (four values of D over four tumor domains) was run on its own system node, consisting of 12 dual-core processors with 64 GB DDR4 RAM. Each time step completed in roughly 10 seconds, resulting in a total solve time for each simulation ranging from 6 days to 5 weeks, depending on the necessary Δt required for stability (Eq. [2.6]).

2.2.5 Statistical analysis

After computing the signal intensity for each simulated voxel, the time course for each voxel is fit to Eq. [2.2], using least-squares error minimization in MATLAB (MathWorks, Natick, MA) to provide estimates of K^{trans} , v_e , and v_p (akin to what would be calculated on a voxel-wise basis in a standard, in vivo DCE-MRI study). Volume fraction estimates v_e and v_p are bounded between 0 and 1, and K^{trans} is bounded between 0 and 5 min^{-1} . This process is represented by the curve-fitting shown in Figure 1c, and the estimated parameters shown in Figure 2.1f. Finally, these parameters are then compared to the histological (v_e , v_p) and assigned (K^{trans}) parameters, and a percent error is calculated for each simulated voxel (Figure 2.1e):

$$\%Error_{\text{voxel}} = \left(\frac{Param_{\text{voxel}}^{\text{fit}} - Param_{\text{voxel}}^{\text{histology}}}{Param_{\text{voxel}}^{\text{histology}}} \right), \quad 2.12$$

where, $Param_{\text{voxel}}^{\text{fit}}$ represents one of the parameters obtained from curve-fitting the SI time-course (i.e., K^{trans} , v_e , or v_p), and $Param_{\text{voxel}}^{\text{histology}}$ is the same parameter either measured

histologically or assigned in the forward model. $\%Error_{voxel}$ values are then used to determine the accuracy of the standard model. These results are reported as mean \pm the 95% confidence interval, at each simulated D (Table 2.1). Note that voxels with a histological $v_p = 0$ will result in an infinite $\%Error$ in v_p and K^{trans} , due to a zero denominator, and are omitted from the summary of results in Table 2.1. It is important to note that, in all Figures in Chapter 2, the error in v_e has been corrected to reflect the fraction of EES which is accessible to contrast agent and connected to a vascular source. Any EES which is not accessible to the contrast agent is not included in the calculation of the error in v_e , except where it is explicitly reported in Table 2.1.

2.2.6 Domain size analysis

In order to determine the effect of domain size on the accuracy of the standard model, the size of the domain was varied for three different domains. These domains consisted of a single 10 μm diameter vessel in empty EES, a single 10 μm diameter vessel in surrounded by uniformly spaced (6 μm in all directions) 10 μm diameter cells, and a single vessel surrounded by cells made using methods described above in *Histological Analysis*. In each of these domains, the edge boundaries were set to have zero-flux boundaries, and the forward model was evaluated. Initially, the domain consisted of only the blood vessel and the domain resulting from a single morphological dilation (i.e., addition of a single layer of white pixels around the white region of a binary mask) of the vessel. The domain size was then incrementally increased by further dilating the previous domain four times, and then the model was again run to compare fit and true volume fractions as a function of increasing domain size. Each domain was grown until morphological dilation was performed a total of 60 times. Each simulation was repeated for values of $D = 1.0, 2.0,$ and $4.0 \times 10^{-4} \text{ mm}^2\text{s}^{-1}$. Error analysis for each domain was performed according to the methods described in the *Statistical Analysis* section.

2.3 Results

Using a poorly perfused tumor domain (Figure 2.2a, $K^{trans} = 0.05 \text{ min}^{-1}$, $v_e = 0.93$, $v_p = 0.003$), three values of D were used to determine the effects of diffusion. The resulting signal intensity time-courses for these simulated scans are depicted in Figure 2.2b. As D is increased from 1.0 to $4.0 \times 10^{-4} \times 10^{-4} \text{ mm}^2\text{s}^{-1}$, the total amount of contrast agent within the EES increases, corresponding to an increase in total signal enhancement. The results of the FEM simulation for this domain are shown in Figure 2.2c. Initially, at $t = 1 \text{ min}$, the distribution of contrast agent within the voxel is extremely uneven. For $D = 1.0, 2.0 \times 10^{-4} \text{ mm}^2\text{s}^{-1}$, the voxel does not equilibrate until near the end of the simulated experiment. As D is further increased to $4.0 \times 10^{-4} \text{ mm}^2\text{s}^{-1}$, the concentration of the contrast agent within the domain takes less time to equilibrate. Increasing D corresponds with an improvement in parameterization error from -31.8% to -15.5% in K^{trans} , and from -23.7% to -0.2% in v_e . Similar results were observed in a well-perfused voxel ($K^{trans} = 0.18 \text{ min}^{-1}$, $v_e = 0.66$, $v_p = 0.009$) in Figure 2.3a, with increasing total signal enhancement correlating with increasing D (Figure 2.3b). The well-perfused voxel equilibrates much sooner, and with a lower D than the poorly perfused voxel (Figure 2.3c). Parameterization error of K^{trans} improves from -30.3% to 11.7%, error in v_e improves from -5.7% to 3.1%, and error in v_p improves from 49.9% to 4.3%. Absolute error in v_e is notably lower for all values of D in the well perfused voxel (Figure 2.3c), when compared to the necrotic voxel (Figure 2.2c). Errors in K^{trans} are similar between the two sampled voxels, while the error in v_p is more sensitive to changes in D for the well-perfused voxel. The necrotic domain demonstrates a characteristic slow wash-in and lack of notable wash-out (Figure 2b), while the well-perfused domain demonstrates both wash-in and wash-out (Figure 2.3b) [84].

Figure 4 depicts the means and 95% confidence intervals of the parameterization errors for a single mouse tumor (histology and segmentation of tumor shown in Figures 2.5d-f), using the full range of values of D within the physiological range. Mean error in all parameters approaches zero with increasing D . K^{trans} is most often underestimated, with its mean value below zero at all diffusivities simulated in this study. The confidence interval for K^{trans} error begins to contain positive values at $D = 2 \times 10^{-4} \text{ mm}^2\text{s}^{-1}$ (Figure 2.4a).

Likewise, mean error in v_e is negative for all simulated diffusivities, but Eq. [2.2] begins to overestimate v_e at values of $D \geq 2.0 \times 10^{-4} \text{ mm}^2\text{s}^{-1}$ (Figure 2.4b). Error in v_p is by far the most widely varied, although the estimation of v_p improves steadily as D increases (Figure 2.4c). A map of parameterization error in all parameters for $D = 2.6 \times 10^{-4} \text{ mm}^2\text{s}^{-1}$ is shown in Figures 2.5a-c. Areas of high necrosis near the center of the tumor demonstrate high error in K^{trans} . This simulation predicts that DCE-MRI, using the imaging parameters in the *Methods* section, will contain inherent parameterization error of K^{trans} between -32.0 and 8.8%, v_e error between -10.0% and 2.4%, and v_p between 95.6% and 149.9%. Many voxels are present with infinite parameterization error, due to histological $v_p = 0$. These voxels are marked with an “X”, and are not included in the 95% confidence intervals displayed in Figure 2.4. Infinite parameterization error also frequently occurs for voxels on the edge of the tumor domain, where the voxel is not completely occupied by tissue.

The 95% confidence intervals of the errors demonstrated in Figures 2.4 and 2.5, as well as those found in the remaining subjects, can be seen in Table 1. This table summarizes our complete results for each specimen ($n = 4$), at each of the four assigned values of D . In aggregate, the mean error of each parameter improves with increasing D . For $D = 2.6 \times 10^{-4} \text{ mm}^2\text{s}^{-1}$, the K^{trans} is most often underestimated, while the number of voxels overestimated increases with D . The same trend is true of v_e . The parameter v_p is nearly always over estimated, with error reduced with increasing diffusivity. Note that Table 1 also reports v_e error uncorrected for regions without contrast agent accessibility. On average, there is a difference of 20% between values corrected for contrast agent accessibility and raw values without this correction. This difference in error is discussed in detail in the *Discussion* section.

Figure 2.6 illustrates the effect of domain size on parameter error by examining the domain immediately surrounding a single vessel. As the domain surrounding the vessel becomes larger, the parameterization error worsens. Figure 2.6a depicts this phenomenon in a voxel containing no cells (i.e. composed solely of the vessel and extravascular extracellular space) to demonstrate this effect with smooth curves for error in all parameters. In each parameter, error is most sensitive to lower diffusivity, while higher

diffusivity continues to result in the best parameter estimation. Figure 2.6b depicts the same phenomenon with a domain of evenly distributed cells around a central circular blood vessel. The addition of cells increases the rate of error accumulation in K^{trans} and v_e as the domain size is increased. Spikes in the plot of v_e error (Figure 2.6b) are caused by the non-smooth changes in EES and true volume fractions as the domain increases in size. This non-smooth behavior is unavoidable using discretized steps in an irregular domain. Figure 2.6c depicts the process using a domain generated from actual histology; the same trend of accumulating error with increasing window size is apparent with all parameters. Due to the pseudo-random distribution of cells, the spikes in error are more present than in the domain with evenly distributed cellularity (Figure 2.6b). In general, the parameter is most accurately estimated with a contrast agent of higher diffusivity, and the Eq. [2.2] estimation of each parameter worsens as the domain increases in size, thereby increasing the distance the contrast agent must travel in order to fill the domain. This process was performed on a number of other tissue domains and blood vessels, and the same general trend of increasing error with increasing window size was found to hold (results not shown). It should be noted that when v_p is reduced below 0.01 (shown with a dashed vertical line in Figures 2.6a-b), the extended Tofts-Kety model no longer holds [67,85], introducing a high parameterization error in v_p .

2.4 Discussion

The results above are intended to demonstrate the error due to diffusion in the extended Tofts-Kety model, for values of K^{trans} , v_e , and v_p within tumor domains derived from entire histology slices. These methods enable us to examine situations which arise in biological tissues that might not occur in contrived or overly-simplistic models of cell density. Of particular note is the presence of regions within the tumors which, due to the distribution of cells, do not allow for any contrast agent to reach them. Such regions were evident in all four tumors studied, suggesting that there could be pockets of tissue in vivo which will not contribute to contrast agent-mediated signal enhancement. In our calculation of error, regions of extravascular extracellular space with no possible enhancement were

counted in the v_{eis} fraction, and only regions accessible to contrast agent were counted in v_e . When non-accessible regions are accounted for, the extended Tofts-Kety model is 20% more accurate in all cases. Volume fractions with isolated regions of extravascular extracellular space can never be quantified using a model of perfusion, and may be better measured *via* diffusion weighted MRI [86]. However, this effect may be mitigated in real tissue, given that there will be more physical pathways for the contrast agent to diffuse through in three dimensions.

This work focuses on a range of diffusivities D which represents those common for gadolinium based contrast agents. Barnes *et al.* demonstrated that as D increases into the gaseous range, the domain equilibrates within the time-resolution of a typical DCE-MRI experiment, and approaches instantaneous equilibration of contrast agent within the extravascular extracellular space [77]. In particular, with high diffusivity, overestimation of K^{trans} indicates that more contrast agent is present in the voxel than would be indicated by perfusion and permeability alone. Likewise, overestimation of v_e indicates that the washout of contrast agent from the voxel is slower than expected, and that the voxel is leaking into neighboring voxels [84]. While we do show that for some voxels, K^{trans} and v_e are overestimated, our results (Table 2.1, and Figures 2.2, 2.3, 2.5) indicate that K^{trans} and v_e are most often underestimated for gadolinium chelate MRI contrast agents.

Figure 2.2c clearly demonstrates an unequal distribution of contrast agent within the imaging voxel, and a clear relationship between the total concentration, signal intensity, and contrast agent diffusion. With low D , the rate at which the voxel can fill with contrast agent is limited by the bottleneck of high-concentration at the vessel boundary. The extended Tofts-Kety model dictates that the rate of exchange between the plasma and extravascular extracellular compartments is governed by the concentration gradient between those two compartments (Eq. [2.5]). Therefore, if contrast agent is unable to quickly diffuse away from the vessel to fill empty portions of the extravascular extracellular space, the amount of contrast agent entering the domain will be limited due to a small gradient between compartments. Figure 2.5 demonstrates the same phenomenon in terms of distance instead of time. Faster-diffusing contrast agents are able to equilibrate

a larger region of the extravascular extracellular space in a shorter time period, and therefore will more accurately represent the entire voxel on the time scale of a DCE-MRI experiment. Contrast agents which diffuse more slowly will not be able to evenly fill a large region of extravascular extracellular space, and therefore decreases the accuracy of the model.

An example of the error commonly encountered when performing a DCE-MRI experiment, using a temporal resolution of 1.6 seconds, and Gd-DTPA, is depicted in Figure 2.4. The large error in K^{trans} is particularly of note due to its common application in diagnosing [55-58] and evaluating response in cancer [59-61,78]. Thus, an accurate estimate of perfusion is necessary to provide accurate predictions of tumor growth and response to therapeutics. By correcting for the error introduced by diffusion, we hypothesize that accurately estimated parameters will have even more predictive power for diagnosis and prognosis. This will require modification of the extended Tofts-Kety model to account for both inter- and intra- voxel diffusion.

Previous efforts have investigated methods to improve the accuracy of the extended Tofts-Kety model by treating the tumor as a continuum, while accounting for *inter*-voxel diffusion between boundaries [56,68-71]. These models are applicable for using fast-diffusing contrast agents, or for correcting for necrotic regions of the tumor where the only source of signal enhancement is from the diffusion of contrast agent from neighboring voxels. They do not, however, account for the underestimation of K^{trans} and v_e resulting from *intra*-voxel diffusion as demonstrated in the routine pre-clinical DCE-MRI procedures using common gadolinium chelates described in this manuscript.

Our study of intra-voxel diffusion was limited due to stability requirements (Eq. [2.6]); evaluating the forward model for an entire tumor domain at $D > 4 \times 10^{-4} \text{ mm}^2\text{s}^{-1}$ was prohibitively long. By taking advantage of mesh partitioning and parallelization, we could potentially extend our model to analyze contrast agents with diffusivities in the gaseous range ($0.17\text{-}10.1 \text{ cm}^2 \text{ s}^{-1}$) [59,60], although CA in this range of diffusivity would likely not be delivered through injection. Decreasing the simulation time would also allow for simulations of the Tofts-Kety model within the flow-limited regime, as increased contrast

agent velocity would require finer time-steps. For the same reasons, the spatial resolution of our model is limited to 2 μm in the imaging plane, and it is assumed that each blood vessel is surrounded by at least 2 μm of extracellular space. This was a necessary assumption in order to allow contrast agent to enter the domain from all directions from any given vessel. Our model is also limited in that the concentration within the plasma compartment is constant in space, and varies temporally with the given population AIF [83]. This means our analysis is limited to the permeability-limited case of the Tofts-Kety model [79]. This analysis does not accurately reflect well-perfused tumors, in the flow-limited regime of the extended Tofts-Kety model. Rather, our approach is most applicable in tumors with poor vascularization and perfusion. Finally, we offer no immediate solution to eliminate this error from the analysis of DCE-MRI. Potential methods for correcting this model may include the molecular diffusivity of the contrast agent, as well as including prior knowledge of the spatial distributions of vascular and cellular volume fractions within the tumor obtained from other imaging techniques.

Future efforts will investigate the effect of the flow-limited case, requiring alternative treatment of the plasma compartment, K^{trans} , and inclusion of a perfusion term in the FEM. We currently lack a model which would correct for the effects of inter and intra voxel diffusion. Future work may also include methods of parameterizing the spatial distribution of blood vessels within a voxel, as vessel proximity to a voxel boundary plays a central role in inter-voxel exchange of contrast agent. Additionally, future development of a diffusion-corrected inverse model for DCE-MRI is of interest. The work presented is intended to inform the interpretation of results obtained from extended Tofts-Kety analysis of DCE-MRI data until such a model is implemented.

2.5 Conclusion

The purpose of this study was to illustrate the effect of diffusion of contrast agent on parameterization error in the analysis of quantitative DCE-MRI data. By simulating the distribution of contrast agent within an entire tumor domain, we are able to highlight the sources of error which might be seen in a typical DCE-MRI experiment. More specifically,

by using histological stains of cellularity and vascularity, highly realistic tumor domains were generated for FEM implementation of the extended Tofts-Kety model at sub-MRI-voxel resolution. From these simulations, we were able to perform simulated DCE-MRI experiments, compare assigned (K^{trans}) and histologically measured parameters (v_e and v_p) with those estimated by curve-fitting to the extended Tofts-Kety model, and produce a spatial map of parameterization error. Our results show that diffusion plays a measurable and significant role in determining the accuracy of the current widely used DCE-MRI model, and point towards the need for an improved model which accounts for the diffusion of contrast agent within and between voxels.

2.6 Acknowledgements

We thank the Cancer Prevention Research Institute of Texas (CPRIT) for funding through RR160005, the National Cancer Institute for funding through U01CA174706, R01CA186193, and R01CA158079, and the National Institute of Health (NIH) for funding through EB007507. The authors acknowledge the Texas Advanced Computing Center (TACC) at The University of Texas at Austin for providing high-performance computing resources that have contributed to the research results reported within this paper. URL: <http://www.tacc.utexas.edu>

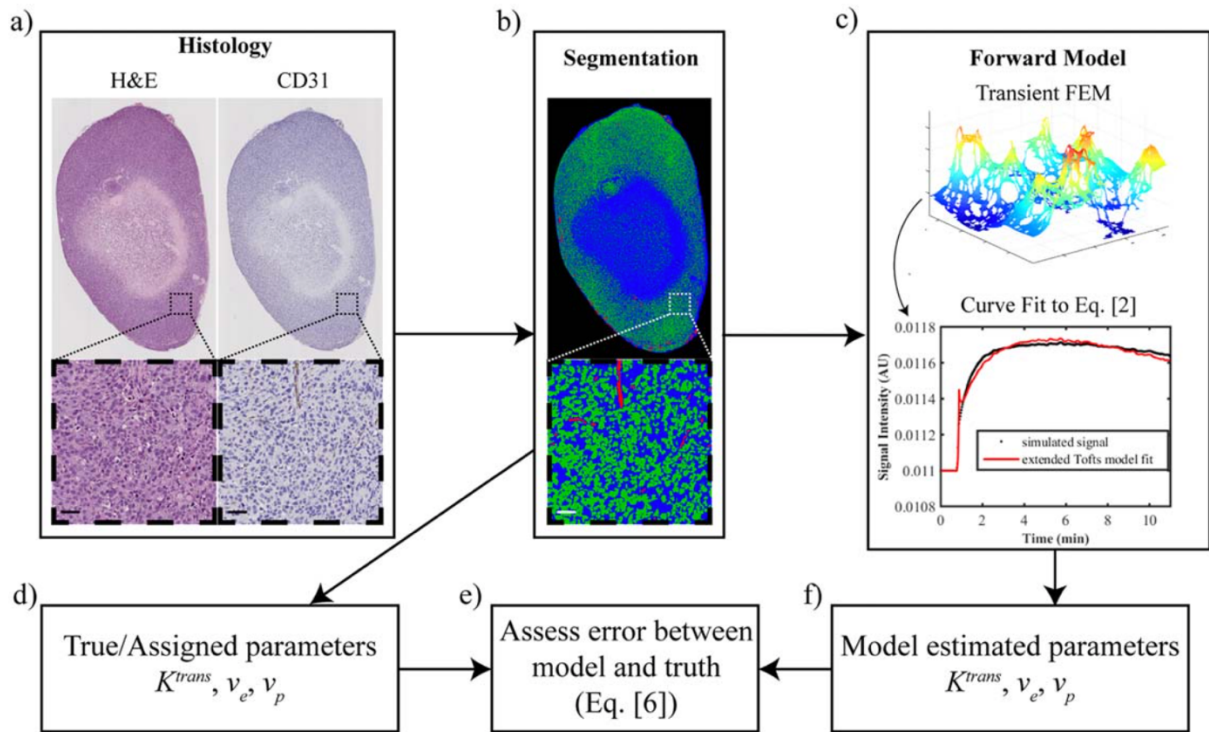


Figure 2.1 Depiction of workflow for developing the simulation domain. Scale bar = 50 μm . Figure 2.1a depicts whole tumor slice stains of cellularity (H&E) and vascularity (CD31) (along with magnified ROIs of a representative $438 \mu\text{m} \times 438 \mu\text{m}$ voxel region). Figure 2.1b depicts whole tumor segmentation after registration and image processing, (along with a magnified ROI of a $438 \mu\text{m} \times 438 \mu\text{m}$ voxel region). Extravascular extracellular space is represented in blue, cells are represented in green, and vessels are represented in red. Figure 2.1c depicts FEM modeling and fitting done to produce a simulated DCE-MRI curve for a single voxel. Figure 2.1d depicts the measurement of model parameters by calculation of volume fractions and Eq. [2.5]. Figure 2.1e shows the comparison of truth and simulated measurements from extended Tofts-Kety analysis. Figure 2.1f lists model parameters obtained from fitting to the simulated signal intensity time-course.

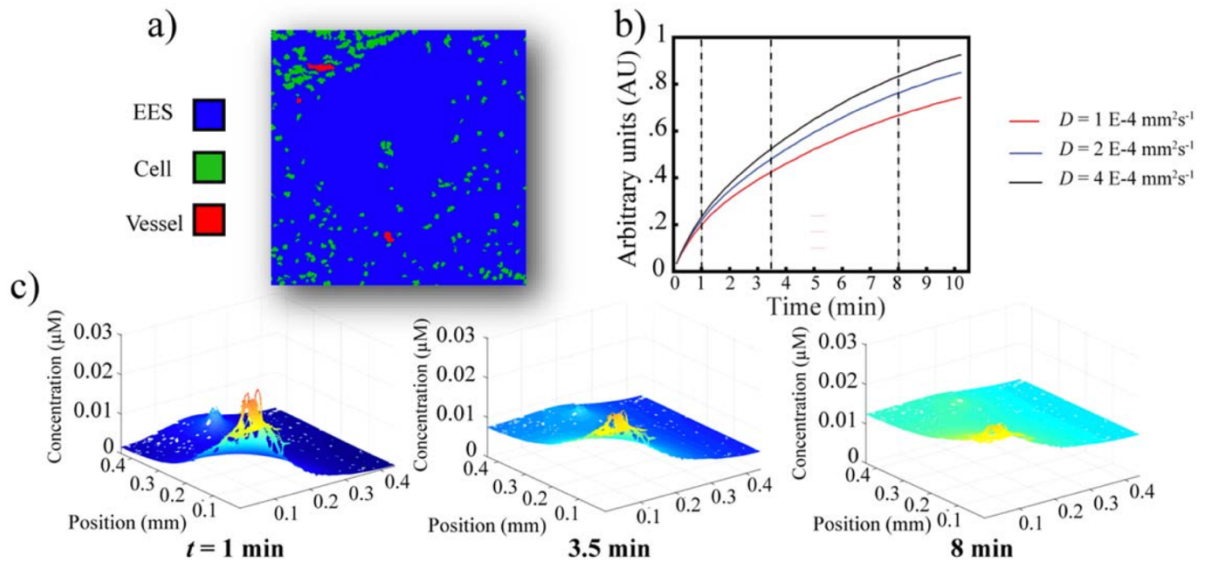


Figure 2.2 Model results from simulations performed on a representative necrotic tissue domain. Figure 2.2a displays segmentation of the necrotic domain into the extravascular extracellular space, cells, and vasculature. The extravascular extracellular space is represented in blue, cells represented in green, and vessels represented in red. Note the large areas of extravascular extracellular space, and sparsely distributed cells and vasculature. Dimensions of the domain are $438 \mu\text{m} \times 438 \mu\text{m}$. Figure 2.2b presents signal intensity time-course, comparing signal enhancement with varying diffusivity. Dashed lines indicate the time-points shown in Figure 2.2c. This voxel exhibits the characteristic slow enhancement and lack of wash-out typically associated with necrotic regions in the tumor. Figure 2.2c shows concentration distributions at sampled time points 1, 3.5, and 8 minutes into the simulated DCE-MRI scan, as well as the associated parametric errors for each simulation. Note that as D increases, the voxel equilibrates sooner and is associated with reduced error in parameter estimation. Underestimation of v_p is due to the true value being $\ll 0.01$ ($v_p = 0.003$).

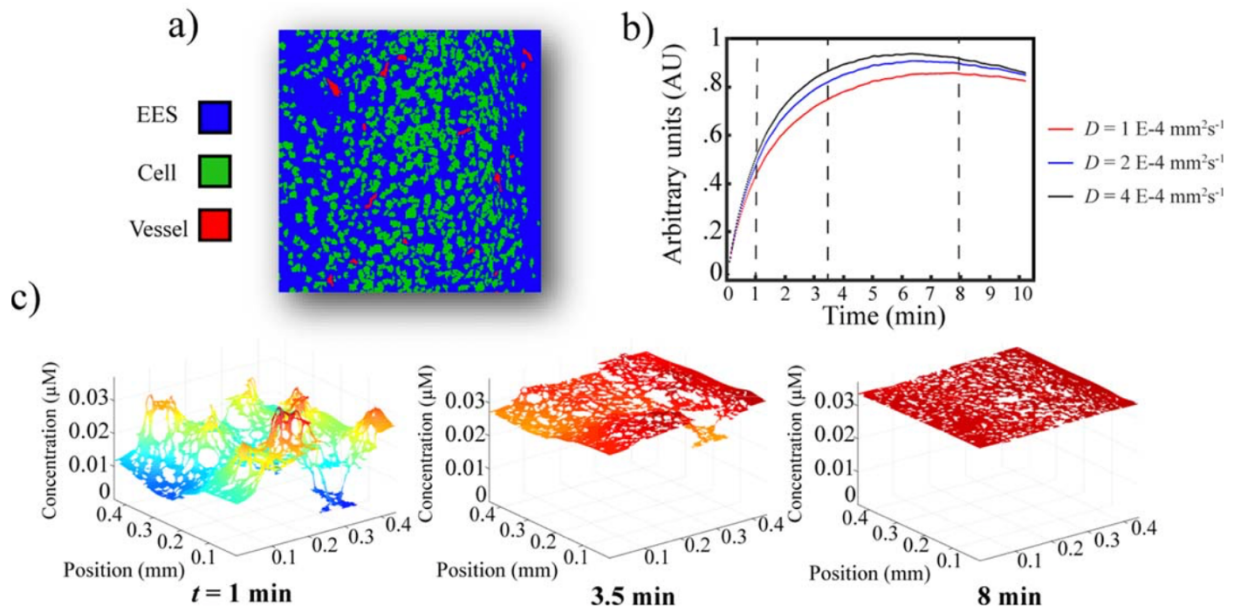


Figure 2.3 Model results from simulation performed on a representative well-perfused tissue domain. Edges of the domain have zero flux boundary conditions. Figure 2.3a displays segmentation of the well-perfused domain into the extravascular extracellular space, cells, and vasculature. The extravascular extracellular space is represented in blue, cells represented in green, and vessels represented in red. Cells and vasculature are more evenly distributed than in Figure 2.2a. Figure 2.3b presents signal intensity time-course, comparing signal enhancement with varying diffusivity. Dotted lines indicate the time-points shown in Figure 2.3c. Note that this domain exhibits a rapid enhancement, and slow washout, typical of a well-perfused voxel. Figure 2.3c shows concentration distributions at sampled time points 1, 3.5, and 8 minutes into the simulated DCE-MRI scan, as well as the associated parametric errors for each simulation. Note that as D increases, the voxel equilibrates sooner and error is reduced. Higher v_p accuracy in the well perfused voxel, compared to the poorly perfused voxel, is due to the increased vascularity the domain ($v_p = 0.009$).

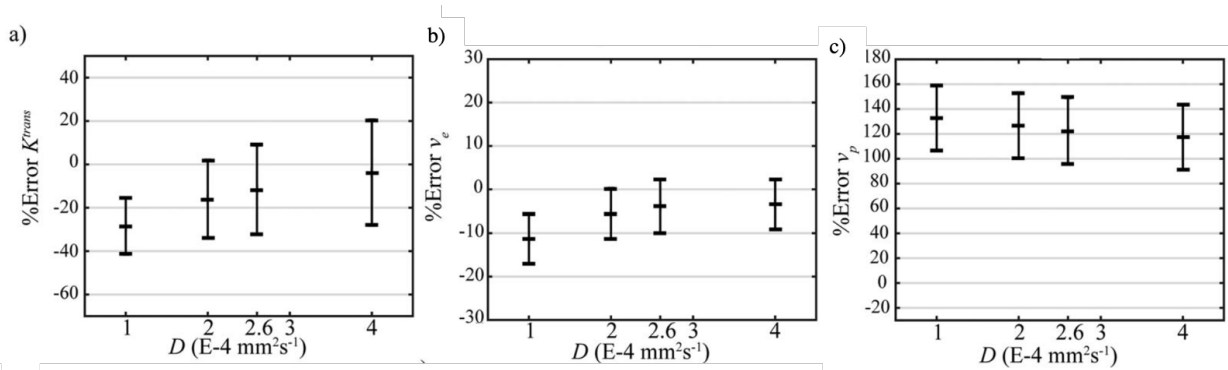


Figure 2.4 Mean and 95% confidence intervals of the parameterization error in a single mouse specimen (see Figure 2.5) for a range of diffusivities. Figure 2.4a summarizes the parameterization error of K^{trans} as a function of diffusivity of the contrast agent. The mean of the measurement approaches 0 for each value of increasing D . As diffusivity increases, the standard model begins to over-estimate K^{trans} , shown with error bars extending above 0%. Figure 2.4b summarizes the parameterization error of v_e as a function of diffusivity. The model more accurately predicts v_e with increasing D , with over-prediction occurring more frequently with increasing D . Figure 2.4c summarizes the parameterization error of v_p as a function of diffusivity. The standard model nearly always overestimates v_p , but becomes more accurate with increasing diffusivity. Note that K^{trans} and v_e are most often under-estimated at the D values used in this simulation.

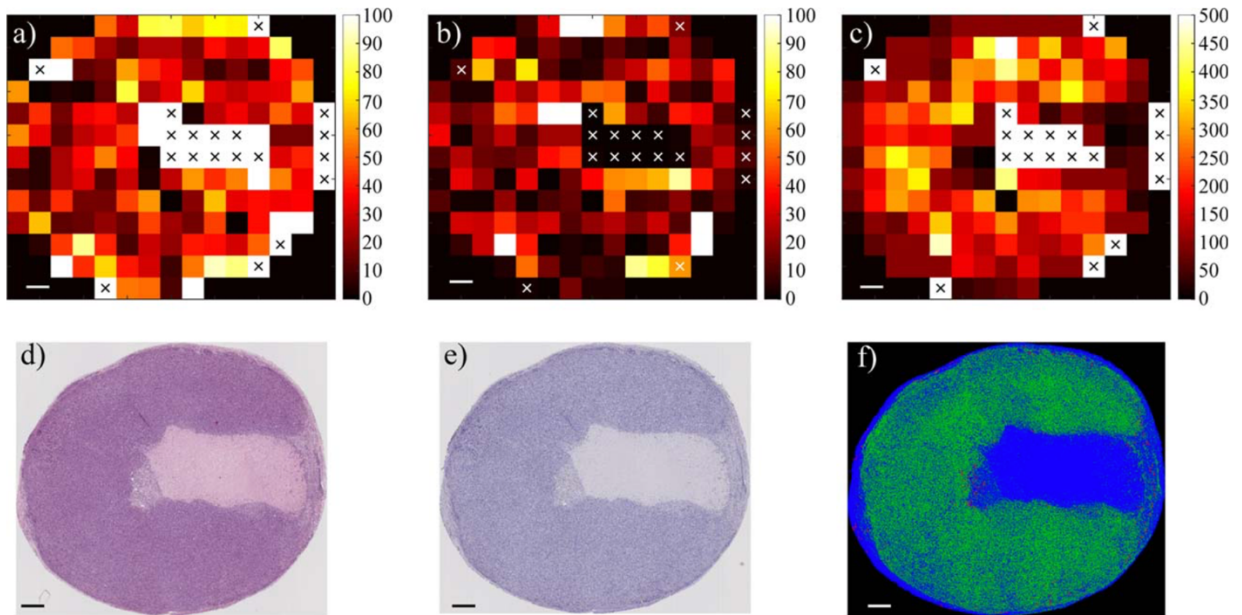


Figure 2.5 Depiction of parameterization error for a single tumor specimen, with $D = 2.6 \times 10^{-4} \text{ mm}^2\text{s}^{-1}$ (appropriate for Magnevist). Regions marked with an “X” do not contain any detected vasculature, and thus result in an infinite parameterization error. Figure 2.5a displays the absolute percent error in K^{trans} . In general, K^{trans} is not accurately measured throughout the entire tumor, with regions of highest error occurring in necrotic regions. Figure 2.5b presents absolute percent error in v_e while panel c shows absolute percent error in v_p . Note that the scale bar ranges from 0 to 500%; error in v_p is considerably higher than in K^{trans} or v_e . H&E and CD31 stains of the tumor are depicted in Figures 2.5d and 2.5e, respectively, while whole tumor segmentation is depicted in Figure 2.5f. Scale bar is the length of a voxel, 438 μm .

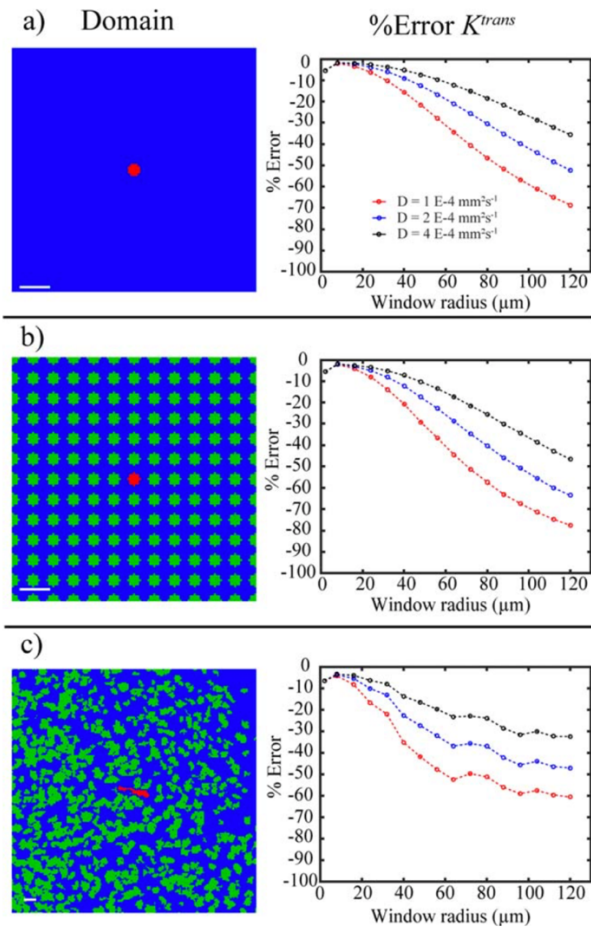


Figure 2.6 Comparison of model accuracy as a function of distance from blood vessel. Starting with the domain shown in Figure 2.6a, only the elements directly adjacent to the blood vessel are included in the simulated DCE-MRI scan. For each data point shown, the initial domain is expanded in all directions using morphological dilation with an 8 pixel neighborhood. The window of elements used in the simulation continues to increase in size, up to $120 \mu\text{m}$ away from the nearest vessel boundary. Figure 2.6a depicts a simple domain containing a single $10 \mu\text{m}$ diameter vessel, and the associated error as the analysis window increases in size. Figure 2.6b presents results from the same procedure performed in Figure 2.6a, but includes evenly spaced cells, both with $10 \mu\text{m}$ diameter, spaced $6 \mu\text{m}$ apart. Note the similar trends in increasing error, with decreased smoothness caused by the addition of cells. Figure 2.6c shows a segmented domain from a section of tumor. Note similar trends to Figures 2.6a and 2.6b, with even further increased noise due to the pseudo-random distribution of cells in the domain. In all cases, the fastest diffusing contrast agent allows for the best parameter estimation with a large window size. At low window size, the model accurately measures the local environment, but begins accumulating error as the domain increases in size and the contrast agent must diffuse further to fill the domain. Scale bar $20 \mu\text{m}$.

<i>D</i> ($\times 10^{-4} \text{ mm}^2 \text{ s}^{-1}$)	<i>% Error K^{trans}</i>	<i>% Error $v_{e,corrected}$</i>	<i>%Error $v_{e,uncorrected}$</i>	<i>%Error v_p</i>
1	-36.9 ± 7.2	-11.3 ± 3.79	-30.1 ± 4.10	93.5 ± 16.1
2	-23.6 ± 9.5	-5.02 ± 3.76	-25.6 ± 4.07	85.2 ± 16.6
2.6	-19.1 ± 10.6	-4.92 ± 3.86	-26.1 ± 4.02	79.5 ± 16.8
4	-10.6 ± 12.3	-1.23 ± 5.22	-24.4 ± 4.03	74.9 ± 16.8

Table 2.1: Summary of parameterization errors over all four tumors

Chapter 3:

Patient specific, imaging-informed modeling of Rhenium-186 nanoliposome delivery *via* convection enhanced delivery in glioblastoma multiforme

3.1 Background and introduction

Glioblastoma Multiforme (GBM) is the most common and deadliest of all primary brain cancers [87-88]. Shortly after diagnosis, patients typically begin treatment and receive maximal allowable resection (to remove the bulk tumor and reduce intracranial pressure), followed by fractionated radiotherapy concurrent with temozolomide [89]. This aggressive treatment regimen results in a median overall survival of 15 months [90]. Despite numerous clinical trials, the standard clinical treatment of GBM has remained relatively unchanged [87-88]. It is nearly impossible to resect all disease, as GBM is highly aggressive, grows rapidly, and initial clinical presentation often requires immediate surgical intervention to release intracranial pressure [90]. Residual invasive disease all but guarantees recurrence, which typically occurs within two years [87,91]. Given the current limitations in successfully treating this disease, especially after the initial treatment course has been completed, there are a large number of aggressive therapies currently in clinical trials, each designed to significantly extend survival (and quality of life) for the patient [92]. One such family of therapies is the local administration of beta radiation for recurrent disease.

Beta radiation provides a strong, local administration of radiation to the site of recurrence, due to the short pathlength (2-4mm) of beta particles, potentially limiting further exposure of healthy brain tissue [91]. One such radiotherapeutic in development is the delivery of Rhenium-186 nanoliposomes (RNL) *via* convection-enhanced delivery (CED) directly to the site of recursion. A promising pre-clinical study, has shown that RNL effectively halts disease progression in the U-87 murine model of GBM, and that radio-nanoliposome retention in the tumor region is much higher than that of molecular

radiotherapeutics [93-94]. This approach is now being investigated in an on-going phase I/II clinical trial (NCT Number NCT01906385) to deliver high doses of radiation, eventually exceeding 20 Gy directly to areas with recurrent disease. The immediate goal of this trial is to treat recurrent tumors and their associated margins with high dose radiation to slow and potentially prevent subsequent recurrent disease, with the ultimate goal of significantly extending mean survival without further surgical resections [93-95].

Many therapeutics delivered *via* CED have had limited success in clinical trials. While the direct delivery of concentrated drug or radioactive agent to the tumor avoids systemic toxicity and bypasses challenges associated with passing the blood-brain barrier, successful delivery and disease treatment is highly dependent on the individual patient and the therapeutic particle being delivered [92]. Jahangiri *et. al* stated that accurate prediction of the spatio-temporal distribution of therapeutic delivered *via* CED is necessary to maximize the chance of success for any given experimental therapy [92]. In particular, they found that less than 50% of patients entered into the PRECISE trial (convection-enhanced delivery of IL13-PE38QQR) had suboptimal catheter placement, and computationally optimized placement might account for the lack of survival benefit expected during the trial [92,96].

Given the high doses of beta radiation delivered by RNL, it is vital to ensure a catheter placement which minimizes the risk of leakage into the cerebrospinal fluid (CSF) and healthy tissue exposure, while simultaneously maximizing tumor coverage. While surgical planning software exists for delivery of molecular therapeutics [97-99], there is no such software tool or model (to our knowledge) specifically designed to predict the spatiotemporal distribution of nanoparticles (100 nm in diameter in the case of RNL) delivered *via* CED. As nanoparticles are orders of magnitude larger in size than molecular agents (~100 nm vs. < 1 nm respectively), there are unique challenges in predicting the delivery of nanoparticles *via* CED. Further, current state-of-the-art computational models of CED rely on particle-based discretization, which is computationally expensive to run, slow to converge, and are highly sensitive to initial conditions and random seeds prior to model convergence [97].

The goal of this study is to define, calibrate, and validate a physics-based computational fluid dynamics model of CED delivery of RNL to recurrent glioblastoma, solved using the finite element method. This approach is designed to account for decreased nanoparticle mobility associated with their larger size in comparison to molecular agents, and utilizes patient-specific pre-operative imaging to derive material properties. The model is implemented using the theory of finite elements, which are stable, deterministic, and ubiquitous in all high-precision fields of science. We utilize a five-patient subpopulation taken from the RNL clinical trial to calibrate and validate our approach. Each model in a family of 12 is calibrated to a gold standard of single photon emission computed tomography (SPECT) images, acquired during and immediately following the infusion of RNL. To assess the validity of each model, a leave-one-out framework is utilized, such that only information obtained prior to a patient's RNL infusion is utilized in making a prediction. Further, while this specific model is developed for the prediction of RNL delivery within the context of the clinical trial, we propose that this framework may potentially be extended to any therapeutic delivered by CED, given the proper data to calibrate and constrain model parameters.

3.2 Methods

3.2.1 Clinical protocol

The patients presented in this study consist of 5 patients from the Phase I/II clinical trial of RNL performed at The University of Texas Health Science Center at San Antonio (UTHSCSA) [95]. The population consists of adult patients suffering from recurrent GBM after an initial tumor resection. While full information on the study (including details on patient population, entry criteria, and full details on image acquisition) can be found in the public clinical trial documentation (NCT Number NCT01906385), here we summarize the salient details relevant to our modeling efforts.

After initial screening and MR imaging are performed (see *Imaging details*, below), a single catheter is surgically inserted intracranially to the site of infusion, and the patient is allowed to rest for approximately 8 hours. RNL is then delivered *via* an automated

syringe pump, initially under a ramp to ensure minimal leakage into the CSF and nearby vasculature, and then at a constant rate of 5 microliters per minute. For the purposes of this study, and due to the minimal amount of RNL delivered during the initial ramp, it is assumed that the rate of delivery is a constant 5 microliters per minute. The total volume of RNL infused and time of infusion for each patient are listed in Table 3.1.

3.2.2 Imaging details

While full details of clinical image acquisition can be found in the public clinical trial documentation (NCT Number NCT01906385), here we summarize the salient details. Each patient undergoes an initial imaging protocol consisting of multimodal magnetic resonance imaging (MRI) for surgical planning. The MR modalities collected consist of T_1 - and T_2 - weighted images, T_2 -fluid attenuated inversion recovery (or FLAIR) images, post-contrast T_1 -weighted, and diffusion imaging (including apparent diffusion coefficient (ADC), fractional anisotropy, and diffusion tensor imaging; though the latter two are not used in the present study). For the post-contrast T_1 -weighted images, patients received Gadovist (Bayer, Whippany, NJ). All images considered in the present study are acquired in the axial direction. MR images are acquired on a Phillips Acheiva 3T scanner using an 8-channel coil.

On the day of the RNL infusion, the patient is placed into a GE Infinia SPECT/CT scanner, along with an imaging standard containing one fifth of the total amount of RNL to be delivered to the patient; the imaging standard is to be used for decay correction and establishing consistency among inter-image intensities. The X-ray CT data (acquired simultaneously with the SPECT images on the same scanner) serves to provide anatomical landmarks for interpretation of the SPECT images, as well as facilitate image registration to the MRI data. SPECT/CT images are collected after half of the RNL volume is infused, and at end-of-infusion (EOI). Further SPECT/CT images are acquired through the following week, to track RNL retention, but those images are not considered in this present study. Field of view and resolution of each imaging modality used in this study are listed in Table 3.2. Further MR image acquisition details are provided in Table 3.3.

3.2.3 Image processing

All image processing is performed in MATLAB 2019a and the Image Processing Toolbox (Mathworks, Natick, MA). Voxels which presented non-physical values (e.g., $ADC < 0$ mm²/s, or SPECT signal intensity < 0) in all imaging modalities are replaced with the mean of the eight nearest non-zero neighboring voxels in the same axial slice. A gaussian filter with a 3×3 voxel kernel is applied to each MR image on each axial slice to reduce noise and smooth sharp gradients in the images. The tumor regions of interest were segmented by hand from the post-contrast T_1 -weighted image, while gray and white matter were segmented *via* a k -means clustering of the T_1 -weighted signal intensity, using three clusters (white matter, gray matter, background) [100]. CSF was segmented using a threshold of ADC values greater than 3×10^{-3} mm²/sec, and validated by comparison to T_2 and FLAIR images [101]. All MR images are registered and resampled using linear interpolation (using the `imregtform` and `imwarp` functions, and ‘multimodal’ option) after rigid registration to the T_1 -weighted image. Registration is performed internally by maximizing the Mattes Mutual Information for every pixel in a transformation [102]. The T_1 -weighted image is then registered to the CT image acquired at EOI, and the resulting transformation is applied to each of the co-registered MR images. The skull-brain boundary is manually identified using the T_1 -weighted image. The region within the skull-boundary is then transformed into an initial mesh (on the axial slice of maximal SPECT intensity) by converting each voxel within the skull boundary into 2 isosceles right triangle elements. This 2D mesh is then refined, according to the procedure outlined in Section 2.5.

SPECT images are first normalized to the total intensity of the SPECT standard within the image, to decay correct and obtain a map of RNL concentration. SPECT images are normalized by dividing the image by the total sum of the signal within the imaging standard. Prior to normalization to the standard, the SPECT images provide a map of radioactive activity as the signal is directly proportional to concentration in any given voxel. After normalization, the signal intensity is directly converted to the concentration of RNL, thus serving as our gold standard for the measurement of the spatial distribution of RNL concentration across time [93-94]. This is done to convert the raw SPECT data, which

is a map of radioactivity, to a map of RNL concentration. X-ray CT images and their corresponding SPECT images are then cropped to a FOV which contains only the skull. These cropped FOVs are then registered to the FOV acquired at EOI. The corresponding cropping and registration transformations are then subsequently applied to the normalized SPECT images.

In order to compare SPECT data to the output of the model, we develop an empirical SPECT PSF for the purpose of simulating a SPECT acquisition. The SPECT point-spread function (PSF) is approximated using a Jaszczak Deluxe SPECT Phantom (Biodex, Shirley, NY). The phantom is imaged submerged in water, and in air, according to the same imaging conditions as an individual patient. A digital representation of the phantom (identical in dimensions to the Jaszczak phantom) is approximated by a 3D voxelized sphere, with uniform intensity, and a resolution 10x higher than the SPECT image (0.442 mm), positioned to match the center of mass between the phantom image and the simulated phantom. The simulated phantom image is then convolved with Gaussian point-spread functions of varying standard-deviations, and down-sampled to match the SPECT resolution (4.42 mm). The summed square-error between the actual SPECT phantom image and the simulated phantom image is minimized. Using these methods, it was empirically determined that the standard deviation of the Gaussian PSF was 5.23 mm which agrees with values previously reported for clinical SPECT scanners [103-104]. This PSF is then applied to all simulated RNL fields to simulate a SPECT acquisition, thereby enabling direct comparison of the predicted RNL distribution to that actually measured from the SPECT data.

3.2.4 Fluid dynamics model

Interstitial pressure and fluid velocity are modeled using the laws of Darcy and Starling, respectively. Darcy's law describes the flow of fluid through porous media (e.g., biological tissue, sand, or granular material):

$$\vec{u} = -K\nabla p, \quad 3.1$$

where $\vec{u}(x)$ is the interstitial fluid velocity, $p(x)$ is the interstitial fluid pressure, and $K(x)$ is the hydraulic conductivity of the tissue. Darcy's law states that fluid velocity is proportional to the gradient of pressure, with a proportionality constant K in the opposite direction of the fastest decreasing pressure. Starling's law describes the pressure loss into capillaries within the tissue:

$$\nabla \cdot \vec{u} = -L_p \frac{S}{V} p + f, \quad 3.2$$

where $L_p(x)$ is the capillary hydraulic conductivity, $S/V(x)$ is the ratio of capillary surface area to volume (L_p and S/V are unidentifiable, so they are combined into a single term), and f is the source term used to introduce the fluid flow from the catheter. Starling's Law is typically used to describe the influx of velocity through capillaries. However in this formulation, the pressure p represents the pressure differential between capillary and interstitial compartments ($p_{cap} - p_{int}$, $p_{cap} \ll p_{int}$) due to the high pressures required for CED, therefore introducing a negative sign into the equation. The catheter fluid flux source term, f , is implemented as a Gaussian with a total mass flux of 5 $\mu\text{L}/\text{min}$, with the mean located at the catheter tip, and a standard deviation of 0.25 mm (such that 95.4% of the mass is distributed within the 1 mm catheter diameter). A Gaussian source term was selected as it is smooth and easier to implement than a point source. Interstitial velocity and pressure are assumed to rapidly equilibrate within the tissue. Mechanical deformation and stiffening of the brain tissue, along with formation of an annular void at the catheter tip are not considered. Pressure is assumed to have equilibrated at the domain boundary, and a zero-slip boundary condition for velocity result in the following Dirichlet boundary conditions:

$$p|_{\delta} = 0, \quad 3.3$$

$$|\vec{u}|_{\delta} = 0, \quad 3.4$$

where δ denotes the domain boundary.

Transport of RNL is modeled as an advection-diffusion system within the skull, using the modified advection-diffusion equation from Jain *et. al* [105-106]:

$$\frac{\partial c}{\partial t} = \nabla \cdot (D \nabla c) - \nabla \cdot (R \bar{u} c) + g, \quad 3.5$$

where $c(x,t)$ is the concentration of RNL at position x and time t , $D(x)$ is the diffusion of RNL within the domain due to random thermal motion, $R(x)$ is a restriction factor which accounts for decreased liposome velocity with respect to interstitial fluid velocity ($R \in [0,1]$), and g is a Gaussian source term identical in shape to f , with a total mass determined by the total normalized RNL intensity divided by the duration of the RNL infusion for each patient. RNL is not permitted to cross the skull boundary, resulting in a Neumann boundary condition for the transport equation:

$$\hat{n} \cdot \nabla c|_{\partial} = 0, \quad 3.6$$

where \hat{n} denotes the normal vector at the domain boundary. The initial condition for RNL concentration $c(x, t = 0)$ is assumed to be uniformly 0.

3.2.5 Numerical implementation and analysis

Eqs. [3.1-3.6] are numerically solved using the finite element method in two-dimensions, on the central axial tumor slice. The 2D finite element mesh is generated on the registered mask of the region within the skull (CSF and brain). Each voxel within then axial slice of maximal SPECT intensity, is then mapped to two isosceles right triangular mesh elements for each of the two masks. The two short sides of each triangular element are 1 mm on a side, corresponding to the size of the T_1 -weighted image voxels. A separate measurement mesh is generated using the SPECT image, with each SPECT voxel corresponding to two isosceles right triangular elements, with short side lengths equal to the SPECT voxel resolution of 4.42 mm. Simulations are performed on the high resolution mesh, but all comparisons between simulation and measured SPECT data are performed after projecting the results onto the lower resolution mesh, corresponding to a simulated SPECT measurement.

The steady-state pressure and interstitial fluid velocity are determined by solving a simultaneous mixed element system of Darcy's Law Eq. [3.1] and Starling's equation Eq. [3.2]. The continuous variational problem is:

$$\langle \vec{u}, \vec{v} \rangle_{\Omega} - \langle p, \nabla \cdot (K\vec{v}) \rangle_{\Omega} = 0, \quad 3.7$$

$$\langle \nabla \cdot \vec{u}, q \rangle_{\Omega} + \langle L_p \frac{S}{V} p, q \rangle_{\Omega} = \langle f, q \rangle_{\Omega}, \quad 3.8$$

where \vec{v} and \vec{u} are second-order Brezzi-Douglas-Marini test and trial functions [107], and q and p are first-order Discrete Galerkin test and trial functions. (The $\langle \bullet, \bullet \rangle_{\Omega}$ notation is used to denote the inner product operator on domain Ω .) Note that the boundary term from integration by parts in Eq. [3.7] has vanished due to application of the Dirichlet boundary conditions summarized by Eqs. [3.3] and [3.4]. The above system is iteratively solved on the high-resolution mesh initially, and the mesh is locally refined until the residuals in p are reduced below 1×10^{-6} N/mm² (Figure 3.3). The resulting refined mesh and steady state velocity field is used in implementing the transient transport model (i.e., Eqs. [3.5] and [3.6]), with implicit forward time-stepping,

$$\langle \Delta t^{-1}(c_{prev} - c, w) \rangle_{\Omega} + \langle R\vec{u}c, \nabla w \rangle_{\Omega} - \langle D\nabla c, \nabla w \rangle_{\Omega} + \langle g, w \rangle_{\Omega} = 0, \quad 3.9$$

where $\Delta t = 1$ min is the simulation timestep, w and c are first-order Lagrange test and trial functions, respectively. However, it is known that this formulation is unstable, and requires stabilization [108]. From a residual perspective, Eq. [3.9] is equivalent to

$$\langle residual(c), w \rangle_{\Omega} = 0, \quad 3.10$$

where it becomes apparent that weak form Eq. [3.9] is a minimization of residuals with respect to a set of test functions w . Stabilization of Eq. [3.10] is performed by adding diffusion in the direction of the velocity streamlines, using the streamline upwind Petrov-Galerkin method [109],

$$\langle residual(c), w + \tau R\vec{u} \cdot \nabla c \rangle_{\Omega} = 0, \quad 3.11$$

where

$$\tau = \zeta(Pe) \frac{2h}{r|\vec{u}|}, \quad 3.12$$

and

$$\zeta(Pe) = \coth(Pe) - \frac{1}{Pe}, \quad 3.13$$

with Peclet number (i.e., the ratio of advective to diffusive flux in an element)

$$Pe = \frac{R |\vec{u}| h}{2D}, \quad 3.14$$

where ρ represents diffusive stabilization basis in the direction of velocity streamlines, τ is a scaling factor determined by both the local element size, h , and Pe such that more diffusive stabilization is applied in regions of high Pe . Again, note that the boundary term introduced by integration by parts in Eq. [3.9] vanishes, this time due to the implementation of zero-flux conditions of Eq. [3.6]. All finite element modeling is done using Python 2.7, using the Fenics 2017.2 library [110], and SuperLu distributed solver method [111].

3.2.6 In silico assessment of model fidelity

To ensure the CFD model converges to a single solution, and becomes more accurate with refinement, we perform a refinement-based convergence analysis [112]. The model is first run on a $100 \text{ mm} \times 100 \text{ mm}$ domain, with a source term located at the center, and boundary conditions described above. The mesh is initially subdivided by 10 triangular elements in each of the two dimensions (10 mm on a short side), the model (i.e., Eqs. [3.7 – 3.14]) is run forward in time, and the spatial distribution of RNL is recorded at mid- and final timepoints. The mesh is then progressively refined, and the model run again, adding 10 to the total number of elements per dimension, until the mesh is subdivided into 400 elements per dimension (0.25 mm on a short side). The L_2 -norm of each progressive model run is calculated between the current iteration and the highest resolution iteration at the final time point. This process is performed for values of hydraulic conductivity of varying orders of magnitude ($K = [10^{-1}, 10^{-2}, 10^{-3}, 10^{-4}] \text{ mm/min}$). The results of this analysis are demonstrated in Figure 3.3.

3.2.7 Model family

Table 3.4 contains a full mathematical description of each of the models in the family which are tested. Models 1 and 2 utilized spatially homogenous material properties. Models 3 and 4 utilized material properties which are linearly weighted by the *ADC* map [107]. Models 5 and 6 weight material properties by exponential weighting of the *ADC* map, such that parameter value for the field asymptotically approaches the calibrated maximum [113]. Models 7-9 utilize bulk material properties for CSF and brain tissue. Models 10-12 further categorize brain tissue into white matter and grey matter. Models 1, 3, 5, 7, and 10 assume a fixed value of $L_p S/V$ which is not fit for. Models 2, 4, 6, 8 and 11 assume a homogenous constant $L_p S/V$ which is a fit parameter. Models 9 and 12 assume $L_p S/V$ is 0 in CSF (congruent with incompressible fluid assumption), but allow for a fit parameter to determine the material property corresponding to the segmented brain region.

3.2.8 Statistical analysis and model selection

The parameters in each model are calibrated to minimize the sum squared error (SSE) between the model results and SPECT gold standard at times $t = 0$, $t = \frac{1}{2}$, and $t = 1$ (times which correspond to the total fraction of RNL delivered). Note, the RNL concentration at $t = 0$ is assumed to be identically zero everywhere. Calibrated parameters are initialized using a multi-start framework to avoid local minima in the objective function. Parameters are calibrated using SciPy (Python 2.7) least squares minimization (`scipy.optimize.least_squares`) [114]. To estimate the gradient of the objective function, each parameter is perturbed by a factor of 1×10^{-4} to approximate an element-wise objective function gradient. These perturbations require a forward solve for each parameter, and are therefore run in parallel. The least-squares algorithm is then run until the change in parameters is less than a tolerance of 1×10^{-4} , the change in SSE (Eq. [3.15]) is less than 1×10^{-4} , or the gradient of the objective function is less than 1×10^{-6} (minimum is reached).

We compare the results of calibrating each model to data from the five representative patients *via* a number of metrics. The quality of the model fit to the data is calculated as:

$$SSE = \sum_t \sum_j (SPECT_j^k - Model_j^k)^2, \quad 3.15$$

where j denotes the spatial index of each voxel in the measured or simulated images, and t denotes the temporal index of the measured or simulated images. The concordance correlation coefficient (CCC) quantifies the deviation from the line of unity of a model's prediction of the spatial distribution of RNL to that experimentally measured from SPECT [115]. A CCC of 1.0 indicates a perfect recreation of the measured data by the model. To compare the shape of the distributions of RNL between the SPECT data and model output, a mask of the RNL is generated using a simple threshold. Voxels are considered to be above the noise floor if their intensity is greater than or equal to 5% of the maximum-intensity voxel for that particular SPECT measurement or simulation. The resulting masks are then compared using the Dice correlation coefficient, which quantifies the overlap between the simulated and measured spatial distributions of RNL, agnostic of the underlying concentration field. A Dice value of unity corresponds to a perfect match between masks, while a Dice value of 0 corresponds to a perfect mismatch between masks [116].

We use two model selection criteria to select the optimal model from the family of 12. The first is the Akaike Information Criteria (AIC) [117] which balances goodness of fitness with the number of free parameters, k , as follows:

$$AIC = n \cdot \ln(SSE) + 2k, \quad 3.16$$

with n , the number of samples (in this case, the number of non-zero voxels). The model with the smallest AIC is selected as the most parsimonious model. Second, we consider which model maximizes the overlap of the simulated and measured RNL distributions (i.e., maximizes the Dice value). This second model selection criteria identifies the model that most accurately matches the spatial distribution of RNL immediately following the infusion.

3.2.9 Validation

To determine the ability of each model to predict the final spatial distribution of RNL in each patient, we employed the leave-one-out method. That is, we would calibrate four of the five patients to a model to yield a distribution of parameter values. These distributions would then be used to assign the model parameters for the fifth patient, thereby enabling the model to be run forward to predict the final spatial distribution of RNL which could then be directly compared to the experimentally measured value for that patient. More specifically, with one patient held back, the mean, μ , and standard deviation, σ , of the model parameters for the remaining four calibrated parameter sets are used to determine a beta-distribution [118]:

$$\beta(x) = \frac{x^{a-1}(1-x)^{b-1}}{\int_0^1 u^{a-1}(1-u)^{b-1} du}, x \in [0,1], \quad 3.17$$

$$a = \mu \left(\frac{\mu(1-\mu)}{\sigma^2} - 1 \right), \quad 3.18$$

$$b = (1-\mu) \left(\frac{\mu(1-\mu)}{\sigma^2} - 1 \right), \quad 3.19$$

where a and b are the beta distribution shape parameters, in terms of the sample mean and variance. The beta-distribution is a generalized monomodal distribution, defined on the interval $[0,1]$, and is used in place of the normal distribution which is defined on the interval $(-\infty, \infty)$. This distribution allows for appropriate sampling of the prior distribution for model parameters which exist between some pre-specified lower and upper bounds. If $\sigma^2 < \mu(1-\mu)$, the beta distribution is replaced with a uniform distribution. Sample parameters are randomly generated from parameter distributions defined by Eq. [3.17], $N = 100$. The forward model is then run using the geometry and imaging data corresponding to the fifth patient that was held back. This approach simulates the results of the model prediction as if the fifth patient were newly entered into the clinical trial. From these 100 independent simulations, a mean and 95% confidence interval are determined on a voxel-wise basis, at

the times corresponding to the SPECT acquisitions. These means and 95% confidence intervals are compared to the measured SPECT data using the CCC, Dice, and SSE.

3.3 Results

3.3.1 Convergence analysis

To determine if we are meshing our domain finely enough, the model is run on a uniform square mesh, with a pressure source at the center. At a resolution of one element per 1 mm in each direction, the global L_2 -norm for pressure is less than 10^{-6} N/mm² for all values of K . Figure 3.3 demonstrates that, upon further refinement, the global L_2 -norm continues to slowly decrease upon further refinement. For the purposes of the current study, a residual of 10^{-6} N/mm² was considered sufficiently refined.

3.3.2 Calibration and model selection

While prediction results are calculated for each of the 12 models, for clarity we present prediction results for only two of the models: Model 1, which has the fewest parameters, and Model 12, which minimizes the mean AIC across 4 of 5 patients, and maximizes the mean Dice across all patients. (Please see the supplemental material for a presentation of all model predictions). Upon calibration of each patient to each model, the AIC , Dice, and CCC were recorded, along with the parameters which minimized the SSE between each patient's measured RNL distribution and the model simulated distribution. Model 12 performed with the highest mean CCC and Dice, ranging from 0.71 to 0.95 in CCC, and 0.84 to 0.97 in Dice. Model 1 performed similarly, with only fitting 3 global parameters, ranging from 0.70 to 0.92 in CCC, and 0.76 to 0.97 in Dice. Model 1 required 3 fit parameters, while model 12 required 8 parameters for a fit, though Model 12 minimized the AIC for each patient except patient 4. The models which performed the worst were Models 5 and 6 (exponentially weighted). Out of all patients, Patient 2 was most closely calibrated with each model iteration, while Patient 4 had the poorest model calibration for each model iteration.

3.3.3 Model prediction

Figure 3.4 presents the Model 1 prediction results for patient 5. As Model 1 does not take into account spatially varying material properties, the predicted distribution of RNL is radially symmetric (Figure 3.4a). Following the leave-one-out approach described above in section 2.9, Model 1 predicts the distribution of RNL with a CCC ranging from 0.70 to 0.94, and Dice ranging from 0.46 to 0.82. Model 1 underestimates the peak intensity at the center of the distribution at both mid- and post- infusion time points by greater than 10% (Figure 3.4a, 3.4b), and the model prediction confidence interval is widest at the center of the RNL distribution (greater than 0.65 AU), near the location where the catheter is placed (Figure 3.4a). The model has regions of high error (underestimating the SPECT data by a factor greater than 90% relative error) near the edge of the brain, where it fails to predict a small leak into the CSF (Figure 3.4a).

Figure 3.5 presents the prediction results from patient 5 for Model 12 which assigns separate material properties to white matter, gray matter, and CSF. Model 12 is able to predict the voxel-wise distribution with CCC ranging from 0.81 to 0.98, and Dice score ranging from 0.47 to 0.84. A full tabulation of calibration results for each model is provided in Table 3.5, and a full tabulation of prediction results from the models selected are shown in Table 3.6. The predicted maximum values for Model 12 overestimates (Figures 3.5a, 3.5b) the RNL concentration by over 20% within the central region of the distribution, in contrast to Model 1 which underestimates the concentration by 12% after the final time point. The region of highest uncertainty in the model prediction for Model 12 is located (greater than 0.70 AU) at the center of the distribution (near the catheter placement site, similar to Model 1), and in CSF within and surrounding the brain (Figure 3.5a). Model 12 recapitulates the leak the CSF surrounding the brain more accurately than Model 1 (Figure 3.5a).

3.4 Discussion

We have presented a family of 12 models which are capable of characterizing the distribution of RNL delivered to a patient's tumor *via* CED. Through calibration, we

demonstrate that we can recapitulate the shape and voxel-wise concentration of RNL to a high degree (mean Dice = 0.91 ± 0.10 , CCC = 0.83 ± 0.10 , Table 3.5) using spatially invariant material properties (Model 1). Upon addition of spatial information, implemented through calibration of material properties determined through pre-operative MRI (Model 12), these metrics improve (mean Dice = 0.93 ± 0.07 , mean CCC = 0.83 ± 0.11 , Table 3.4). Utilizing prior-knowledge from other patients in a leave-one-out method, Model 12 is highly predictive of the distribution of RNL (Dice = 0.69 ± 0.18 , CCC = 0.88 ± 0.12), indicating that this model has potential for predicting the distribution of RNL for future patients within this clinical trial. In addition to predicting the spatio-temporal distribution of RNL, this framework provides a map of model uncertainty that indicates the statistical level of confidence in the model prediction at a local voxel level.

There are a number of improvements which can be implemented in this modeling framework. For example, the model was implemented in 2D but applied to a 3D structure. In spite of this, the predictive ability of the model in this preliminary data set is high, which we attribute largely to the differences between in-plane and through-plane spatial resolution in the imaging data: 0.98 mm versus 5 mm. Similarly, the spatial resolution of the SPECT data (4.42 mm on each side) also fundamentally limits the accuracy of the predictions. The limited spatial resolution afforded by SPECT is, of course, well-known and there is little that can be done at this time. It is possible that calibrating to MR-labeled nanoparticles [119] may be a way to improve the spatial resolution of the input data and this would, in turn, potentially improve the predictive ability of our modeling scheme. Our model also assumes that resting-state interstitial velocity is dominated by the flow due to CED, and resting-state interstitial fluid velocity is therefore ignored. This simplifying assumption may be invalid, particularly in the case of slow, multi-day infusions. The effects of CED on interstitial flow, and its effects on tumor growth is a growing field, and is currently under investigation [120-121].

Given the modest sample size ($N = 5$), the results above should be interpreted as an initial contribution that must be validated in a large patient set that includes patients of

heterogeneous physiologies and outcomes, including those with and without significant CSF leaks. But the positive results in the current data set does warrant further investigation.

Other models of CED have been presented previously [97,99,122-124]. However, to the best of our knowledge, all models currently in use have been developed with molecular agents in mind, and may therefore systematically overestimate the distribution of RNL, especially in the case of nanoliposomes. Additionally, some models utilize literature values for material properties, which apply only in the situations with identical conditions to which the measurement are taken, but may not apply in the case of large molecules, or other assumptions than those used to measure or estimate the material properties in the present work [98,123].

Other modeling approaches (e.g., iPlanFlow (BrainLab, Munich Germany), and those contributed by Raghavan *et. al.*) utilize a linear scaling of the diffusion tensor imaging (DTI) map to inform K as a tensor [97,99,124]. While our model does not utilize the full DTI tensor field, Kim *et. al.* hypothesize that fully informing K with DTI imaging may not be necessary, and that large changes in K , such as those found between boundaries between differing tissue types, are the most important feature to capture in modeling CED [124]. We believe this hypothesis is supported by the fact that Model 12, which uses only segmented tissue types instead of a scaling of the ADC map, was the most accurate at predicting the distribution of RNL on both voxel-wise and volumetric basis. Some models of CED couple tissue deformation at the catheter tip with changes to the hydraulic conductivity [97,99]. While we do not take this phenomenon into account explicitly, it is possible that the empirical nature utilized to determine material properties (i.e. calibration *versus* direct measurement) may account for discrepancies between these methods.

3.5 Conclusion

We have presented a family of 12 models calibrated by patient-specific, multi-modality imaging that is capable of predicting the final spatial distribution of RNL with a DICE score of 0.69 ± 0.18 and a CCC of 0.88 ± 0.12 . We aim to utilize this modeling methodology for the optimization of CED catheter placement, such that tumor coverage

is maximized while healthy tissue exposure is minimized, for treatment of recurrent glioblastoma in the ongoing Phase I/II RNL clinical trial.

3.6 Acknowledgments

We thank the National Institutes of Health for funding through R01 CA235800 and T32 EB007507. We thank CPRIT for funding through RR160005. T.E.Y. is a CPRIT Scholar of Cancer Research. We offer a sincere thank you to all the patients who volunteer to participate in our studies; your strength and courage are examples for all of us.

3.7 Ethical Statement

All clinical data presented in the present study is used by permission of Clinical Trial NCT Number NCT01906385, which is approved and compliant to the ethical standards of IRB, HIPPA, and the FDA.

Patient	Infused volume (mL)	Infusion time (min)	Dose (mCi)	CSF leak?
1	0.66	132	1	yes
2	1.32	264	2	no
3	2.64	528	4	no
4	2.64	528	4	yes
5	2.64	528	4	yes (minor)

Table 3.1: Clinical patient details

Modality	In-plane Resolution (mm)	Slice Resolution (mm)	FOV (voxels)
<i>T_I</i>	1.0	1.0	256 × 256 × 165
<i>T_I+C</i>	1.0	1.0	256 × 256 × 165
<i>ADC</i>	0.98	5.0	256 × 256 × 30
SPECT	4.42	4.42	128 × 128 × 128
CT	1.10	4.42	512 × 512 × 90

Table 3.2: Clinical imaging details

Image	Sequence	TR (ms)	TE (ms)	TI (ms)	α	b-values
T1	Fast field echo	25	2.1	-	30°	-
T1+contrast	Fast field echo	25	2.1	-	30°	-
T2	Turbo spin echo	8,052	100	-	90°	-
FLAIR	Long TR	11,000	125	2,800	90°	-
ADC	Single Shot SENSE	4,390	56	-	90°	800,1000

Table 3.3: Clinical MR image acquisition parameters

Model	Apparent Tissue Hydraulic Conductivity (K , mm^2)	Apparent Liposome Diffusivity (D , $\text{mm}^2 \text{ s}^{-1}$)	Restriction Factor (R , unitless)	Hydraulic conductivity and capillary area to volume ratio ($L_p S/V$, $\text{mm}^2 \text{ N}^{-1} \text{ s}^{-1}$)	Total Parameters
1	$K = \theta_1$	$D = \theta_2$	$R = \theta_3$	$L_p S/V = 0.01$	3
2	$K = \theta_1$	$D = \theta_2$	$R = \theta_3$	$\frac{L_p S}{V} = \theta_4$	4
3	$K = \theta_1 \times ADC$	$D = \theta_2 \times ADC$	$R = \theta_3$	$\frac{L_p S}{V} = 0.01$	3
4	$K = \theta_1 \times ADC$	$D = \theta_2 \times ADC$	$R = \theta_3$	$\frac{L_p S}{V} = \theta_4$	4
5	$K = \theta_1 \exp(-\theta_2/ADC)$	$D = \theta_3 \exp(-\theta_4/ADC)$	$R = \theta_5$	$\frac{L_p S}{V} = 0.01$	5
6	$K = \theta_1 \exp(-\theta_2/ADC)$	$D = \theta_3 \exp(-\theta_4/ADC)$	$R = \theta_5$	$\frac{L_p S}{V} = \theta_6$	6
7	$K = \begin{cases} \theta_1, CSF \\ \theta_2, brain \end{cases}$	$D = \begin{cases} \theta_3, CSF \\ \theta_4, brain \end{cases}$	$R = \theta_5$	$\frac{L_p S}{V} = 0.01$	5
8	$K = \begin{cases} \theta_1, CSF \\ \theta_2, brain \end{cases}$	$D = \begin{cases} \theta_3, CSF \\ \theta_4, brain \end{cases}$	$R = \theta_5$	$\frac{L_p S}{V} = \theta_6$	6
9	$K = \begin{cases} \theta_1, CSF \\ \theta_2, brain \end{cases}$	$D = \begin{cases} \theta_3, CSF \\ \theta_4, brain \end{cases}$	$R = \theta_5$	$\frac{L_p S}{V} = \begin{cases} 0, CSF \\ \theta_6, brain \end{cases}$	6
10	$K = \begin{cases} \theta_1, CSF \\ \theta_2, white matter \\ \theta_3, grey matter \end{cases}$	$D = \begin{cases} \theta_4, CSF \\ \theta_5, white matter \\ \theta_6, grey matter \end{cases}$	$R = \theta_7$	$\frac{L_p S}{V} = 0.01$	7
11	$K = \begin{cases} \theta_1, CSF \\ \theta_2, white matter \\ \theta_3, grey matter \end{cases}$	$D = \begin{cases} \theta_4, CSF \\ \theta_5, white matter \\ \theta_6, grey matter \end{cases}$	$R = \theta_7$	$\frac{L_p S}{V} = \theta_8$	8
12	$K = \begin{cases} \theta_1, CSF \\ \theta_2, white matter \\ \theta_3, grey matter \end{cases}$	$D = \begin{cases} \theta_4, CSF \\ \theta_5, white matter \\ \theta_6, grey matter \end{cases}$	$R = \theta_7$	$\frac{L_p S}{V} = \begin{cases} 0, CSF \\ \theta_8, brain \end{cases}$	8

Table 3.4: List of each member of the model family and their associated and unknown parameters θ_n

	Model	1	2	3	4	5	6	7	8	9	10	11	12
Patient 1	AIC	-188	-186	-187	-185	-186	-183	-241	-292	-292	-305	-333	-338
	CCC	0.85	0.85	0.88	0.88	0.87	0.87	0.87	0.89	0.89	0.89	0.91	0.90
	Dice	0.92	0.92	0.92	0.92	0.92	0.92	0.93	0.94	0.94	0.94	0.95	0.95
Patient 2	AIC	725	727	780	782	886	889	711	713	713	695	693	691
	CCC	0.92	0.92	0.91	0.91	0.89	0.89	0.95	0.95	0.95	0.95	0.95	0.95
	Dice	0.97	0.97	0.96	0.96	0.93	0.93	0.97	0.97	0.97	0.97	0.97	0.97
Patient 3	AIC	1,187	1,190	1,173	1,175	1,308	1,310	1,181	1,169	1,169	1,180	1,185	1,162
	CCC	0.87	0.87	0.88	0.88	0.88	0.88	0.87	0.88	0.88	0.87	0.87	0.88
	Dice	0.96	0.96	0.96	0.96	0.92	0.92	0.96	0.96	0.96	0.96	0.96	0.97
Patient 4	AIC	433.	492	494	459	461	335	337	333	278	280	262	278
	CCC	0.70	0.70	0.71	0.71	0.70	0.70	0.70	0.70	0.70	0.71	0.71	0.71
	Dice	0.76	0.76	0.74	0.74	0.74	0.74	0.81	0.81	0.81	0.83	0.83	0.84
Patient 5	AIC	276	278	298	300	282	269	218	220	218	132	131	128
	CCC	0.81	0.81	0.80	0.80	0.81	0.80	0.82	0.82	0.82	0.82	0.82	0.83
	Dice	0.92	0.92	0.92	0.92	0.92	0.92	0.93	0.93	0.93	0.95	0.95	0.95
Mean	AIC	487	500	512	507	550	524	441	429	417	396	388	384
	CCC	0.83	0.83	0.83	0.83	0.83	0.83	0.84	0.85	0.85	0.85	0.85	0.85
	Dice	0.91	0.91	0.90	0.90	0.89	0.89	0.92	0.92	0.92	0.93	0.93	0.93

Table 3.5: AIC, CCC, and Dice for model calibrations for each patient and model combination

	Patient 1		Patient 2		Patient 3		Patient 4		Patient 5		Mean	
Model	CCC	Dice	CCC	Dice								
1	0.80	0.60	0.91	0.65	0.70	0.49	0.80	0.46	0.94	0.82	0.83	0.60
12	0.84	0.74	0.98	0.79	0.81	0.48	0.83	0.58	0.96	0.84	0.88	0.69

Table 3.6: Prediction results

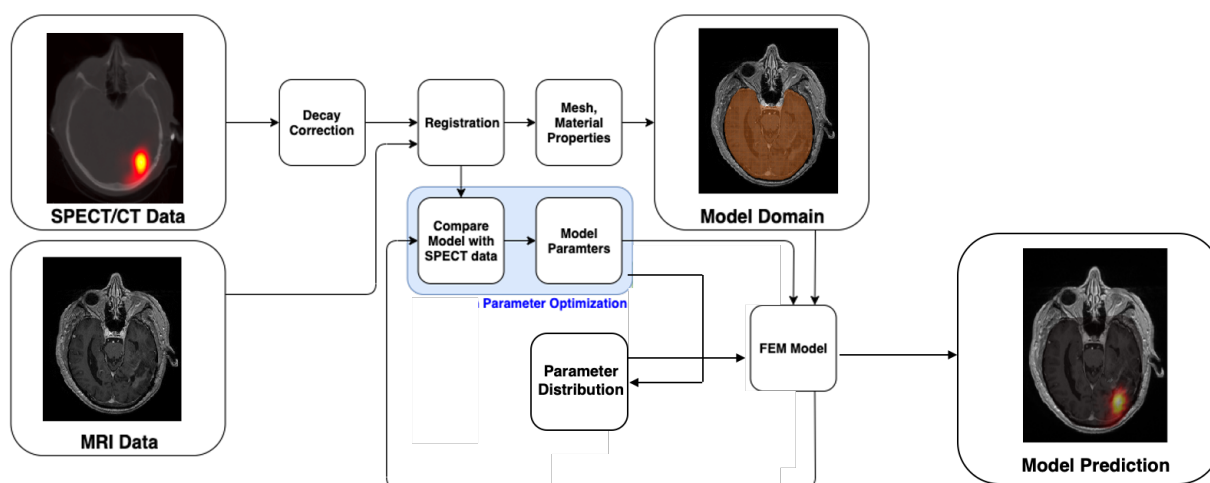


Figure 3.1 Schematic for modeling process. The SPECT/CT and MRI data are first co-registered and used to create the FEM mesh. The model (for one model family) is then run forward using an initial set of parameters. The result of the model is then compared with the SPECT data to determine the error, and the model parameters are updated until the error between model and SPECT data for 1 single patient are minimized. The parameters which minimize the error are then used to create a parameter distribution, which is then used in a leave-one-out Monte Carlo boot-strapping methodology to predict the distribution of RNL.

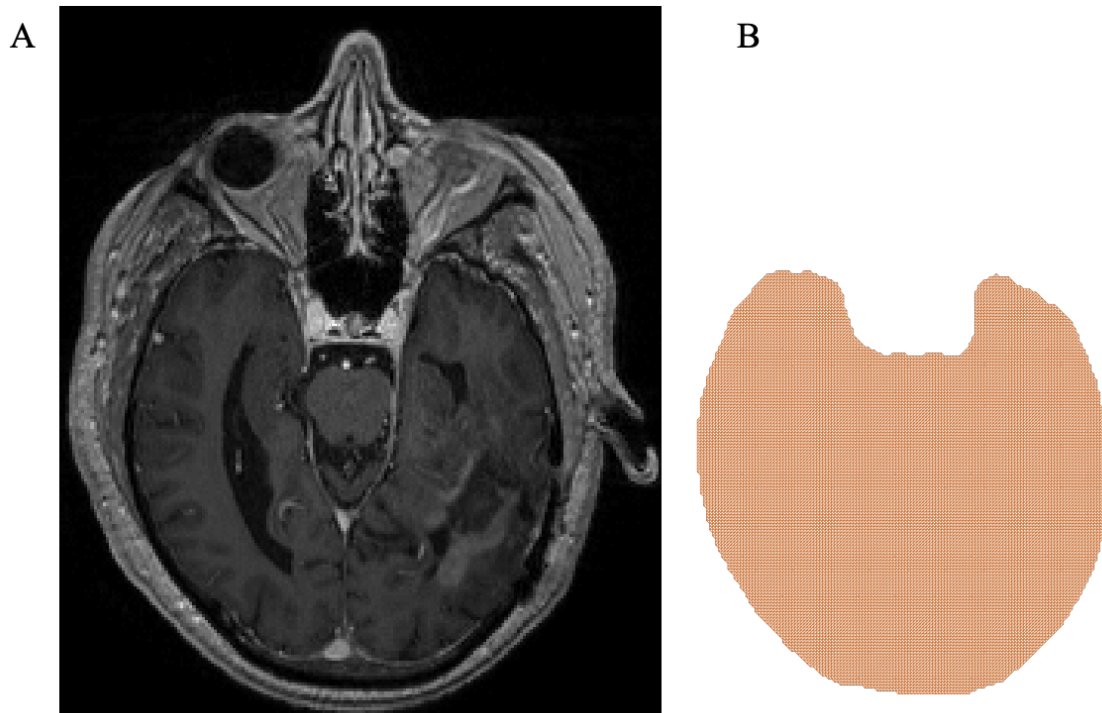


Figure 3.2 Demonstrative T1+contrast image, and its corresponding FEM mesh. Each voxel in the image in panel A is meshed into two isosceles right-triangular elements in panel B. This mesh is then refined until the pressure residuals in each element are below 10^{-6} N/mm², before the forward model is run.

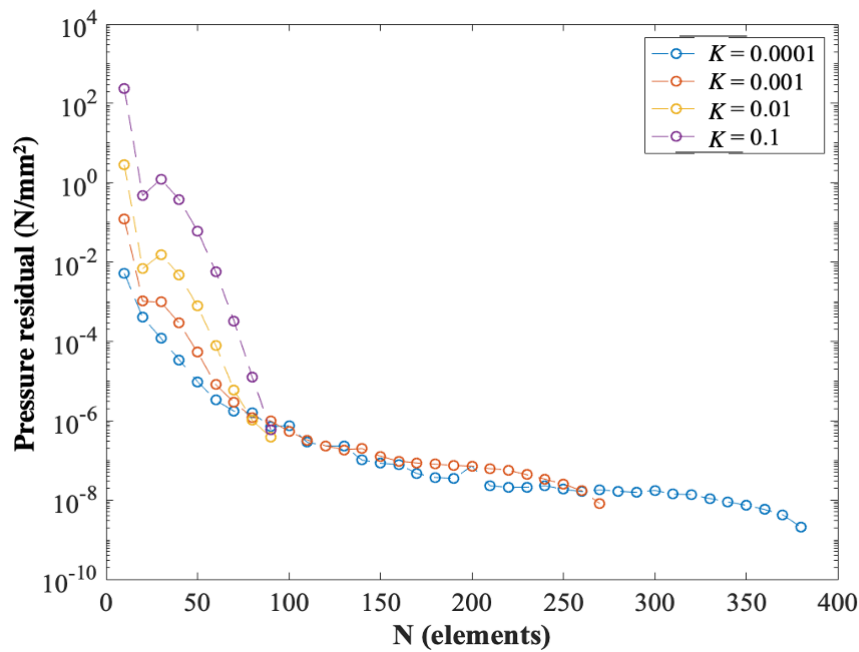


Figure 3.3 Model Convergence with mesh refinement. Depicted are the total residuals (defined as the L-2 norm) of the steady-state pressure field. For all values of K , concentration residuals decrease with increasing mesh refinement. An initial mesh resolution of 1 element per 1 mm (corresponding to $N = 100$ elements per dimension) is selected, as residuals for each value of K are below a tolerance of 10^{-6} N/mm^2 . Further local refinement is iteratively performed on the patient-specific imaging-derived mesh, until the pressure residual everywhere is less than 10^{-6} N/mm^2 . For the purposes of the convergence analysis, the mesh was refined until a residual of 10^{-6} N/mm^2 was achieved, and simulations were truncated early for brevity.

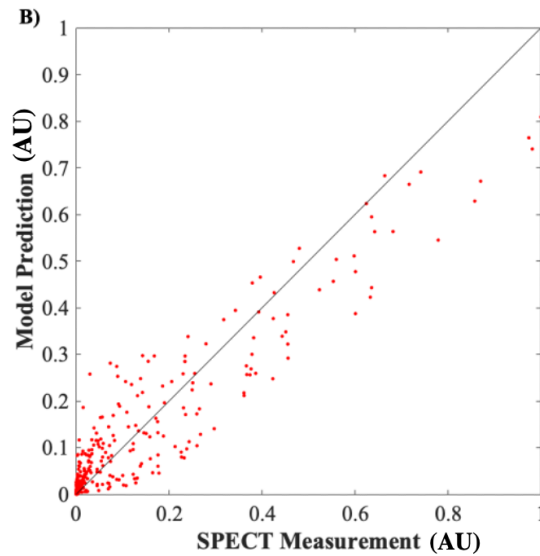
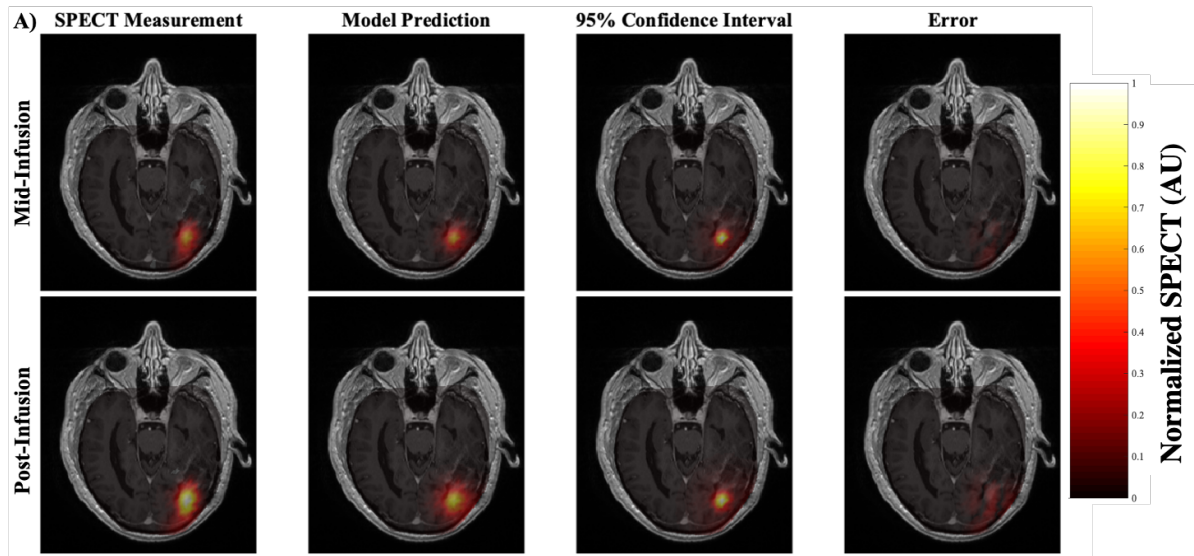


Figure 3.4 Visualization of the Model 1 prediction for (representative) Patient 5. Each image in panel A consists of a heatmap of the model prediction overlaid over on a grayscale, post-contrast, T_1 -weighted image through the central axial tumor slice. Images in the top row of panel A correspond to the mid-infusion time point, and images in the bottom row correspond to the post-infusion time point. The left-most column depicts the true distribution of RNL within the central tumor slice, the second column the mean of 100 simulations from Model 1, the third column 95% confidence interval of the model prediction, and right-most column the absolute value of prediction error. The Dice coefficient between the model and measured SPECT image for the patient shown is 0.82. Panel B depicts the voxel-wise values as red points, with the line of unity shown in black. The CCC for the patient shown is 0.94.

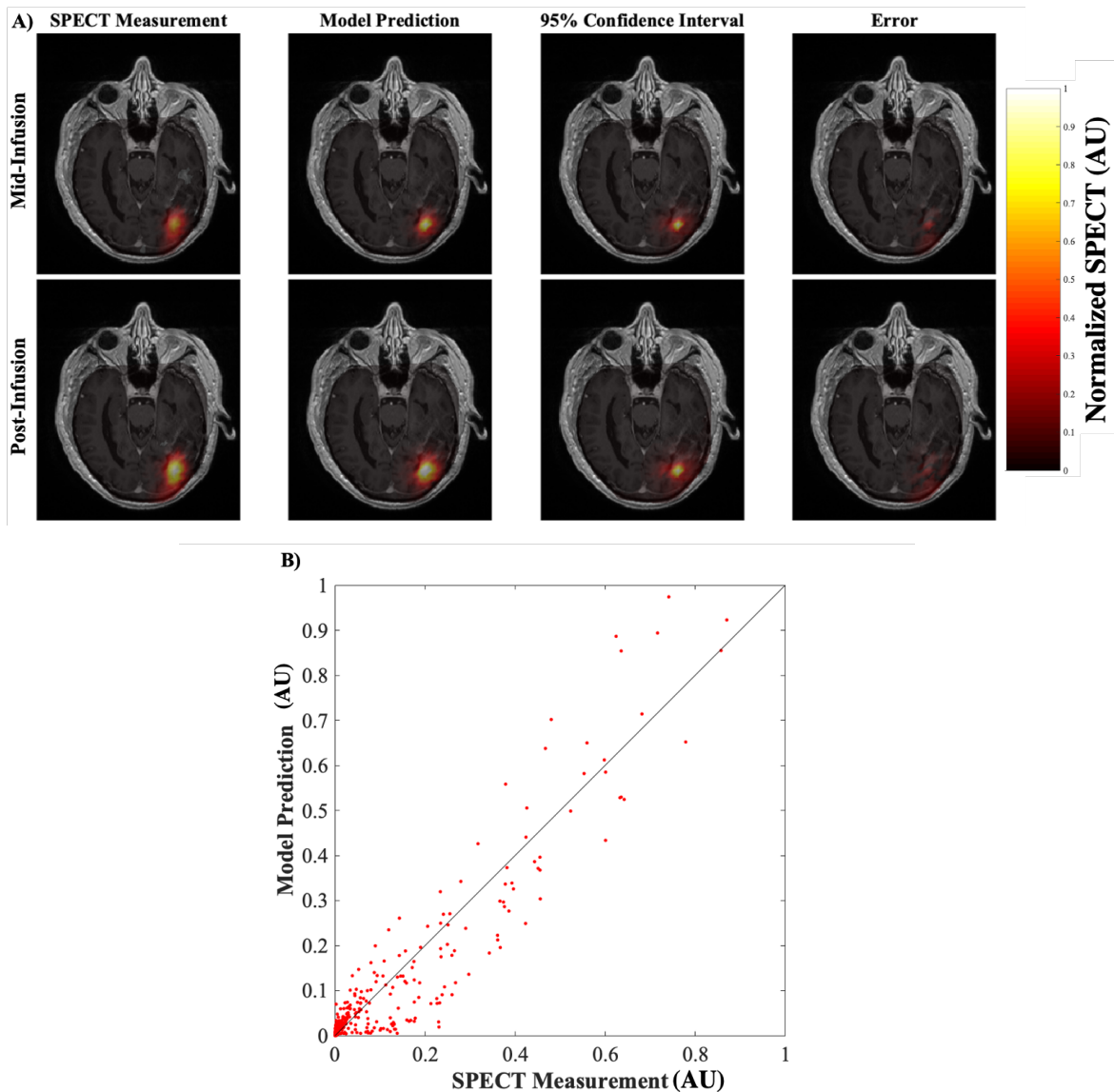


Figure 3.5 Visualization of the Model 12 prediction for representative Patient 5. For each image in panel A, each image consists of a heatmap of the model prediction is overlaid over of a grayscale post-contrast T_1 -weighted image through the central axial tumor slice. Images in the top row correspond to the mid-infusion time point, and images in the bottom row correspond to the post-infusion time point. The left-most column depicts the true distribution of RNL within the central tumor slice, the second column the mean of 100 model predictions, the third column 95% confidence interval, and right-most column the absolute value of prediction error. The Dice coefficient between the model and prediction 5% maximum threshold for the patient shown is 0.84. Panel B depicts the normalized voxel-wise values as red points, with a line of unity (where perfect agreement between model and data would occur) is shown in black. The CCC for the patient shown is 0.96.

Chapter 4:

A framework for optimal catheter placement for RNL delivery

4.1 Introduction

Convection enhanced delivery (CED) is a promising experimental method for delivering drugs to the brain to treat a variety of malignancies; in particular, the approach has found much utility for treating aggressive glioma or glioblastoma multiforme in preclinical trials [125-126]. By injecting therapeutic agents directly into the brain *via* catheter, CED bypasses the blood-brain barrier and achieves greater intratumoral concentrations of the therapy than systemic delivery [127]. Despite its promise, and the advantages over systemic delivery, CED has yet to enter the standard of care [125]. As with any neurological surgical procedure, there are numerous risks, primarily associated with the placement of the catheter, and leakage of high-dose chemo- or radiotherapeutic into cerebrospinal fluid (CSF) and non-diseased brain tissue. As such, planning an optimal trajectory for the placement of the catheter is imperative to maximize the chances of a successful procedure and extend an individual patient's survival.

Selecting a catheter placement for CED requires the balance of numerous factors [128-129]. Primarily, the surgeon must select a location which will maximize the delivery of the drug within the tumor, while simultaneously minimizing leakage into CSF and exposing non-diseased brain tissue [130-131]. Additionally, the surgeon must consider the neuroanatomy of the patient so that the insertion trajectory allows the catheter to be firmly set in place to avoid catheter reflux, while also minimizing the risk of neurological function loss due to compromising the integrity of white-matter tracts [130]. A successful intervention must optimize all of these considerations.

With the long-term goal of assisting the clinician in surgical planning for CED, we present a framework for an algorithm to select the optimal catheter placement, given the constraints listed in the previous paragraph. Using a patient-specific model of CED of Rhenium-186 nanoliposome (RNL) delivery, calibrated and validated in Chapter 3, we present a flexible framework for optimizing the catheter placement and predicted spatial

distribution of RNL for an individual patient. Given a radiologist-determined tumor region of interest (ROI), segmented map of different tissue types from magnetic resonance imaging, we define an objective function that seeks to maximize the delivery of RNL to the tumor, minimize RNL delivery to healthy tissue, and has the capacity to be extended to include additional constraints as determined by the investigator or clinician. The overall goal of this chapter is to systematically investigate the effects of catheter placement on healthy tissue exposure to RNL, the variance of RNL concentration within the tumor, to identify the optimal location for catheter placement on an individual patient basis.

4.2 Methods

4.2.1 Prediction of RNL distribution

To predict the final distribution of RNL for a patient after infusion, we employ the model defined and investigated in Chapter 3 (i.e., Eqs. [3.1-3.14]). The model is initialized with each patient's pre-operative MR imaging data, consisting of pre- and post-contrast T_1 -weighted images, T_2 -weighted images, fluid attenuated inversion recovery images, diffusion weighted images, and the segmented tumor ROI. To complete the parameterization of the model, and allow for predicting the final distribution of RNL, a leave one out approach is employed whereby the data from $n - 1$ patients (where n is the total number of patients) are calibrated to the model, and these parameter values are then averaged and assigned to the patient held back from the calibration process. Using the patient's individualized geometry, together with the $n - 1$ group averaged parameter values, a set of potential catheter positions are selected and the model is simulated forward to determine the resulting final distribution of RNL. For the purpose of this study, the set of potential catheter positions consists of the center of each imaging voxel within the tumor ROI. For each catheter position, the forward model (Eqs. [3.1-3.14]) is run to provide a map of the predicted RNL distribution. The objective function is then evaluated on each predicted RNL distribution.

Once the location of the catheter placement which minimizes the objective function (section 4.2.2) is identified, a Monte Carlo simulation is performed to provide a confidence

interval for the predicted delivery of RNL to the tumor at the objective-minimizing location. The forward model is evaluated 100 times, using parameter sets randomly sampled from the parameter distributions determined in Chapter 3 (Eqs. [3.17-3.19]). The mean concentrations from the Monte Carlo simulation are used to display a predicted concentration map.

4.2.2 Objective function and analysis

The objective functions consist of the sum of two terms, J_1 and J_2 , with the goal of minimizing this function. More specifically, to minimize leakage into the CSF and exposure to healthy brain tissue, we calculate J_1 , the total amount of RNL outside the tumor ROI:

$$J_1 = \frac{\int_{\Omega} cdX - \int_{\Omega_{tumor}} cdX}{\int_{\Omega} cdX}, \quad 4.1$$

where J_1 is the first term in the objective function, c is the concentration of RNL immediately following infusion, Ω is the full domain, and Ω_{tumor} is the region within the tumor. In an attempt to maximize uniform exposure of RNL to the tumor, we calculate J_2 , the total variance of RNL concentration over the tumor ROI:

$$J_2 = \sum_{n=1}^{n_v} (c_n - \bar{c})^2, \quad 4.2$$

where J_2 is the second term in the objective function, i is the index for each voxel within the tumor mask, n_v is the total number of voxels within the tumor mask, c_i is the concentration of RNL within voxel i , and \bar{c} is the mean concentration of all voxels within the tumor mask. These two quantities are combined into a quadratic objective (or loss) function:

$$J = \left(\sum_{m=1}^2 A_m J_m \right)^2, \quad 4.3$$

where J is the total objective function evaluated from a given catheter placement, m is the index for the objective function terms, A_m is the weight term (where $A_1 = 100$, and $A_2 = 1$) and J_m is the objective function term. This general framework was selected to allow for the

inclusion of additional constraints; for example, white matter tracks, as identified from diffusion tractography, may need to be avoided as much as possible. A_1 was selected to be greater than A_2 to prioritize minimization of RNL to healthy tissue over RNL concentration variance within the tumor. A quadratic objective function was chosen such that future optimization schemas could take advantage of their numerous beneficial properties (e.g., guaranteed minimum, and efficient algorithms for objective descent) [132].

To determine the relevant merit of a given injection site, the RNL distribution that minimized the objective function was compared to 1) the surgical placement the patient actually received, the 2) tumor center of mass (COM, to simulate a naïve catheter placement), and 3) a worst-case placement (i.e., the placement that maximized the objective function). For each of the above catheter placements, J is evaluated for each of five patients and compared using fold-change from objective-maximized placement, placement at the tumor COM, and objective-minimized placement.

4.3 Results

4.3.1 Objective function maps

Patients 1-3 (Figures 4.1-4.3, respectively) have tumors which are largely convex (i.e., any two points within the tumor ROI can be connected by a line segment that is contained within the tumor ROI), and have a clear COM located within the tumor itself. The resulting maps of the objective function have clear global minima near the tumor COM, and regions of high objective function near tumor edges, especially near resection cavities (see, e.g., Patient 3 in Figure 4.3). Patients 4 and 5 (Figures 4.4 and 4.5, respectively), have tumors which are highly asymmetric, concave, and have COMs not located within the tumor itself. As such, the objective function map is highly asymmetrical. In the case of Patient 4 (Figure 4.4), there is no clear global minimum, though the optimal placement reduced J_2 by 505% and reduced J_1 by 5.5% from worst placement to best placement. In the case of Patient 5 (Figure 4.5), the objective function has a clear global minimum. The maps of J_1 and J_2 for Patient 3 are depicted in Figures 4.6a and 4.6b respectively. In Patient 3, both J_1 and J_2 are maximized near the resection cavity and at the periphery of the

tumor, and are minimized near the tumor COM. We also demonstrate the predicted concentration of RNL from 100 Monte Carlo simulation, given catheter placements which (Figure 4.7a) minimize J , (Figure 4.7b) at the tumor COM, and (Figure 4.7c) maximize J . J_2 is increased by 334% from best to worst placement, and J_1 is increased by 7.8%, and the overall objective J is increased by 28.4% from best to worst placement. The difference between optimal placement and COM placement is

4.3.2 Optimization comparison

A quantitative comparison of the improvement in all terms of the objective function is presented in Table 4.1. The mean reduction in RNL concentration variance from worst placement to optimal is 315%, and is 67% from COM to optimal placement. The mean improvement in catheter placement for reduction in RNL leakage (J_1 term in the objective function) is 5% from worst placement to optimal, and 0.3% from COM to optimal. The improvement from COM to optimal placement, in terms of leakage for all patients, was less than 1%. The improvement of the entire objective function for Patient 10 was roughly 1.1%, with the remaining patients resulting in an objective function improvement over COM of less than 1%. In overall objective improvement, the mean for all patients from COM to optimal is 0.5%, and the improvement from worst placement to best placement is 14%. Patient 1 had the overall lowest improvement in J from worst to best, while Patient 3 saw the highest improvement.

4.4 Discussion

In cases with a clearly defined and largely convex tumor, the objective function is clearly defined, and the minimum value of the objective function is easily identified as a global minimum (see patients 1-3, Figures 4.1-4.3). For tumors which are highly concave or irregularly shaped, the objective function is more complex, and locating a global minimum may be difficult (see patients 4-5, Figure 4-5). However, the resulting distribution of RNL for local minima could be compared, and maxima (Figures 4.4-4.5) can be easily avoided, providing additional information to the surgeon. We anticipate that

the benefit of a visual objective function is most useful in tumors with an external COM, or whose primary bulk is along the boundaries of a resection cavity. The objective function in nearly all other cases improves by less than 1% when compared to the tumor COM, indicating that the objective function may be more useful in excluding regions of high risk of poor tumor coverage (high RNL variance within the tumor), and less valuable (in its current state) as a tool to determine the optimal placement. Future implementations of this model may incorporate the predicted radiation field and down-stream models of tumor progression, enabling the catheter to be placed in a location which minimizes future tumor progression [133-135].

While there is a rich history of optimization for external beam radiation therapy [135-137], computational methods for the optimization of catheter placement are sparse [128]. The current methodology utilized is for the clinician to select a number of potential catheter trajectories, and the results are then predicted using iPlanFlow (BrainLab, Munich, Germany). While iPlanFlow is capable of detecting poor catheter placements by comparing catheter trajectories with DTI tractography and identifying poor tumor coverage and potential leakage, it does not (to our knowledge) utilize these metrics to determine a spatial map of placement optimality. Additionally, iPlanFlow is designed to model molecular agents, and has not been calibrated to predict the delivery of much-larger nanoparticles, while the methodology presented is calibrated with data collected from nanoparticle delivery [138].

We have presented a preliminary framework which is capable of providing critical guidance on placing a catheter for CED. This framework is limited, in that the underlying model and patient-derived parameters used to estimate the distribution of RNL, are calibrated using a small preliminary cohort of five patients. This model and optimization scheme is also presented in two spatial dimensions, whereas advection for CED, as well as the geometry of the brain and tumor, are all inherently three-dimensional. However, ADC images used are acquired with a slice thickness of 5-mm, and an in-plane resolution of 0.98 mm, a 2D approximation may not significantly differ from a full 3D simulation, and 3D simulation would be difficult to perform with anisotropic voxel sizes. Further, the current

results only reflect the location of the tip of the catheter, and not the full 3D catheter trajectory from the skull to the tip of the cannula. As such, information regarding the 3D placement of the catheter is not considered. Future investigations will need to expand the underlying model to three spatial dimensions, include a larger sample size (potentially from a cancer imaging database), and consider other factors such as avoiding trajectories which cross vital functional regions of the brain identified by DTI tractography [139]. The methodology may further be extended to optimize for syringe-pump pressure, even taking a time-integrated optimal control approach [140], or incorporating the placement of multiple catheters.

These results, while preliminary, demonstrate the potential functionality of a methodology which would predict an optimal catheter placement for a patient undergoing CED of RNL for a recurrent GBM. This method not only provides an estimated optimal catheter placement, but may also provide additional useful information by providing a spatial map of the objective function. This map may allow clinicians to identify multiple potential locations and help them to avoid regions with a high risk of leakage, or regions where full tumor coverage would not be achieved. We hope that further iterations of this methodology will help to maximize the benefit to each individual patient, and help identify patients whose tumors and brain geometries may not have a high chance of treatment success. These methods were designed for and calibrated using data from for the ongoing RNL clinical trial, but we anticipate that this methodology and underlying model could be adapted to fit any theranostic agent which can be measured by medical imaging.

4.5 Conclusion

We demonstrate a functional framework to optimize the placement of a catheter for CED of RNL. In two dimensions, we perform an exhaustive search for the location which simultaneously minimizes the chances of predicted CSF leaks and minimizes uneven tumor coverage. With preliminary results, we reduce the amount of leakage by a factor of 5.2%, and reduced concentration variance within the tumor ROI coverage by a factor of over 300%, when compared to the naïve choice of center of mass. Using this framework, we

hope to improve the outcomes of future studies investigating the efficacy of RNL in GBM patients, and maximize the potential life-extending benefit of this experimental procedure for each individual patient.

4.6 Acknowledgments

We thank the National Institutes of Health for funding through R01 CA235800 and T32 EB007507. We thank CPRIT for funding through RR160005. T.E.Y. is a CPRIT Scholar of Cancer Research. We offer a sincere thank you to all the patients who volunteer to participate in our studies; your strength and courage are examples for all of us.

4.7 Ethical Statement

All clinical data presented in the present study is used by permission of Clinical Trial NCT Number NCT01906385, which is approved and compliant to the ethical standards of IRB, HIPPA, and the FDA.

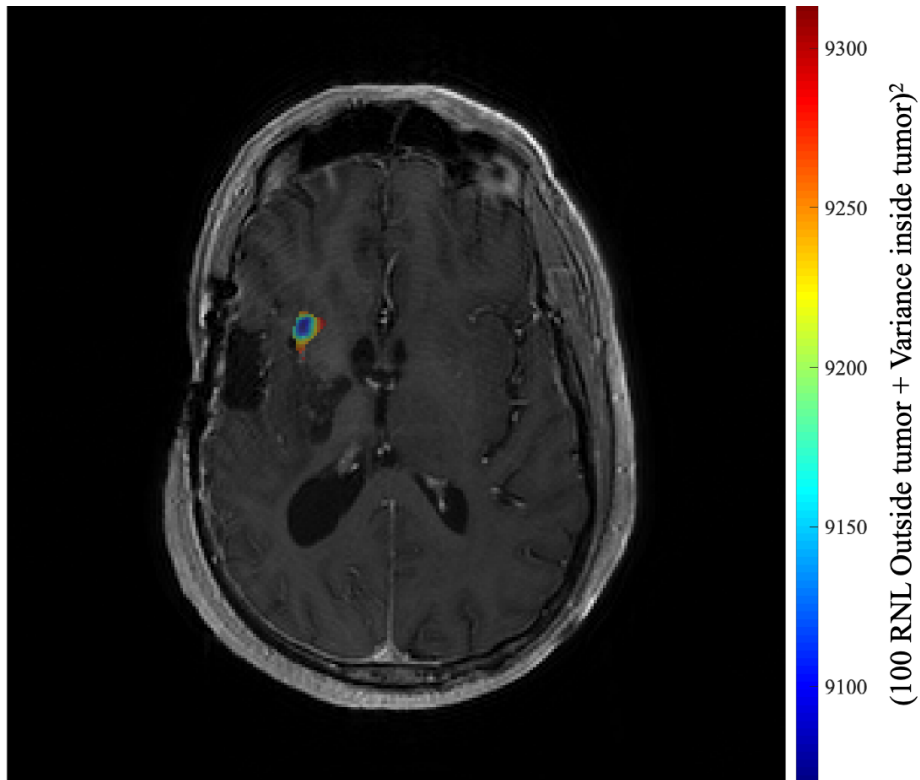


Figure 4.1 Objective function overlain on T_1 + contrast image for Patient 1 on central tumor slice. Patient 1 has the smallest tumor out of the preliminary cohort, and as such the optimal catheter placement is near the center of mass. Regions on the branching structures of the tumor have an objective function value greater than 9300, indicating that these regions would allow excess RNL to escape into the surrounding brain tissue.

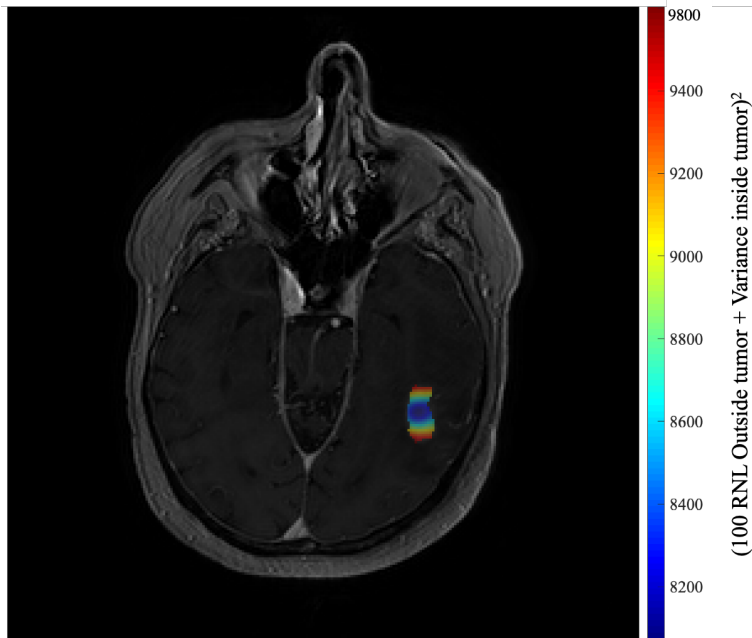


Figure 4.2 Objective function overlain on T_1 + contrast image for Patient 2 on central tumor slice. The tumor present in Patient 2 is largely symmetrical, and convex, indicating a clear objective global minimum near the tumor center of mass. Regions near the edges of the tumor in red (objective greater than 9400), are regions where total tumor coverage would not be achieved, and where maximal leakage into the surrounding tissue is predicted to occur.

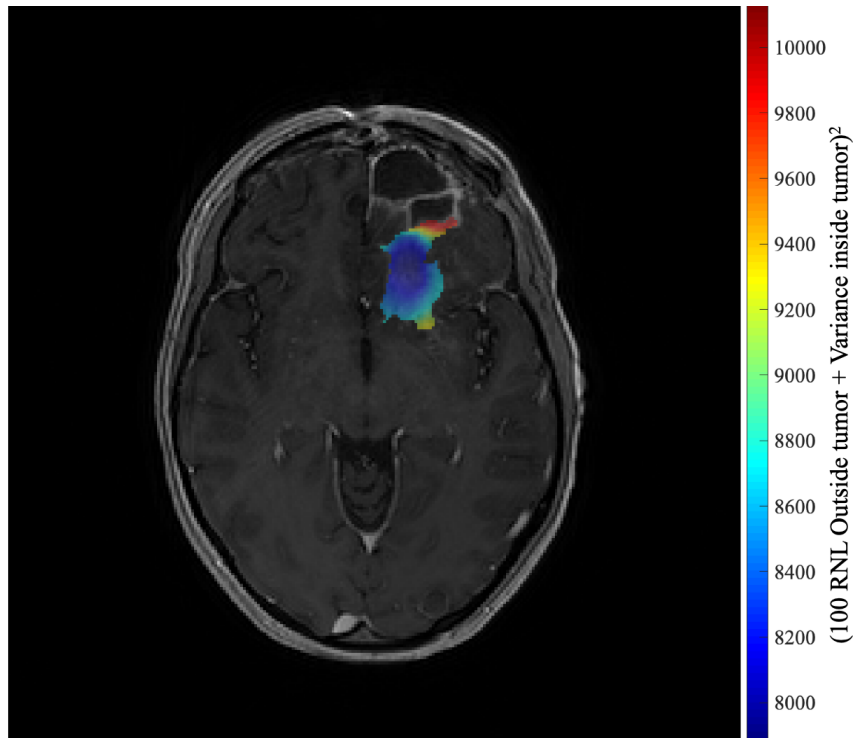


Figure 4.3 Objective function overlay on T_1 + contrast image for Patient 3 on the central tumor slice. The tumor of Patient 3 is located directly adjacent to a large prior resection cavity. The region of highest objective (objective > 9600) is located in a branch closest to the resection cavity. This indicates that catheter placements near this region could result in poor tumor coverage (minimized RNL variance), and leakage into the resection cavity. A global objective minimum is observed near the tumor center of mass.

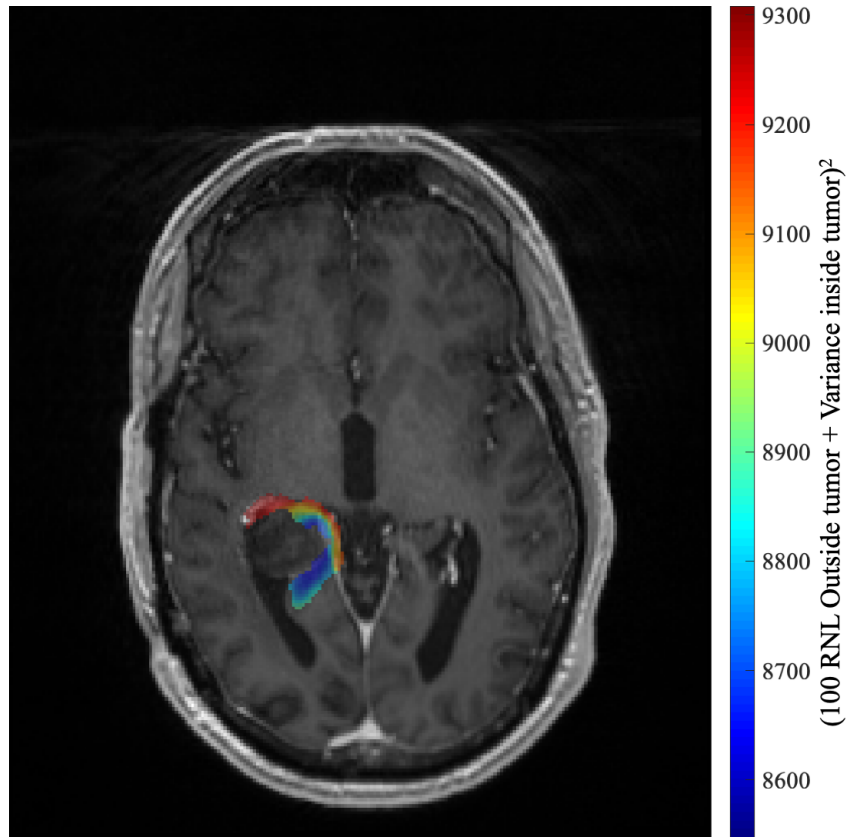


Figure 4.4 Objective function overlain on T_1 + contrast image for Patient 4 on the central tumor slice. The tumor for Patient 4 is highly concave, and located along the rim of a prior tumor resection cavity near the left ventricle. As the majority of the tumor is directly adjacent to a cavity, a global minimum is difficult to distinguish by eye. Multiple catheter sites within the map, highlighted in blue (objective less than 8700) may be run in a forward simulation to aid the surgeon in determining the true optimal placement.

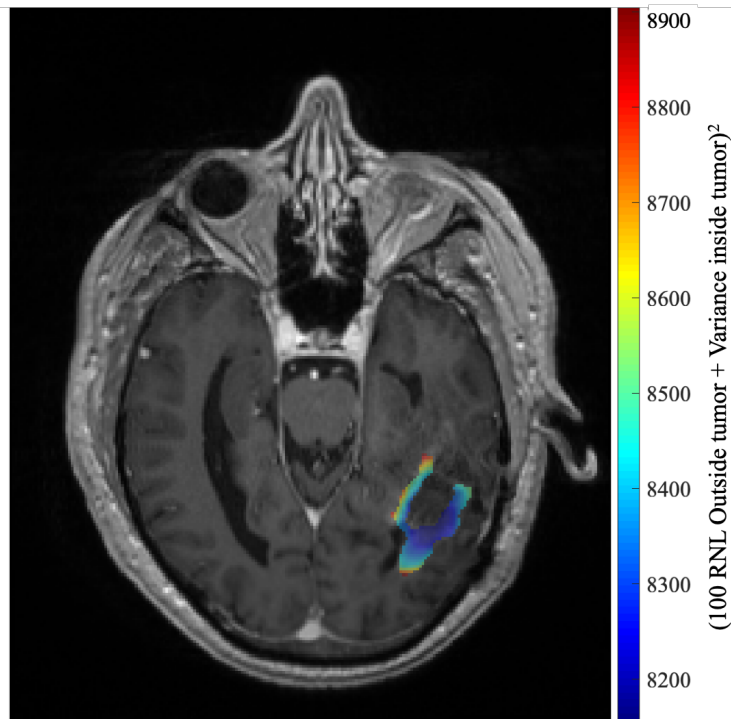


Figure 4.5 Objective function overlay on T_1 + contrast image for Patient 5 on the central tumor slice. The tumor in Patient 5 is highly asymmetrical, and as such has a highly asymmetrical objective function. Despite this asymmetry, there is a clear global minimum, aiding the physician in determining the optimal placement which minimizes leakage in a tumor with complex geometry.

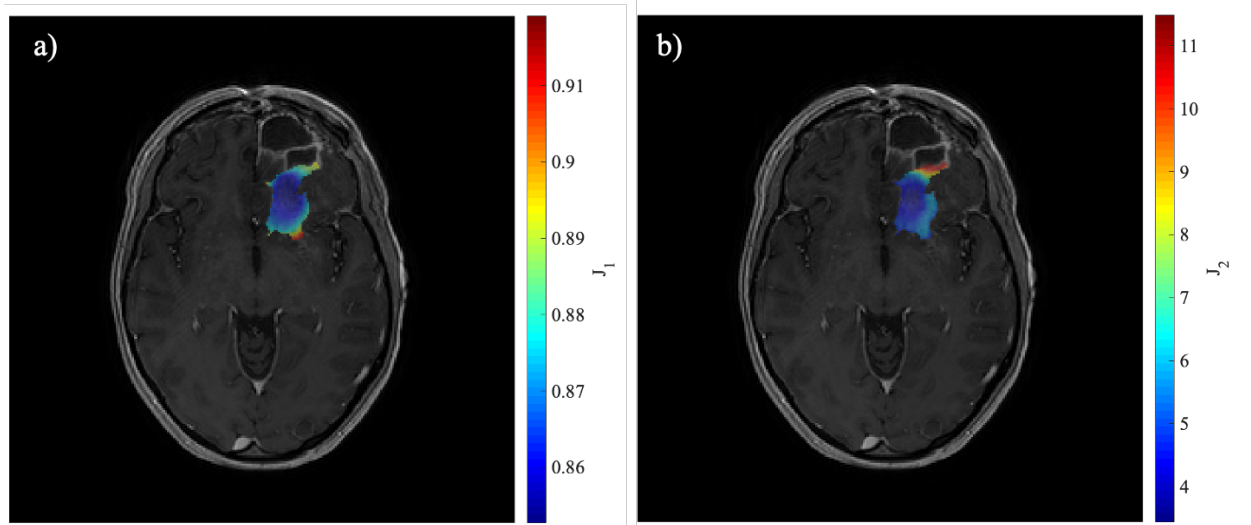


Figure 4.6 Maps of individual components of objective function J . Figure 4.6a depicts a map of J_1 , the normalized ratio of RNL outside of the tumor, over the segmented tumor overlain on a T_1 +contrast image of Patient 3. Figure 4.6b depicts a map of J_2 , the variance of $[RNL]$ within the tumor, over the segmented tumor overlain on a T_1 +contrast image of Patient 3. As the tumor is largely convex, the maps of J_1 and J_2 have a similar shape. Both J_1 and J_2 are maximized nearest to the resection cavity, and minimized near the tumor center of mass.

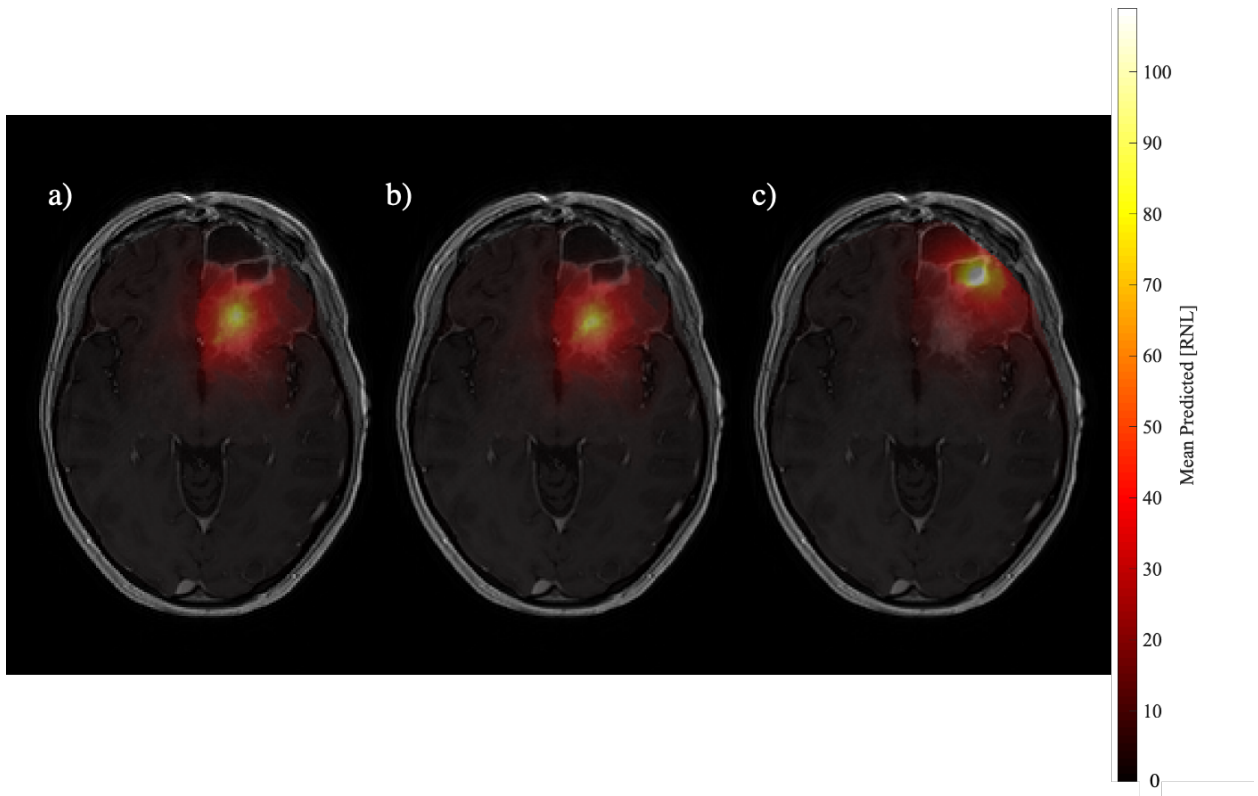


Figure 4.7 Distributions of RNL in Patient 3, resulting from the mean distribution of 100 Monte Carlo predictions, with (4.7a) catheter placement minimizing the objective function $J(x,y)$, (4.7b) placement at tumor center-of-mass, (4.7c) and placement maximizing the objective function $J(x,y)$.

Table 4.1: Comparison of the objective function components and objective function

		Patient					
		1	2	3	4	5	
RNL outside tumor (J_1)	Best	4556	32255	88314	8055	8256	
	Worst	4646	34166	95190	8496	8636	
	COM	4565	32273	88478	8135	8275	Mean
	Worst/Best	1.020	1.059	1.078	1.055	1.046	1.052
	COM/Best	1.002	1.001	1.002	1.010	1.002	1.003
Variance within tumor (J_2)	Best	0.464	4.703	3.441	0.413	0.389	
	Worst	1.291	8.728	11.491	2.086	1.056	
	COM	1.088	4.890	3.651	1.088	0.497	Mean
	Worst/Best	2.782	1.856	3.340	5.049	2.715	3.148
	COM/Best	2.343	1.040	1.061	2.633	1.278	1.671
Objective Function (J)	Best	9070	8073	7889	8547	8156	
	Worst	9314	9604	10129	9308	8905	
	COM	9112	8095	7936	8640	8166	Mean
	Worst/Best	1.0270	1.190	1.284	1.089	1.092	1.136
	COM/Best	1.004	1.003	1.006	1.011	1.001	1.005

Objective-minimizing catheter placement (Best), Objective-maximizing placement (Worst), and tumor center-of-mass placement (COM). Objective function = $\{100(\text{fraction of RNL outside of tumor}) + (\text{Variance within tumor})\}^2$

Chapter 5: Conclusion

5.1 Summary

The overall goal of this dissertation was to apply computational fluid dynamics models to the field of medical imaging to improve the quantitative characterization of cancer. In Aim 1 (Chapter 2), the goal was to investigate the effect of contrast agent diffusion within the extravascular extracellular space on the accuracy of DCE-MRI analysis. We demonstrated that when in the permeability limited regime, the extended Kety-Tofts model under-estimates K^{trans} and v_e , and overestimates v_p . These results highlight the need for improved models of contrast agent transport data acquired from time resolved DCE-MRI data to accurately characterize the blood perfusion properties of the tissue. In Aim 2 (Chapter 3), the goal was to develop a computational fluid dynamics approach, utilizing patient specific imaging and modern finite element methods, to predict the distribution of radiolabeled nanoparticles within brain tumors. After calibrations, the model was capable of recapitulating SPECT data in two-dimensions, and able to provide a confidence-bounded prediction of the final liposome distribution. In Aim 3 (Chapter 4), we utilized the model developed and validated in Aim II to predict the optimal catheter placement for delivery. From our results, we are able to not only predict the locations which minimize leakage into the tumor, but also maximize tumor coverage and prevent excessive leakage outside the tumor.

5.2 Future directions

5.2.1 Models of DCE-MRI data

The results from Aim I (Chapter II) indicate a need for a more accurate parameterization and physical description of the fluid dynamics involved in DCE-MRI. To more accurately parameterize the tissue, we propose utilizing a simple advection-diffusion modeling framework, utilizing ADC information to initialize material property priors, so that DCE-MRI data may be the main source of information on blood perfusion, interstitial velocity, and the presence of local source terms (vasculature). One of the original

advantages of the Kety-Tofts model was that it could be efficiently applied to each individual voxel, or the mean signal intensity curve of a whole region of interest. A large concern in the original implementation of the Kety-Tofts model in the 1990's was that applying the method to an entire 4D DCE-MRI dataset would be too memory- and processing- intensive. Computational power and efficiency have grown exponentially since then, and it is now feasible to invert 4D datasets to determine individual voxel contributions to flow between voxels, as well as the individual source terms within voxels. We hypothesize that a methodology for inverting the advection-diffusion equation for DCE-MRI data (solving for the unknown fields of interstitial velocity, diffusion, and source term), further informed by the ADC, would more accurately reflect the fluid dynamics, increase the predictivity of tumor response models based on the extended Kety-Tofts model, and will allow for the development of more granular, patient-specific models of tumor growth, drug delivery, and treatment response. We propose to develop a completely new parameterization of DCE-MRI, which solves for a local interstitial velocity, and source term, using the method of adjoint states to efficiently perform the inversion of the advection-diffusion-equation. After this data analysis, we would compare these parameters to the extended Kety-Tofts parameters to determine if they carry the same predictive capacity for treatment response and tumor aggression.

5.2.2 Modeling RNL-186 for CED

The model developed in Aim II, while accurate, is only a two-dimensional model, and leaves out much of the spatial information acquired. Thus, the model needs to be expanded to account for all three spatial dimensions. To achieve that goal, the model must be re-written in a compiled language (so that inversion may be achieved in a reasonable amount of time), and expanded to incorporate the full three-dimensional MRI acquisition. Further, the patient cohort used to calibrate the model consisted of only five patients. To have more confidence in the model and its validation, we would retrospectively calibrate a newly developed 3D model for each patient which has entered into the RNL trial, and repeat the leave-one-out validation to ensure the model performance is preserved.

Additionally, as the RNL clinical trial has begun utilizing multiple catheters do further increase coverage of RNL, we would like to extend the model to allow for the placement of multiple catheters to continue to aggregate patients from this study into our parameter distributions. Finally, while SPECT is useful data for calibrating the model *in vivo* with clinical data, in the future we would co-encapsulate an MR contrast agent along with the Rhenium-186 in the nanoliposomes, so that the concentration of the contrast agent may be calibrated and validated against higher resolution (in both time and space) imaging modality. This methodology could be used to minimize gamma-ray exposure from X-ray CT imaging, assuming MR-compatible catheters are available and compatible with the syringe pumps in use for the current clinical trial.

5.2.3 Optimizing CED catheter placement

In Aim 3, we demonstrate a framework for optimal catheter placement, and demonstrate the results of one such instantiation of that framework. To fully characterize the optimization protocol, the model must be thoroughly validated in a larger patient cohort (see 5.2.2), and then applied on a larger dataset to fully investigate. We propose running the optimization algorithm on a large cohort of patients from a GBM dataset taken from the open source Cancer Imaging Archive (wiki.cancerimagingarchive.net), to fully investigate, test, and optimize the catheter placement algorithm. Utilizing a large dataset would allow for a stronger analysis of the total statistical power and study of the clinical utility of our algorithm and framework. Additionally, we would like to expand the optimization algorithm to incorporate the optimization of multiple catheter placements, incorporate DTI tractography, and optimize syringe pump pressure live in the operating room, utilizing the SPECT data acquired during the procedure, a more robust inversion methodology, and the theory of optimal control.

References

- [1] A. G. Waks and E. P. Winer, “Breast Cancer Treatment,” *JAMA*, vol. 321, no. 3, p. 288, Jan. 2019, doi: 10.1001/jama.2018.19323.
- [2] R. E. Hendrick, “Radiation Doses and Cancer Risks from Breast Imaging Studies,” *Radiology*, vol. 257, no. 1, pp. 246–253, Oct. 2010, doi: 10.1148/radiol.10100570.
- [3] B. A. Miller, E. J. Feuer, and B. F. Hankey, “Recent incidence trends for breast cancer in women and the relevance of early detection: an update,” *CA. Cancer J. Clin.*, vol. 43, no. 1, pp. 27–41, Jan. 1993, doi: 10.3322/canjclin.43.1.27.
- [4] T. T. Yankeelov and J. J. Gore, “Dynamic Contrast Enhanced Magnetic Resonance Imaging in Oncology: Theory, Data Acquisition, Analysis, and Examples,” *Curr. Med. Imaging Rev.*, vol. 3, no. 2, pp. 91–107, May 2007, doi: 10.2174/157340507780619179.
- [5] S. L. Barnes, J. G. Whisenant, M. E. Loveless, and T. E. Yankeelov, “Practical Dynamic Contrast Enhanced MRI in Small Animal Models of Cancer: Data Acquisition, Data Analysis, and Interpretation,” *Pharmaceutics*, vol. 4, pp. 442–478, 2012, doi: 10.3390/pharmaceutics4030442.
- [6] M. E. Loveless et al., “A Quantitative Comparison of the Influence of Individual Versus Population-Derived Vascular Input Functions on Dynamic Contrast Enhanced-MRI in Small Animals,” *Magn. Reson. Med.*, vol. 67, pp. 226–236, 2012, doi: 10.1002/mrm.22988.
- [7] P. S. Tofts et al., “Estimating Kinetic Parameters From Dynamic Contrast-Enhanced T1-Weighted MRI of a Diffusible Tracer: Standardized Quantities and Symbols,” *J. Magn. Reson. Imaging*, vol. 10, pp. 223–232, 1999, doi: 10.1002/(SICI)1522-2586(199909)10.
- [8] S. L. Barnes, C. C. Quarles, and T. E. Yankeelov, “Modeling the effect of intra-voxel diffusion of contrast agent on the quantitative analysis of dynamic contrast enhanced magnetic resonance imaging,” *PLoS One*, vol. 9, no. 10, p. e108726, 2014, doi: 10.1371/journal.pone.0108726.
- [9] F. Khalifa et al., “Models and methods for analyzing DCE-MRI: A review,” *Med. Phys.*, vol. 41, no. 12, p. 124301, 2014, doi: 10.1118/1.4898202.
- [10] J. U. Fluckiger, M. E. Loveless, S. L. Barnes, M. Lepage, and T. E. Yankeelov, “A diffusion-compensated model for the analysis of DCE-MRI data: theory,

- simulations and experimental results,” *Phys. Med. Biol.*, vol. 58, pp. 1983–1998, 2013, doi: 10.1088/0031-9155/58/6/1983.
- [11] N. A. Oberheim Bush, S. L. Hervey-Jumper, and M. S. Berger, “Management of Glioblastoma, Present and Future,” *World Neurosurg.*, vol. 131, pp. 328–338, 2019, doi: 10.1016/j.wneu.2019.07.044.
- [12] M. E. Davis, “Glioblastoma: Overview of Disease and Treatment,” *Clin. J. Oncol. Nurs.*, vol. 20, no. 5, pp. S2–S8, Oct. 2016, doi: 10.1188/16.CJON.S1.2-8.
- [13] “Survival in glioblastoma : a review on the impact of treatment modalities,” pp. 1062–1071, 2016, doi: 10.1007/s12094-016-1497-x.
- [14] R. Stupp et al., “Radiotherapy plus Concomitant and Adjuvant Temozolomide for Glioblastoma,” *N. Engl. J. Med.*, vol. 352, no. 10, pp. 987–996, Mar. 2005, doi: 10.1056/NEJMoa043330.
- [15] E. S. S. Newlands, M. F. G. F. G. Stevens, S. R. R. Wedge, R. T. T. Wheelhouse, and C. Brock, “Temozolomide: a review of its discovery, chemical properties, pre-clinical development and clinical trials,” *Cancer Treat. Rev.*, vol. 23, no. 1, pp. 35–61, Jan. 1997, doi: 10.1016/S0305-7372(97)90019-0.
- [16] A. M. Mehta, A. M. Sonabend, and J. N. Bruce, “Convection-Enhanced Delivery,” *Neurotherapeutics*, vol. 14, no. 2, pp. 358–371, 2017, doi: 10.1007/s13311-017-0520-4.
- [17] L. J. O’Donnell and C.-F. Westin, “An Introduction to Diffusion Tensor Image Analysis,” *Neurosurg. Clin. N. Am.*, vol. 22, no. 2, pp. 185–196, Apr. 2011, doi: 10.1016/j.nec.2010.12.004.
- [18] A. . Anderson, J. Xie, J. Pizzonia, R. . Bronen, D. . Spencer, and J. . Gore, “Effects of cell volume fraction changes on apparent diffusion in human cells,” *Magn. Reson. Imaging*, vol. 18, no. 6, pp. 689–695, Jul. 2000, doi: 10.1016/S0730-725X(00)00147-8.
- [19] S. L. Barnes, A. G. Sorace, M. E. Loveless, J. G. Whisenant, and T. E. Yankeelov, “Correlation of tumor characteristics derived from DCE-MRI and DW-MRI with histology in murine models of breast cancer,” *NMR Biomed.*, vol. 28, no. 10, pp. 1345–1356, Oct. 2015, doi: 10.1002/nbm.3377.

- [20] W. Zhan, F. Rodriguez y Baena, and D. Dini, “Effect of tissue permeability and drug diffusion anisotropy on convection-enhanced delivery,” *Drug Deliv.*, vol. 26, no. 1, pp. 773–781, Jan. 2019, doi: 10.1080/10717544.2019.1639844.
- [21] D. S. Tuch, V. J. Wedeen, A. M. Dale, J. S. George, and J. W. Belliveau, “Conductivity tensor mapping of the human brain using diffusion tensor MRI,” *Proc. Natl. Acad. Sci.*, vol. 98, no. 20, pp. 11697–11701, Sep. 2001, doi: 10.1073/pnas.171473898.
- [22] W. T. Phillips et al., “Rhenium-186 liposomes as convection-enhanced nanoparticle brachytherapy for treatment of glioblastoma,” *Neuro. Oncol.*, vol. 14, no. 4, pp. 416–425, Apr. 2012, doi: 10.1093/neuonc/nos060.
- [23] M. Tavakoli, M. Naji, A. Abdollahi, and F. Kalantari, “Attenuation correction in SPECT images using attenuation map estimation with its emission data,” *Mar.* 2017, p. 101324Z, doi: 10.1117/12.2254828.
- [24] F. J. Beekman, C. Kamphuis, and E. C. Frey, “Scatter compensation methods in 3D iterative SPECT reconstruction: A simulation study,” *Phys. Med. Biol.*, vol. 42, no. 8, pp. 1619–1632, Aug. 1997, doi: 10.1088/0031-9155/42/8/011.
- [25] A. K. Buck et al., “SPECT/CT,” *J. Nucl. Med.*, vol. 49, no. 8, pp. 1305–1319, Jul. 2008, doi: 10.2967/jnumed.107.050195.
- [26] R. Raghavan, S. Mikaelian, M. Brady, and Z. J. Chen, “Fluid infusions from catheters into elastic tissue: I. Azimuthally symmetric backflow in homogeneous media,” *Phys. Med. Biol.*, vol. 55, no. 1, pp. 281–304, 2010, doi: 10.1088/0031-9155/55/1/017.
- [27] K. H. Rosenbluth, J. F. Eschermann, G. Mittermeyer, R. Thomson, S. Mittermeyer, and K. S. Bankiewicz, “Analysis of a simulation algorithm for direct brain drug delivery,” *Neuroimage*, vol. 59, no. 3, pp. 2423–2429, 2012, doi: 10.1016/j.neuroimage.2011.08.107.
- [28] A. Jahangiri, A. T. Chin, P. M. Flanigan, and R. Chen, “Convection-enhanced delivery in glioblastoma: a review of preclinical and clinical studies,” vol. 126, no. 1, pp. 191–200, 2017, doi: 10.3171/2016.1.JNS151591.Convection-enhanced.
- [29] K. N. Magdoom, G. L. Pishko, and J. H. Kim, “Evaluation of a Voxelized Model Based on DCE-MRI for Tracer Transport in Tumor,” vol. 134, no. September 2012, pp. 1–9, 2016, doi: 10.1115/1.4007096.

- [30] C. A. Stine and J. M. Munson, “Convection-Enhanced Delivery: Connection to and Impact of Interstitial Fluid Flow,” *Front. Oncol.*, vol. 9, no. October, 2019, doi: 10.3389/fonc.2019.00966.
- [31] F. Danhier, O. Feron, and V. Pr at, “To exploit the tumor microenvironment: Passive and active tumor targeting of nanocarriers for anti-cancer drug delivery.,” *J. Control. Release*, vol. 148, no. 2, pp. 135–46, Dec. 2010, doi: 10.1016/j.jconrel.2010.08.027.
- [32] L. Brannon-Peppas and J. O. Blanchette, “Nanoparticle and targeted systems for cancer therapy,” *Adv. Drug Deliv. Rev.*, vol. 64, pp. 206–212, Dec. 2012, doi: 10.1016/j.addr.2012.09.033.
- [33] S. Stapleton et al., “A mathematical model of the enhanced permeability and retention effect for liposome transport in solid tumors,” *PLoS One*, vol. 8, no. 12, pp. 1–10, 2013, doi: 10.1371/journal.pone.0081157.
- [34] S. X. Wang et al., “Intraoperative ¹⁸⁶re-liposome radionuclidetherapy in a head and neck squamous cell carcinoma xenograft positive surgical margin model,” *Clin. Cancer Res.*, vol. 14, no. 12, pp. 3975–3983, 2008, doi: 10.1158/1078-0432.CCR-07-4149.
- [35] M. Argyrou, A. Valassi, M. Andreou, and M. Lyra, “Dosimetry and Therapeutic Ratios for Rhenium-186 HEDP,” *ISRN Mol. Imaging*, vol. 2013, pp. 1–6, 2013, doi: 10.1155/2013/124603.
- [36] J. Woo et al., “Subject-specific brain tumor growth modelling via an efficient Bayesian inference framework,” *Med. Imaging 2018 Image Process.*, vol. 10574, no. March, p. 89, 2018, doi: 10.1117/12.2293145.
- [37] J. Floyd, W. Phillips, B. Goins, A. Bao, and A. Brenner, “FIRST IN HUMAN STUDY OF RHENIUM NANOLIPOSOMES FOR INTRATUMORAL THERAPY OF GLIOMA,” doi: 10.1093/neuonc/nov205.3.
- [38] L. T. Baxter and R. K. Jain, “Transport of fluid and macromolecules in tumors. I. Role of interstitial pressure and convection,” *Microvasc. Res.*, vol. 37, no. 1, pp. 77–104, 1989, doi: 10.1016/0026-2862(89)90074-5.
- [39] H. Liu, P. R. Patil, and U. Narusawa, “On Darcy-Brinkman equation: Viscous flow between two parallel plates packed with regular square arrays of cylinders,” *Entropy*, vol. 9, no. 3, pp. 118–131, 2007, doi: 10.3390/e9030118.

- [40] I. Harari and T. J. R. Hughes, “Stabilized finite element methods for steady advection-diffusion with production,” *Comput. Methods Appl. Mech. Eng.*, vol. 115, no. C, pp. 165–191, 1994, doi: 10.1016/0045-7825(94)90193-7.
- [41] R. K. Jain, “Transport of Molecules in the Tumor Interstitium : A Review1,” vol. 500, no. 17, pp. 3039–3052, 1987.
- [42] X. Li et al., “Combined DCE-MRI and DW-MRI for Predicting Breast Cancer Pathological Response After the First Cycle of Neoadjuvant Chemotherapy,” *Invest Radiol*, vol. 50, no. 4, pp. 195–204, 2015, doi: 10.1097/RLI.000000000000100.Combined.
- [43] A. Surov et al., “Correlations Between DCE MRI and Histopathological Parameters in Head and Neck Squamous Cell Carcinoma,” *Transl. Oncol.*, vol. 10, no. 1, pp. 17–21, 2017, doi: 10.1016/j.tranon.2016.10.001.
- [44] D. A. Hormuth et al., “A mechanically coupled reaction–diffusion model that incorporates intra-tumoural heterogeneity to predict in vivo glioma growth,” *J. R. Soc. Interface*, vol. 14, no. 128, 2017, doi: 10.1098/rsif.2016.1010.
- [45] A. M. Jarrett, D. A. Hormuth, S. L. Barnes, X. Feng, W. Huang, and T. E. Yankeelov, “Incorporating drug delivery into an imaging-driven, mechanics-coupled reaction diffusion model for predicting the response of breast cancer to neoadjuvant chemotherapy: theory and preliminary clinical results,” *Phys. Med. Biol.*, vol. 63, no. 10, p. 105015, May 2018, doi: 10.1088/1361-6560/aac040.
- [46] T. E. Yankeelov et al., “Clinically relevant modeling of tumor growth and treatment response.,” *Sci. Transl. Med.*, vol. 5, no. 187, p. 187ps9, 2013, doi: 10.1126/scitranslmed.3005686.
- [47] E. A. B. F. Lima, J. T. Oden, D. A. Hormuth, T. E. Yankeelov, and R. C. Almeida, “Selection, calibration, and validation of models of tumor growth,” *Math. Model. Methods Appl. Sci.*, vol. 26, no. 12, pp. 2341–2368, 2016, doi: 10.1142/S021820251650055X.
- [48] D. A. I. Hormuth et al., “Predicting in vivo glioma growth with the reaction diffusion equation constrained by quantitative magnetic resonance imaging data,” *Phys. Biol.*, vol. 12, p. 046006, 2015, doi: 10.1088/1478-3975/12/4/046006.
- [49] W. Zhan, D. Y. Arifin, T. K. Lee, and C. H. Wang, “Mathematical Modelling of Convection Enhanced Delivery of Carmustine and Paclitaxel for Brain Tumour Therapy,” *Pharm. Res.*, vol. 34, no. 4, pp. 860–873, 2017, doi: 10.1007/s11095-017-2114-6.

- [50] A. A. Linninger, M. R. Somayaji, M. Mekarski, and L. Zhang, “Prediction of convection-enhanced drug delivery to the human brain,” *J. Theor. Biol.*, vol. 250, no. 1, pp. 125–138, 2008, doi: 10.1016/j.jtbi.2007.09.009.
- [51] T. J. R. Hughes, L. P. Franca, and M. Mallet, “A new finite element formulation for computational fluid dynamics: VI. Convergence analysis of the generalized SUPG formulation for linear time-dependent multidimensional advective-diffusive systems,” *Comput. Methods Appl. Mech. Eng.*, vol. 63, no. 1, pp. 97–112, 1987, doi: 10.1016/0045-7825(87)90125-3.
- [52] M. S. Branicky, V. S. Borkar, and S. K. Mitter, “A unified framework for hybrid control: model and optimal control theory,” *IEEE Trans. Automat. Contr.*, vol. 43, no. 1, pp. 31–45, 1998, doi: 10.1109/9.654885.
- [53] B. A. Moffat et al., “Diffusion imaging for evaluation of tumor therapies in preclinical animal models,” *Magn. Reson. Mater. Physics, Biol. Med.*, vol. 17, no. 3–6, pp. 249–259, Dec. 2004, doi: 10.1007/s10334-004-0079-z.
- [54] T. T. Yankeelov and J. J. Gore, “Dynamic Contrast Enhanced Magnetic Resonance Imaging in Oncology: Theory, Data Acquisition, Analysis, and Examples,” *Curr. Med. Imaging Rev.*, vol. 3, no. 2, pp. 91–107, May 2007, doi: 10.2174/157340507780619179.
- [55] A. Surov et al., “Correlations Between DCE MRI and Histopathological Parameters in Head and Neck Squamous Cell Carcinoma,” *Transl. Oncol.*, vol. 10, no. 1, pp. 17–21, 2017, doi: 10.1016/j.tranon.2016.10.001.
- [56] G. Jia et al., “Colorectal Liver Metastases: Contrast Agent Diffusion Coefficient for Quantification of Contrast Enhancement Heterogeneity at MR Imaging,” *Radiology*, vol. 248, no. 3, pp. 901–9, 2008.
- [57] H. Daldrup et al., “Correlation of Dynamic Contrast Enhanced MR Imaging with Histologic Tumor Grade: Comparison of Macromolecular and Small-Molecular Contrast Media,” *AJR. Am. J. Roentgenol.*, vol. 171, no. 4, pp. 941–949, 1998.
- [58] M. Haris et al., “Differentiation of infective from neoplastic brain lesions by dynamic contrast-enhanced MRI,” *Neuroradiology*, vol. 50, pp. 531–540, 2008, doi: 10.1007/s00234-008-0378-6.
- [59] X. Li et al., “Combined DCE-MRI and DW-MRI for Predicting Breast Cancer Pathological Response After the First Cycle of Neoadjuvant Chemotherapy,” *Invest Radiol*, vol. 50, no. 4, pp. 195–204, 2015, doi: 10.1097/RLI.000000000000100.Combined.

- [60] X. Li et al., “Analyzing Spatial Heterogeneity in DCE- and DW-MRI Parametric Maps to Optimize Prediction of Pathologic Response to Neoadjuvant Chemotherapy,” *Transl. Oncol.*, vol. 7, no. 1, pp. 14–22, 2014, doi: 10.1593/tlo.13748.
- [61] J. Gaustad, V. Pozdniakova, T. Hompland, T. G. Simonsen, and E. K. Rofstad, “Magnetic resonance imaging identifies early effects of sunitinib treatment in human melanoma xenografts,” *J. Exp. Clin. Cancer Res.*, vol. 32, no. 93, 2013.
- [62] J. G. Whisenant et al., “Evaluating treatment response using DW-MRI and DCE-MRI in trastuzumab responsive and resistant HER2-overexpressing human breast cancer xenografts,” *Transl. Oncol.*, vol. 7, no. 6, pp. 768–779, 2014, doi: 10.1016/j.tranon.2014.09.011.
- [63] R. G. Abramson et al., “MRI Biomarkers in Oncology Clinical Trials,” *Magn Reson Imaging Clin N Am*, vol. 24, no. 1, pp. 11–29, 2016, doi: 10.1016/j.mric.2015.08.002.MRI.
- [64] T. E. Yankeelov, L. R. Arlinghaus, X. Li, and J. C. Gore, “The Role of Magnetic Resonance Imaging Biomarkers in Clinical,” *Semin. Oncol.*, vol. 38, no. 1, pp. 16–25, 2011, doi: 10.1053/j.seminoncol.2010.11.007.
- [65] S. Walker-Samuel, M. O. Leach, and D. J. Collins, “Evaluation of response to treatment using DCE-MRI: the relationship between initial area under the gadolinium curve (IAUGC) and quantitative pharmacokinetic analysis,” *Phys. Med. Biol.*, vol. 51, pp. 3593–3602, 2006, doi: 10.1088/0031-9155/51/14/021.
- [66] M. Asselin, J. P. B. O’Connor, R. Boellaard, N. A. Thacker, and A. Jackson, “Quantifying heterogeneity in human tumours using MRI and PET,” *Eur. J. Cancer*, vol. 48, pp. 447–455, 2012, doi: 10.1016/j.ejca.2011.12.025.
- [67] P. S. Tofts and A. G. Kermode, “Measurement of the blood-brain barrier permeability and leakage space using dynamic MR imaging. 1. Fundamental concepts,” *Magn. Reson. Med.*, vol. 17, pp. 357–367, 1991, doi: 10.1002/mrm.1910170208.
- [68] M. Pellerin, T. E. Yankeelov, and M. Lepage, “Incorporating Contrast Agent Diffusion Into the Analysis of DCE-MRI Data,” *Magn. Reson. Med.*, vol. 58, pp. 1124–1134, 2007, doi: 10.1002/mrm.21400.
- [69] N. A. Pannetier, C. Debacker, F. Mauconduit, T. Christen, and E. L. Barbier, “A Simulation Tool for Dynamic Contrast Enhanced MRI,” *PLoS One*, vol. 8, no. 3, 2013, doi: 10.1371/journal.pone.0057636.

- [70] J. U. Fluckiger, M. E. Loveless, S. L. Barnes, M. Lepage, and T. E. Yankeelov, "A diffusion-compensated model for the analysis of DCE-MRI data: theory, simulations and experimental results," *Phys. Med. Biol.*, vol. 58, pp. 1983–1998, 2013, doi: 10.1088/0031-9155/58/6/1983.
- [71] S. Sourbron, "A Tracer-Kinetic Field Theory for Medical Imaging," *IEEE Trans. Med. Imaging*, vol. 33, no. 4, pp. 935–946, 2014.
- [72] S. S. Kety, "The Theory And Applications of The Exchange of Inert Gas at the Lungs and Tissues," *Pharmacol. Rev.*, vol. 3, no. 1, pp. 1–41, 1951, [Online]. Available: <http://pharmrev.aspetjournals.org/content/3/1/1.long>.
- [73] T. S. Koh, S. Hartono, C. H. Thng, T. K. H. Lim, L. Martarello, and Q. S. Ng, "In Vivo Measurement of Gadolinium Diffusivity by Dynamic Contrast-Enhanced MRI : A Preclinical Study of Human Xenografts," *Magn. Reson. Med.*, vol. 69, pp. 269–276, 2013, doi: 10.1002/mrm.24246.
- [74] M. J. Gordon, K. C. Chu, A. Margaritis, A. J. Martin, C. R. Ethier, and B. K. Rutt, "Measurement of Gd-DTPA Diffusion Through PVA Hydrogel Using a Novel Magnetic Resonance Imaging Method," *Biotechnol. Bioeng.*, vol. 65, no. 4, pp. 459–467, 1999.
- [75] T. Langø, T. Mørland, and A. O. Brubakk, "Diffusion coefficients and solubility coefficients for gases in biological fluids and tissues: a review," *Undersea Hyperb. Med.*, vol. 23, no. 4, pp. 247–272, 1996, [Online]. Available: <https://medspace.mc.duke.edu/sites/default/files/8989856.pdf>.
- [76] B. T. Saam et al., "MR Imaging of Diffusion of ^3He Gas in Healthy and Diseased Lungs," *Magn. Reson. Med.*, vol. 44, pp. 174–179, 2000.
- [77] S. L. Barnes, C. C. Quarles, and T. E. Yankeelov, "Modeling the effect of intra-voxel diffusion of contrast agent on the quantitative analysis of dynamic contrast enhanced magnetic resonance imaging," *PLoS One*, vol. 9, no. 10, p. e108726, 2014, doi: 10.1371/journal.pone.0108726.
- [78] A. G. Sorace et al., "Trastuzumab improves tumor perfusion and vascular delivery of cytotoxic therapy in a murine model of HER2+ breast cancer: preliminary results," *Breast Cancer Res. Treat.*, vol. 155, no. 2, pp. 273–284, Jan. 2016, doi: 10.1007/s10549-016-3680-8.
- [79] P. S. Tofts et al., "Estimating Kinetic Parameters From Dynamic Contrast-Enhanced T1-Weighted MRI of a Diffusible Tracer: Standardized Quantities and

- Symbols,” *J. Magn. Reson. Imaging*, vol. 10, pp. 223–232, 1999, doi: 10.1002/(SICI)1522-2586(199909)10.
- [80] Q. G. De Lussanet et al., “Dynamic contrast-enhanced magnetic resonance imaging at 1.5 Tesla with gadopentetate dimeglumine to assess the angiostatic effects of anginex in mice,” *Eur. J. Cancer*, vol. 40, pp. 1262–1268, 2004, doi: 10.1016/j.ejca.2004.01.020.
- [81] D. R. Lynch, “Numerical Partial Differential Equations for Environmental Scientists and Engineers: A First Practical Course,” New York: Springer, 2005, p. 128.
- [82] J. Lagrange, *Lecons elementaires sur les mathematiques, donnees à l’ecole normale*. Paris: Gauthier-Villars, 1795.
- [83] M. E. Loveless et al., “A Quantitative Comparison of the Influence of Individual Versus Population-Derived Vascular Input Functions on Dynamic Contrast Enhanced-MRI in Small Animals,” *Magn. Reson. Med.*, vol. 67, pp. 226–236, 2012, doi: 10.1002/mrm.22988.
- [84] S. L. Barnes, J. G. Whisenant, M. E. Loveless, and T. E. Yankeelov, “Practical Dynamic Contrast Enhanced MRI in Small Animal Models of Cancer: Data Acquisition, Data Analysis, and Interpretation,” *Pharmaceutics*, vol. 4, pp. 442–478, 2012, doi: 10.3390/pharmaceutics4030442.
- [85] S. L. Barnes, A. G. Sorace, M. E. Loveless, J. G. Whisenant, and T. E. Yankeelov, “Correlation of tumor characteristics derived from DCE-MRI and DW-MRI with histology in murine models of breast cancer,” *NMR Biomed.*, vol. 28, no. 10, pp. 1345–1356, Oct. 2015, doi: 10.1002/nbm.3377.
- [86] B. Y. J. Crank and P. Nicolson, “A practical method for numerical evaluation of solutions of partial differential equations of the heat-conduction type,” *Adv. Comput. Math.*, vol. 6, pp. 207–226, 1946.
- [87] B. J. Cowling, A. Aiello, H. Kong, and C. Hill, “Glioblastoma in Adults: A Society for Neuro-Oncology (SNO) and European Society of Neuro-Oncology (EANO) Consensus Review on Current Management and Future Directions,” pp. 1–10, 2020.
- [88] G. Tabatabai and H. Wakimoto, “Glioblastoma: State of the art and future perspectives,” *Cancers (Basel)*, vol. 11, no. 8, pp. 10–13, 2019, doi: 10.3390/cancers11081091.

- [89] R. Stupp et al., “Radiotherapy plus Concomitant and Adjuvant Temozolomide for Glioblastoma,” *N. Engl. J. Med.*, vol. 352, no. 10, pp. 987–996, Mar. 2005, doi: 10.1056/NEJMoa043330.
- [90] N. A. Oberheim Bush, S. L. Hervey-Jumper, and M. S. Berger, “Management of Glioblastoma, Present and Future,” *World Neurosurg.*, vol. 131, pp. 328–338, 2019, doi: 10.1016/j.wneu.2019.07.044.
- [91] L. T. Shieh, H. R. Guo, Y. K. Chang, N. M. Lu, and S. Y. Ho, “Clinical implications of multiple glioblastomas: An analysis of prognostic factors and survival to distinguish from their single counterparts,” *J. Formos. Med. Assoc.*, vol. 119, no. 3, pp. 728–734, 2020, doi: 10.1016/j.jfma.2019.08.024.
- [92] A. Jahangiri, A. T. Chin, P. M. Flanigan, R. Chen, K. Bankiewicz, and M. K. Aghi, “Convection-enhanced delivery in glioblastoma: a review of preclinical and clinical studies,” *J. Neurosurg.*, vol. 126, no. 1, pp. 191–200, Jan. 2017, doi: 10.3171/2016.1.JNS151591.
- [93] W. T. Phillips et al., “Rhenium-186 liposomes as convection-enhanced nanoparticle brachytherapy for treatment of glioblastoma,” *Neuro. Oncol.*, vol. 14, no. 4, pp. 416–425, Apr. 2012, doi: 10.1093/neuonc/nos060.
- [94] A. Bao, B. Goins, R. Klipper, G. Negrete, and W. T. Phillips, “¹⁸⁶Re-liposome labeling using ¹⁸⁶Re-SNS/S complexes: In vitro stability, imaging, and biodistribution in rats,” *J. Nucl. Med.*, vol. 44, no. 12, pp. 1992–1999, 2003.
- [95] J. Floyd, W. Phillips, B. Goins, A. Bao, and A. Brenner, “ATNT-03FIRST IN HUMAN STUDY OF RHENIUM NANOLIPOSOMES FOR INTRATUMORAL THERAPY OF GLIOMA,” *Neuro. Oncol.*, vol. 17, no. suppl 5, p. v10.3-v10, 2015, doi: 10.1093/neuonc/nov205.03.
- [96] S. Kunwar et al., “Phase III randomized trial of CED of IL13-PE38QQR vs Gliadel wafers for recurrent glioblastoma,” *Neuro. Oncol.*, vol. 12, no. 8, pp. 871–881, Aug. 2010, doi: 10.1093/neuonc/nop054.
- [97] K. H. Rosenbluth, J. F. Eschermann, G. Mittermeyer, R. Thomson, S. Mittermeyer, and K. S. Bankiewicz, “Analysis of a simulation algorithm for direct brain drug delivery,” *Neuroimage*, vol. 59, no. 3, pp. 2423–2429, 2012, doi: 10.1016/j.neuroimage.2011.08.107.

- [98] A. A. Linninger, M. R. Somayaji, T. Erickson, X. Guo, and R. D. Penn, “Computational methods for predicting drug transport in anisotropic and heterogeneous brain tissue,” vol. 41, pp. 2176–2187, 2008, doi: 10.1016/j.jbiomech.2008.04.025.
- [99] K. H. Støverud, M. Darcis, R. Helmig, and S. M. Hassanizadeh, “Modeling Concentration Distribution and Deformation During Convection-Enhanced Drug Delivery into Brain Tissue,” *Transp. Porous Media*, vol. 92, no. 1, pp. 119–143, 2012, doi: 10.1007/s11242-011-9894-7.
- [100] J. Ashburner and K. J. Friston, *Human Brain Function*. Elsevier, 2004.
- [101] B. M. ELLINGSON et al., “Diffusion MRI quality control and functional diffusion map results in ACRIN 6677/RTOG 0625: A multicenter, randomized, phase II trial of bevacizumab and chemotherapy in recurrent glioblastoma,” *Int. J. Oncol.*, vol. 46, no. 5, pp. 1883–1892, May 2015, doi: 10.3892/ijo.2015.2891.
- [102] J. Woo, M. Stone, and J. L. Prince, “Multimodal Registration via Mutual Information Incorporating Geometric and Spatial Context,” *IEEE Trans. Image Process.*, vol. 24, no. 2, pp. 757–769, Feb. 2015, doi: 10.1109/TIP.2014.2387019.
- [103] S. Y. Chun, J. A. Fessler, and Y. K. Dewaraja, “Correction for Collimator-Detector Response in SPECT Using Point Spread Function Template,” *IEEE Trans. Med. Imaging*, vol. 32, no. 2, pp. 295–305, Feb. 2013, doi: 10.1109/TMI.2012.2225441.
- [104] B. R. Zeeberg, A. N. Bice, S. Loncaric, and H. N. Wagner, “A Theoretically-Correct Algorithm to Compensate for a Three-Dimensional Spatially-Variant Point Spread Function in Spect Imaging,” in *Information Processing in Medical Imaging*, Boston, MA: Springer US, 1988, pp. 245–254.
- [105] L. T. Baxter and R. K. Jain, “Transport of fluid and macromolecules in tumors. I. Role of interstitial pressure and convection,” *Microvasc. Res.*, vol. 37, no. 1, pp. 77–104, 1989, doi: 10.1016/0026-2862(89)90074-5.
- [106] R. K. Jain, “Transport of Molecules in the Tumor Interstitium: A Review,” vol. 500, no. 17, pp. 3039–3052, 1987.
- [107] D. N. Arnold, F. Brezzi, and M. Fortin, “A stable finite element for the stokes equations,” *Calcolo*, vol. 21, no. 4, pp. 337–344, Dec. 1984, doi: 10.1007/BF02576171.

- [108] I. Harari and T. J. R. Hughes, “Stabilized finite element methods for steady advection-diffusion with production,” *Comput. Methods Appl. Mech. Eng.*, vol. 115, no. C, pp. 165–191, 1994, doi: 10.1016/0045-7825(94)90193-7.
- [109] T. J. R. Hughes, L. P. Franca, and M. Mallet, “A new finite element formulation for computational fluid dynamics: VI. Convergence analysis of the generalized SUPG formulation for linear time-dependent multidimensional advective-diffusive systems,” *Comput. Methods Appl. Mech. Eng.*, vol. 63, no. 1, pp. 97–112, 1987, doi: 10.1016/0045-7825(87)90125-3.
- [110] G. N. W. et al. A. Logg, K.-A. Mardal, *Automated Solution of Differential Equations by the Finite Element Method*, vol. 84. Berlin, Heidelberg: Springer Berlin Heidelberg, 2012.
- [111] J. Dongarra et al., “SuperLU,” in *Encyclopedia of Parallel Computing*, Boston, MA: Springer US, 2011, pp. 1955–1962.
- [112] S. U. Ansari, M. Hussain, S. M. Ahmad, A. Rashid, and S. Mazhar, “Stabilized mixed finite element method for transient darcy flow,” *Trans. Can. Soc. Mech. Eng.*, vol. 41, no. 1, pp. 85–97, 2017, doi: 10.1139/tcsme-2017-1006.
- [113] D. A. I. Hormuth et al., “Predicting in vivo glioma growth with the reaction diffusion equation constrained by quantitative magnetic resonance imaging data,” *Phys. Biol.*, vol. 12, p. 046006, 2015, doi: 10.1088/1478-3975/12/4/046006.
- [114] P. Virtanen et al., “SciPy 1.0: fundamental algorithms for scientific computing in Python,” *Nat. Methods*, vol. 17, no. 3, pp. 261–272, Mar. 2020, doi: 10.1038/s41592-019-0686-2.
- [115] H. Akoglu, “User’s guide to correlation coefficients,” *Turkish J. Emerg. Med.*, vol. 18, no. 3, pp. 91–93, 2018, doi: 10.1016/j.tjem.2018.08.001.
- [116] L. R. Dice, “Measures of the Amount of Ecologic Association Between Species,” *Ecology*, vol. 26, no. 3, pp. 297–302, Jul. 1945, doi: 10.2307/1932409.
- [117] K. Yamaoka, T. Nakagawa, and T. Uno, “Application of Akaike’s information criterion (AIC) in the evaluation of linear pharmacokinetic equations,” *J. Pharmacokinet. Biopharm.*, vol. 6, no. 2, pp. 165–175, Apr. 1978, doi: 10.1007/BF01117450.
- [118] D. J. Balding and R. A. Nichols, “A method for quantifying differentiation between populations at multi-allelic loci and its implications for investigating identity and paternity,” *Genetica*, vol. 96, no. 1–2, pp. 3–12, Jun. 1995, doi: 10.1007/BF01441146.

- [119] M. T. Krauze, J. Forsayeth, D. Yin, and K. S. Bankiewicz, “Chapter 18 Convection-Enhanced Delivery of Liposomes to Primate Brain,” 2009, pp. 349–362.
- [120] K. M. Kingsmore et al., “MRI analysis to map interstitial flow in the brain tumor microenvironment,” *APL Bioeng.*, vol. 2, no. 3, p. 031905, 2018, doi: 10.1063/1.5023503.
- [121] C. A. Stine and J. M. Munson, “Convection-Enhanced Delivery: Connection to and Impact of Interstitial Fluid Flow,” *Front. Oncol.*, vol. 9, no. October, 2019, doi: 10.3389/fonc.2019.00966.
- [122] A. A. Linninger, M. R. Somayaji, M. Mekarski, and L. Zhang, “Prediction of convection-enhanced drug delivery to the human brain,” *J. Theor. Biol.*, vol. 250, no. 1, pp. 125–138, 2008, doi: 10.1016/j.jtbi.2007.09.009.
- [123] W. Zhan, D. Y. Arifin, T. K. Lee, and C. H. Wang, “Mathematical Modelling of Convection Enhanced Delivery of Carmustine and Paclitaxel for Brain Tumour Therapy,” *Pharm. Res.*, vol. 34, no. 4, pp. 860–873, 2017, doi: 10.1007/s11095-017-2114-6.
- [124] J. H. Kim, G. W. Astarý, S. Kantorovich, T. H. Mareci, P. R. Carney, and M. Sarntinoranont, “Voxelized computational model for convection-enhanced delivery in the rat ventral hippocampus: Comparison with in vivo MR experimental studies,” *Ann. Biomed. Eng.*, vol. 40, no. 9, pp. 2043–2058, 2012, doi: 10.1007/s10439-012-0566-8.
- [125] A. Jahangiri, A. T. Chin, P. M. Flanigan, R. Chen, K. Bankiewicz, and M. K. Aghi, “Convection-enhanced delivery in glioblastoma: a review of preclinical and clinical studies,” *J. Neurosurg.*, vol. 126, no. 1, pp. 191–200, Jan. 2017, doi: 10.3171/2016.1.JNS151591.
- [126] W. T. Phillips et al., “Rhenium-186 liposomes as convection-enhanced nanoparticle brachytherapy for treatment of glioblastoma,” *Neuro. Oncol.*, vol. 14, no. 4, pp. 416–425, Apr. 2012, doi: 10.1093/neuonc/nos060.
- [127] A. M. Mehta, A. M. Sonabend, and J. N. Bruce, “Convection-Enhanced Delivery,” *Neurotherapeutics*, vol. 14, no. 2, pp. 358–371, 2017, doi: 10.1007/s13311-017-0520-4.

- [128] M. A. Vogelbaum et al., “Clinical utility of a patient-specific algorithm for simulating intracerebral drug infusions,” *Neuro. Oncol.*, vol. 2009, pp. 167–175, 2009, doi: 10.1215/15228517.
- [129] T. Shahar, Z. Ram, and A. A. Kanner, “Convection-enhanced delivery catheter placements for high-grade gliomas: complications and pitfalls,” *J. Neurooncol.*, vol. 107, no. 2, pp. 373–378, Apr. 2012, doi: 10.1007/s11060-011-0751-x.
- [130] R. Raghavan, M. L. Brady, M. I. Rodríguez-Ponce, A. Hartlep, C. Pedain, and J. H. Sampson, “Convection-enhanced delivery of therapeutics for brain disease, and its optimization,” *Neurosurg. Focus*, vol. 20, no. 4, p. E12, Apr. 2006, doi: 10.3171/foc.2006.20.4.7.
- [131] J. Floyd, W. Phillips, B. Goins, A. Bao, and A. Brenner, “ATNT-03FIRST IN HUMAN STUDY OF RHENIUM NANOLIPOSOMES FOR INTRATUMORAL THERAPY OF GLIOMA,” *Neuro. Oncol.*, vol. 17, no. suppl 5, p. v10.3-v10, 2015, doi: 10.1093/neuonc/nov205.03.
- [132] B. Sengupta, K. J. Friston, and W. D. Penny, “Efficient gradient computation for dynamical models,” *Neuroimage*, vol. 98, pp. 521–527, 2014, doi: 10.1016/j.neuroimage.2014.04.040.
- [133] D. A. Hormuth, J. A. Weis, S. L. Barnes, M. I. Miga, V. Quaranta, and T. E. Yankeelov, “Biophysical Modeling of In Vivo Glioma Response After Whole-Brain Radiation Therapy in a Murine Model of Brain Cancer,” *Int. J. Radiat. Oncol.*, vol. 100, no. 5, pp. 1270–1279, Apr. 2018, doi: 10.1016/j.ijrobp.2017.12.004.
- [134] E. A. B. F. Lima et al., “Selection and validation of predictive models of radiation effects on tumor growth based on noninvasive imaging data,” *Comput. Methods Appl. Mech. Eng.*, vol. 327, pp. 277–305, Dec. 2017, doi: 10.1016/j.cma.2017.08.009.
- [135] T. Mizutani et al., “Optimization of treatment strategy by using a machine learning model to predict survival time of patients with malignant glioma after radiotherapy,” *J. Radiat. Res.*, vol. 60, no. 6, pp. 818–824, Nov. 2019, doi: 10.1093/jrr/rrz066.
- [136] T. Li and L. Xing, “Optimizing 4D cone-beam CT acquisition protocol for external beam radiotherapy,” *Int. J. Radiat. Oncol.*, vol. 67, no. 4, pp. 1211–1219, Mar. 2007, doi: 10.1016/j.ijrobp.2006.10.024.

- [137] S. Liu et al., “Optimizing efficiency and safety in external beam radiotherapy using automated plan check (APC) tool and six sigma methodology,” *J. Appl. Clin. Med. Phys.*, vol. 20, no. 8, pp. 56–64, Aug. 2019, doi: 10.1002/acm2.12678.
- [138] K. H. Rosenbluth, J. F. Eschermann, G. Mittermeyer, R. Thomson, S. Mittermeyer, and K. S. Bankiewicz, “Analysis of a simulation algorithm for direct brain drug delivery,” *Neuroimage*, vol. 59, no. 3, pp. 2423–2429, 2012, doi: 10.1016/j.neuroimage.2011.08.107.
- [139] D. S. Tuch, V. J. Wedeen, A. M. Dale, J. S. George, and J. W. Belliveau, “Conductivity tensor mapping of the human brain using diffusion tensor MRI,” *Proc. Natl. Acad. Sci.*, vol. 98, no. 20, pp. 11697–11701, Sep. 2001, doi: 10.1073/pnas.171473898.
- [140] M. S. Branicky, V. S. Borkar, and S. K. Mitter, “A unified framework for hybrid control: model and optimal control theory,” *IEEE Trans. Automat. Contr.*, vol. 43, no. 1, pp. 31–45, 1998, doi: 10.1109/9.654885.

Vita

Ryan Woodall was born and raised in Albuquerque, NM, where he graduated from Albuquerque Academy in the class of 2010. In 2014, Ryan graduated cum laude from Trinity University, in San Antonio, Texas, with a Bachelor of Science in Engineering Science, and a Minor in Mathematics. Ryan earned a Master's and Doctoral degree from the Department of Biomedical Engineering at The University of Texas at Austin, where his research was focused on the intersection of medical imaging and biological fluid transport. During his time at UT Austin, Ryan earned an NIH Fellowship and coursework portfolio in Imaging Science and Informatics. The results of his work have been published in multiple primary- and co-authored journal articles, as well as conference presentations and proceedings. He completed his PhD in July of 2020 during the COVID-19 pandemic.

Email: woodall.rt@gmail.com

This dissertation was typed by Ryan Thomas Woodall